

Dottorato di Ricerca
in
Ingegneria Elettronica
“Dalle nanostrutture ai sistemi”

XXI Ciclo

Ph.D. Thesis

**An Adaptive Optics system for the automatic control of
laser beam jitters in air**

Salvatore Grasso

Docenti Guida:

Prof. Giuseppe Schirripa Spagnolo

Prof. Fabrizio Barone

Coordinatore:

Prof. Gennaro Conte

October 2008

Contents

Introduction.....	7
1 Virgo Project: the interferometric detection of gravitational waves.....	12
1.1 GW detection in interferometric antennas	13
1.2 Design, construction and commissioning of the Virgo antenna.....	16
1.3 Noise management and sensitivity curve	19
1.3.1 Seismic noise.....	21
1.3.2 Shot noise.....	22
1.3.3 Thermal noise.....	24
1.3.4 Virgo sensitivity curve	26
1.4 Noise from coupling of interferometer asymmetries with input laser beam jitters	27
1.5 Passive suppression and requirements for active prefiltering of the laser jitters	30
2 Adaptive Optics	34
2.1 Optical aberration and Zernike polynomials	34
2.2 Scheme and operation of a standard AO system.....	40
2.3 Main components and operative parameters	42
2.3.1 Wavefront Aberration Measurement.....	42
2.3.2 Actuators for wavefront aberration control	45
2.3.3 Operative parameters and performances of an AO system	48
2.4 Fields of application of AO.....	53
2.5 State of the art and future outlooks of the AO technology	62
3 Project of the Adaptive Optics system based on interferometric techniques for the automatic control of laser beam jitters in air	66
3.1 Gaussian Optics and higher order Hermite Gauss modes.....	68
3.2 Wavefront analysis of the perturbed Gaussian beam: correspondence between Hermite Gauss modes and Zernike polynomials	72
3.3 Optical design of the interferometric AO system	77
3.4 Design of the feedback control system	80
3.4.1 Control system for the interferometer lock in.....	83
3.4.2 Control system for the correction of laser beam aberrations.....	85
3.5 Error signals extraction from the Controlled System and diagonalization of the 6x6 transfer matrix K	90

3.6	<i>Calculation of the 6x6 transfer matrix A of the Regulator and diagonalization of the 6x6 matrix G relative to the open loop system</i>	102
4	Implementation of the Prototype	110
4.1	<i>Architecture of the AO interferometric system</i>	111
4.2	<i>Laser Source</i>	114
4.3	<i>Adaptive mirror</i>	116
4.4	<i>Array of photodiodes</i>	118
4.5	<i>Optical arrangement for mode matching of the laser beam with the interferometer</i>	122
4.6	<i>Data processor</i>	128
5	Test of the prototype, results and discussion	131
5.1	<i>Measurement of the frequency response function of the control system</i>	132
5.1.1	Some theoretical principles	132
5.1.2	Methodology of measurement	138
5.1.3	Results and discussion	140
5.2	<i>Measurement of residual noise in the controlled laser beam</i>	158
5.2.1	Some theoretical principles	158
5.2.2	Methodology of measurement	161
5.2.3	Results and discussion	162
5.3	<i>Quality control of the Gaussian beam</i>	171
5.3.1	Some theoretical principles	171
5.3.2	Methodology of measurement	174
5.3.3	Results and discussion	175
	Conclusions	178

Introduction

The direct measurement of the Gravitational Waves (GW) foreseen by Einstein's General Theory of Relativity has never been demonstrated and therefore it is one of the most important challenges of the scientific research. Currently several large scale experiments are being carried out all over the world aiming to first perform direct detection of gravitational signals coming from Space.

The scientific benefits expected from the measurement of GW concern several fields of theoretical and experimental Physics. First of all, the direct detection of GW is a primary test for the confirmation of the Einstein's theory. Secondly, the measurement of the *gravitons* will provide an important contribution to the theory of unification of the fundamental forces. Furthermore, in the field of Astronomy and Cosmology, the GW measurement will add new information to the knowledge of the Universe, that is actually based on the collection of electromagnetic waves and neutrinos. In particular, as the most of the astronomical bodies are transparent to gravitational waves due to their very low absorption coefficient, the GW detection will open a new observational window that is the Gravitational Wave Astronomy.

It is also worth noting that the development of large and sophisticated GW detectors drives interesting lines of research of Applied Physics and Engineering which are strongly involved for the implementation of performing components and subsystems. This is exactly the case of the present PhD work in Electronical Engineering as we are going to present in the following.

Two kinds of ground based detectors have been proposed in the last few decades, but none of them has yet performed the direct measurement of GW. Detectors based on the Webber bars have been put into operation since 1960, but due to their limited bandwidth and low sensitivity they do not seem to be adapt for this purpose. On the contrary, long baseline interferometric antennas like LIGO in the Unites States and VIRGO in Italy are wideband and low noise detectors that promise to successfully operate the measurement of gravitational waves.

The *VIRGO Project* is an Italian and French collaboration started 20 years ago and finalized to the realization of a big experiment for the GW detection on Cascina site (Pisa). The Virgo antenna is a ground based Michelson interferometer of 3 km long arms with optics suspended by a multistage pendulum for the seismic isolation. The principle of detection is based on the

assumption that the gravitational perturbation coming from Space induces a displacement of the suspended terminal mirrors of the Michelson. This causes a variation of the phase difference of the two beams into the interferometer and consequently changes the interference fringes pattern at the output of the Michelson. The intensity variation that is read at the photodetector surface can be directly connected to the GW measurement.

The extreme weakness of the expected gravitational signal makes very difficult its detection because in the bandwidth $10\text{ Hz} \div 10\text{ kHz}$ it is necessary to measure mirror displacements of the order of $10^{-18}\text{ m}/\sqrt{\text{Hz}}$ corresponding to $10^{-11}\text{ rad}/\sqrt{\text{Hz}}$ variation of the phase difference of the two beams into the Michelson. Therefore, most of the scientific and technical efforts of the Virgo Groups have been finalized to carry out a complete *noise management* of the antenna, that is the identification of all the possible sources of noise, the assessment of their effects on the measurement and the investigation of solutions for noise reduction down to residual values that make the interferometer able to *sense* very weak signals. The Virgo sensitivity curve that has been achieved thanks to the noise management work of the Virgo Groups is actually the lower limit for GW detection and corresponds to the detectivity of $10^{-19}\text{ m}/\sqrt{\text{Hz}}$ in the central band at 100 Hz. This means that the first generation of Virgo has a real chance of detecting the GW for the first time ever.

Nevertheless, further efforts are currently performed by researchers in order to discover new margins of improvement for the actual antenna as well as for Advanced Virgo, that is a major upgrade with the goal of increasing the Virgo sensitivity by about one order of magnitude in the whole detection band. In fact this result would allow the antenna to see many events every year thus starting the era of gravitational wave astronomy.

One of the possible improvements that are being investigated in Virgo is the reduction of the noise that has been demonstrated to origin from the coupling between the input laser beam jitters and the interferometer asymmetries.

The necessity of containing that kind of noise below the Virgo detectivity threshold has first induced designers and researchers to impose strict statements for the alignment of the suspended optics. These requirements are fulfilled at the best of the present technology using sophisticated control systems, but serious doubts arise to the possibility of keeping a fine optical alignment for long term period in a large scale interferometer exposed to the atmospheric factors. Therefore much attention has also been paid to the possibility of reducing that noise acting on the suppression of the input laser beam jitters. In the actual antenna this suppression is already operated using a

passive filtering system named *mode cleaner*, that is a triangular Fabry-Perot cavity of Finesse 1000 placed at the input of the detector. The cavity reduces of three orders of magnitude the jitters of the input laser beam before it enters the interferometer, but this is not sufficient to relax the statements of optical alignment neither it permits to significantly improve the sensitivity curve in view of Advanced Virgo. Therefore other solutions are being explored in these years to perform an active filtering of the laser in cascade with the mode cleaner, but up to date no system has yet demonstrated to fit the constraints for the reduction of the input laser perturbations. Therefore this argument is still an open issue in the environment of the scientific research of Virgo.

Starting from this context, the target of the our PhD work has been the development of an Adaptive Optics (AO) system for the active filtering of laser beam jitters. We have proposed and designed the system, implemented an experimental prototype in laboratory and tested it upon different sets of measures that validate the design and confirm the effectiveness and the robustness of the proposed AO control system in compliance with the Virgo requirements.

The present Doctoral Thesis is arranged in five Chapters which present our R&D work and the results obtained in these last three years.

In Chapter 1 we make a short overview of the Virgo Project starting from the general principles of GW detection in an interferometric antenna. We present the main characteristics of the Virgo detector that has been designed for wideband and high sensitivity operation and has been commissioned on Cascina site in 2003. The problem of noise into the interferometer is widely discussed with particular reference to seismic noise, thermal noise and shot noise, that are the three main noise sources limiting the sensitivity respectively in the range of low, medium and high frequency of the detection band. Finally, we analyze the noise originated by the coupling of the input laser beam jitters with the interferometer asymmetries, discuss the passive reduction operated by the mode cleaner and then put in evidence the requirements for an additional active filtering that is needed for the upgrade of the antenna.

The technology of Adaptive Optics is discussed in Chapter 2, where we investigate the opportunities offered by current systems and the limitations exhibited when they operate the dynamical correction of wavefront aberrations. We begin with a short description of the optical aberrations and their representation in terms of Zernike polynomials. Successively, we present the standard configuration of an AO system that is essentially based on the architecture of a closed loop control where it is well distinguished the

sensor, the actuator and the processing unit. In particular we present the Shack Hartmann wavefront sensor and the most common models of actuators, that are two classes of deformable mirrors with segmented or continuous reflecting surface. We also present the main operative parameters of the AO systems and the principal applications in the fields of astronomy, industry and medicine.

Chapter 3 enters the core of our R&D work and presents the Project of the AO system based on an interferometric technique for the detection of laser beam jitters. We start with a short description of Gaussian optics concerning the characteristics and the propagation in air of the laser fundamental mode. Soon after, we perform the theoretical analysis which demonstrates that laser beam jitters can be alternatively described with higher order Hermite Gauss modes perturbing the Gaussian beam or with Zernike polynomials expanding the laser aberrated wavefront. This correspondence allows to design an AO system that extracts the error signals in terms of Hermite Gauss coefficients and generates the correction commands for the deformable mirror in terms of Zernike modes. We discuss in detail the mode of operation of the proposed AO system that performs the simultaneous correction of six aberration modes up to the second order. In particular we present the optical design based on the Michelson interferometric configuration and the block diagram of the closed loop control.

The experimental apparatus implemented in the Laboratory of Applied Physics at the University of Salerno is described in Chapter 4. We show the scheme of the whole system and the characteristics of the main components. Specific sections are devoted to the input laser, to the adaptive mirror for the wavefront correction and to the photodiodes 5x5 array placed at the output of the Michelson for the error signal extraction. We also present the electronic boards designed and engineered in our laboratory for the amplification of the photocurrents emerging from the photodiodes. Chapter 4 ends with a description of the optical arrangement that we have performed to match the input laser beam with the interferometer and in particular to control the position and the diameter of the beam waist on the deformable mirror and on the photodiodes surface.

In Chapter 5 we report and discuss the three sets of measurements carried out for the complete characterization of the prototype. We have first measured the transfer functions of the AO system both at open and closed loop in order to demonstrate effectiveness and stability of the different controls acting simultaneously on the six aberration modes of the laser beam. Secondly, we have directly measured the six error signals representing the perturbation coefficients and from the analysis of their curves in the time domain as well

as in the spectral representation we test the reduction operated by the AO control when the loop is closed. Finally, we have achieved the quality control of the corrected laser beam by the measurement of its transverse intensity that is detected at the output of the Michelson and then fitted to the ideal Gaussian profile.

The present Thesis ends with the Conclusions where we summarize the results of the R&D work and remark that our AO system fulfils the Virgo requirements for laser correction and therefore it can be seriously proposed for application to interferometric GW antennas.

Chapter 1

Virgo Project: the interferometric detection of gravitational waves

The Virgo Project is one of the most popular experiments carried out in the world for the direct measurement of gravitational waves (GW). It was born from an Italian and French collaboration which allowed the implementation of a ground based interferometric gravitational wave antenna located in Cascina, a small Italian municipality near Pisa. The Virgo antenna operates in correlation with other similar detectors like the two interferometers of LIGO Project in the United States, and it is expected that it can detect gravitational waves generated by star masses moving in the Universe.

In this first Chapter we discuss the principle of operation of an interferometric GW antenna based on the Michelson scheme, and then we present the Virgo Project with a brief overview about the design and commissioning. After that, we approach the problem of the weakness of the gravitational signals and discuss the studies and the arrangements that have been performed in order to maximize the sensitivity and minimize the noise that affects the Virgo interferometer. In particular, we analyze the seismic noise, the thermal noise and the shot noise, that are the three main sources of disturbance that delimit the lower level of the Virgo detectivity in three different spectral ranges of the detection bandwidth. Finally, we dedicate a specific section to the noise generated by the coupling between the interferometer asymmetries and the input laser beam jitter, which puts serious open issues for the performing of the actual interferometer and also of the next generation advanced gravitational antennas. We identify the Virgo requirements for the reduction of this noise and propose the application of an Adaptive Optics system in accordance with those statements. The development of such a system and the demonstration of its efficacy in accordance with the preliminary statements is the core of our PhD work and will be presented in the next Chapters.

1.1 GW detection in interferometric antennas

The gravitational waves are perturbations of the space-time metric that propagate at the speed of light and modify the distance between two points, as foreseen by the Einstein's General Theory of Relativity [1],..., [5]. They are originated by the movement of any mass, but, due to the weakness of the signal, it is not possible to produce detectable gravitational waves in laboratory. So, the only possibility to perform a direct measurement of them is to collect signals originated by big astronomical objects, such as Supernovae, Coalescent binaries and Pulsars, which emit gravitational waves in the frequency band from few Hz to few kHz and can have impulsive, periodic or stochastic behaviour [6],..., [9].

For this reason, different kinds of very complex and high sensitivity ground based detectors have been built in the recent years, but up to date the direct measurement of gravitational waves has not yet been achieved, and therefore it is still a strong commitment for the researchers involved in the field of the experimental relativity [10], [11], [12].

The scientific benefits that are expected from the direct GW detection concern several fields of the theoretical and experimental Physics. First of all, the measurement of gravitational waves is an important test which confirms the Einstein's theory after that other experiments have already been carried out with success [10]; secondly, in terms of quantum physics, the measurement of the *gravitons* can give an important contribution to the theory of unification of the fundamental forces. Furthermore, in the field of Astronomy and Cosmology, the GW measurement will add new information to the knowledge of the Universe, that is actually based on the collection of electromagnetic waves and neutrinos coming from the Space. In particular, as the most of the astronomical bodies are transparent to gravitational waves due to their very low absorption coefficient, the direct measurement of them will open a new observational window that is the Gravitational Wave Astronomy. And finally, but not less important, the development of large and sophisticated GW detectors drives interesting applications of applied physics and engineering, which contribute to the implementation of very performing components and subsystems. This is the case of the present PhD work in Electronical Engineering, where we have developed an Adaptive Optics system for the laser beam filtering.

The gravitational waves are generated by star masses whose movement is not spherically symmetric. In this case, the amplitude of the wave is given by the adimensional parameter h as:

$$h = \frac{4G\varepsilon_{ns}E_{kin}}{c^4 r} \quad (1.1)$$

where G is the Newton constant, c is the speed of light in vacuum, r is the distance between the source and the detector, E_{kin} is the total kinetic energy of the source mass and ε_{ns} ($0 \leq \varepsilon_{ns} \leq 1$) the fraction of kinetic energy not spherically symmetric.

The possibility of detecting the gravitational waves depends on the amplitude $h_s(t)$ of the wave generated from the source S , on its frequency distribution, and on the noise h_n of the detector. If f_c is the characteristic frequency of the signal in the center of the spectral range Δf , the signal to noise ratio of the detector is:

$$\frac{S}{N} \approx \frac{|h_s(t)|}{\tilde{h}_n(f_c) \cdot \Delta f^{1/2}} \quad (1.2)$$

being $\tilde{h}_n(f)$ the power spectral density of the intrinsic noise of the detector, expressed in units of $1/\sqrt{\text{Hz}}$. Therefore, if we use low noise detectors, we can sense weak signals from very far sources, that is we increase the possibility of detectable gravitational events and then we widen the part of Universe that we can investigate.

So far, three different kinds of GW detectors have been proposed, that are respectively the Webber bars, the ground based interferometric antennas and the space interferometers. Several Webber bars have been built and are operating since 1960, but they are strictly band limited and not very noiseless ($\tilde{h} \cong 10^{-16} \text{ Hz}^{-1/2}$ at $f=1 \text{ KHz}$), and none of them has ever performed a successful measurement. On the other side, space interferometers could be very sensitive and low noise, but their implementation and commissioning would be so costly and difficult that no Project has been financed in the world. This is why in the past years attention has been moved to ground based interferometric antennas, which have been built in several big experiments in the world as they promised to be wideband and high sensitivity detectors at a reasonable cost of construction [13].

The principle of operation of an interferometric GW antenna based on the Michelson configuration is easy to understand if we refer to the scheme shown in figure 1.1.

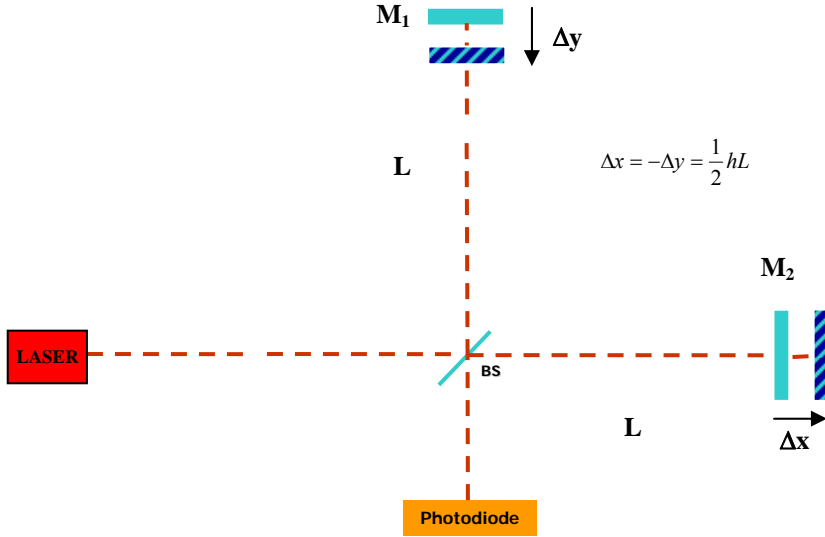


Figure 1.1: Scheme of the Michelson interferometer used as antenna and effect of the gravitational wave h on the test masses corresponding to displacement $-\Delta y$ and Δx of the terminal mirrors M_1 and M_2 respectively. BS is the beam splitter of the input laser and L is the arms length. The phase difference induced by the gravitational wave is measured by the photodiode through the variation of the output intensity. The direction of propagation of the wave is assumed perpendicular to the plane of the paper.

The gravitational wave impinging on the Michelson interferometer, perpendicularly to the plane of the optical system, is represented by the perturbation $h=h(t)$ of the space time, and moves the test masses corresponding to the terminal mirrors M_1 and M_2 of the Michelson interferometer by alternated squeezing and stretching of its arms of length L . If we assume the ideal case where the two masses could be considered free in air, their displacements are simply given by:

$$\Delta x = -\Delta y = \frac{1}{2} hL \quad (1.3)$$

The displacement of the two mirrors from the equilibrium position changes the interference condition and therefore the optical paths phase difference of the two orthogonal beams of the interferometer is:

$$\Delta\phi(t) = \frac{4\pi}{\lambda} (\Delta x - \Delta y) = \frac{4\pi L}{\lambda} h(t) \quad (1.4)$$

This last equation shows that the Michelson interferometer behaves like a linear gravitational antenna, as the phase difference $\Delta\phi(t)$, which we can detect by the interference fringes variation measured by the photodiode, is proportional to the gravitational signal $h(t)$.

In the real case, for the seismic isolation, the mirrors are suspended by a mechanical pendulum of resonance frequency ω_0 and time constant τ , and therefore the displacements Δx and Δy are obtained by the following differential equations:

$$\begin{aligned}\frac{d^2\Delta x}{dt^2} + \frac{1}{\tau} \frac{d\Delta x}{dt} + \omega_0^2 \Delta x &= \frac{1}{2} \frac{d^2 h}{dt^2} L \\ \frac{d^2\Delta y}{dt^2} + \frac{1}{\tau} \frac{d\Delta y}{dt} + \omega_0^2 \Delta y &= -\frac{1}{2} \frac{d^2 h}{dt^2} L\end{aligned}\tag{1.5}$$

It can be seen that in the Fourier domain, for gravitational waves of frequencies $\omega \gg \omega_0$, the solutions of eqs. (1.5) are $\Delta x = -\Delta y = (1/2)Lh_0 \exp(i\omega t)$, and so the phase difference is:

$$\Delta\phi = \frac{4\pi L}{\lambda} h_0 e^{i\omega t}\tag{1.6}$$

That is, for frequencies ω much higher than the resonance frequency ω_0 of the pendulum, the mirror behaves like a free-fall mass and hence by measuring the phase difference $\Delta\phi(t)$ we can have a proportional measurement of the wave amplitude h_0 .

1.2 Design, construction and commissioning of the Virgo antenna

The Virgo Project was born from an Italian and French collaboration supported by INFN (Italy) and CNRS (France) and is nowadays one of the

most important experiments in the world for the interferometric GW detection [14], [15]. The Virgo antenna is a long baseline Michelson interferometer with a 3 km long Fabry Perot cavity implemented in each of the two arms, designed for wideband (10Hz÷10kHz) detection of gravitational waves with sensitivity $\tilde{h} \approx 10^{-23} \div 10^{-22} 1/\sqrt{\text{Hz}}$, which corresponds to measure displacements of the test masses of the order of $10^{-19} \text{ m}/\sqrt{\text{Hz}}$. It is located at the European Gravitational Observatory (EGO) close to Cascina (Pisa, Italy) as shown in figure 1.2 and has been commissioned in 2003-2004. The data collected by Virgo are compared and correlated with those generated by other similar antennas presently in action such as LIGO, TAMA and GEO [16], [17], [18], [19].



Figure 1.2: Virgo antenna at Cascina (Pisa)

The Virgo antenna is a Michelson interferometer implemented into a ground based steel structure of towers and tubes containing all the suspended optics and all the necessary equipments.

The input source is a 20 W Nd:YAG laser at 1064 nm which is split on the beam splitter and enters the two 3 km long Fabry Perot cavities. The suspended optics of the Virgo interferometer are large diameter (350 mm)

and big mass (20 kg) mirrors and beam splitter, with super polished, very low absorption and scattering surfaces manufactured by the German company Heraeus in collaboration with ESPCI (Paris).

The terminal mirrors, used as test masses, are located in an ultra high vacuum system (from 10^{-9} mbar for H_2 to 10^{-14} mbar for hydrocarbon) and suspended by a sophisticated multistage pendulum for the seismic isolation. This is the Superattenuator (SA) pictured in figure 1.3, that is a 10 m tall chain of mechanical filters positioned into each of the two terminal steel towers of the antenna [20], [21], [22].

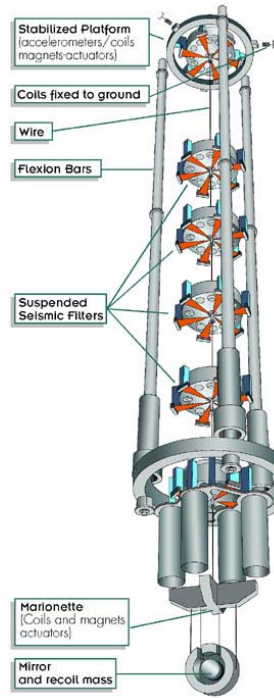


Figure 1.3: Scheme of the Virgo Superattenuator (SA) chain: active control is exerted by coils and magnets at three stages: inertial damping on the top, local control on the marionette and locking on the mirror using the reference mass

The SA isolates the test masses from the ground motion. A passive filtering is provided to the mirror at frequency higher than a few Hz, as the pendulum is a chain of mechanical filters whose resonance frequencies lay all below 2 Hz. This passive attenuation is better than $10^{-18} \text{ m}/\sqrt{\text{Hz}}$ at 10 Hz. Furthermore, in order to reduce the low frequency residual motion due to the chain resonances and achieve the pre-alignment of the interferometer, an active

control is performed by exerting control forces on three actuation point, that are respectively the top stage, the marionette and directly the mirror. The control is carried out by magnetic forces induced by coils on permanent magnets put on specific points of the suspension chain.

The position of the mirrors is then controlled in real-time through a feed-back system so to keep the interferometer in the condition of destructive interference (also called dark-fringe lock in) [23], [24]. The passing of a gravitational wave, or any other effect which try to move the mirror position, induces a reaction signal in the feed-back system which represents the signal of the antenna. Once the interferometer is longitudinally locked, it is necessary to maintain the mirrors aligned each other and with respect to the incoming beam with rms accuracy close to 10^{-9} rad [25], [26].

Several commissioning runs have been performed since 2003 in order to put into operation the different subsystems and step by step the ideal sensitivity curve has been quite well approached [27], [28], [29]. The treatment of all the engineering that has been necessary for the implementation of this large and sophisticated detector is of course interesting but overcomes the scope of the present work, and therefore the reader is referred to the bibliography.

1.3 Noise management and sensitivity curve

Despite of the simplicity of the principle of operation, based on a classic interferometric sensor, the detection of a gravitational wave is dramatically difficult, because of the weakness of the waves, which cause very small variations of the Michelson arms length. In fact, the detection of mirror displacements of the order of $10^{-19} \div 10^{-18} \text{ m}/\sqrt{\text{Hz}}$ imposes the implementation of a very sensitive and low noise sensor, and therefore several issues have been taken into account in the design and the construction of the Virgo antenna, and several studies are still being done, in order to achieve the desired performance.

The first requirement which the detector must fulfil is to maximize the sensitivity S , derived by eq. (1.4) as:

$$S = \frac{\Delta\phi}{h} = \frac{4\pi L}{\lambda} \quad (1.7)$$

This last expression shows that the antenna sensitivity is proportional to the length L of the Michelson arms, and therefore it can be increased by increasing L . That is why long baseline gravitational antennas have been built, like Virgo interferometer having 3 km long arms. Nevertheless, such a length is not yet sufficient to guarantee the minimum degree of sensitivity required for the GW detection, while, on the other side, it is not possible to build arms of 100 km for obvious reasons of cost and technological difficulties. The problem has been overcome by increasing the optical path of the two laser beams before recombining, using two Fabry-Perot cavities implemented in each interferometer arm as shown in figure 1.4.

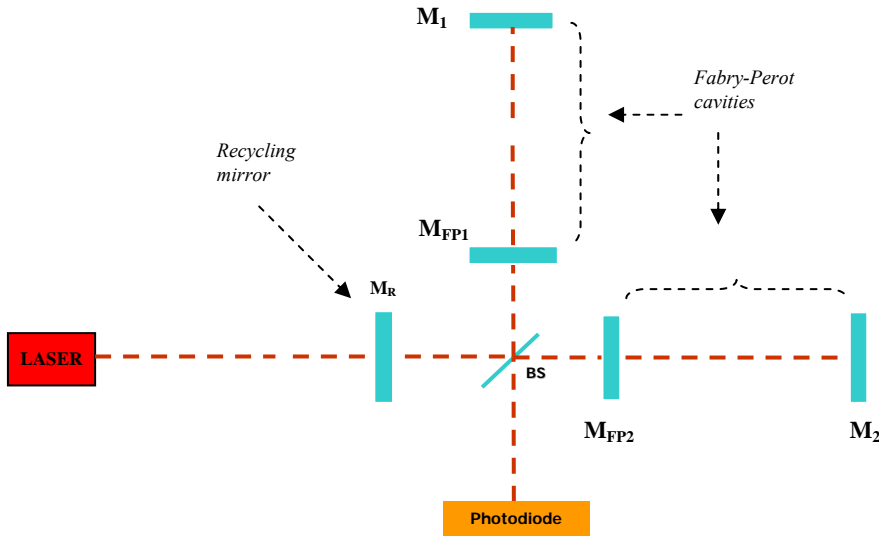


Figure 1.4: Layout of the Virgo interferometer of arms length $L=3$ km . The terminal mirrors M_1 and M_2 , which form two Fabry-Perot cavities with M_{FP1} and M_{FP2} respectively. BS is the beam splitter of the input laser, and M_R is the recycling mirror.

In fact, in this case the detector sensitivity is increased by the factor $2F/\pi \approx 32$, being $F=50$ the Virgo cavities *Finesse*, or:

$$S = \frac{\Delta\phi}{h} = \frac{4\pi L}{\lambda} \frac{2F}{\pi} = \frac{4\pi L'}{\lambda} \quad (1.8)$$

This also means that the effective arms length changes from $L=3$ km to $L'=2FL/\pi \approx 96$ km .

The second requirement of the Virgo antenna is the minimization of all the possible sources of noise which could limit the detectivity in the sensing bandwidth. A great part of the scientific and engineering work of the Virgo Groups has been devoted to this problem, which is a very important issue to solve for the success of the Project. So, in these last years a typical *noise management* has been carried out, where all the forms of noise that could affect the detector have been identified, assessed and if necessary reduced to a residual level that stands below the officially accepted lower limit of detectivity, or Virgo sensitivity curve.

The three main sources of noise in the Virgo antenna are the seismic noise, the shot noise and the thermal noise, which characterize the sensitivity curve respectively in the low frequency band, in the high frequency band and in the central band.

1.3.1 Seismic noise

The seismic vibrations of the ground deform the interferometer arms length, and hence they introduce a perturbation into the gravitational antenna that is named *seismic noise*. The power spectral density of this noise has been experimentally achieved through direct measurements on the Cascina site, and the result is well fitted over 0.1 Hz by the following expression:

$$\tilde{x}_s(f) \cong \frac{10^{-6}}{f} \frac{m}{\sqrt{Hz}} \quad (1.9)$$

which, in terms of gravitational detectivity, is:

$$\tilde{h}_s(f) = \frac{2\tilde{x}_s(f)}{L(3km)} \cong \frac{0.7 \cdot 10^{-9}}{f^2} \frac{1}{\sqrt{HZ}} \quad (1.10)$$

This seismic noise would seriously limit the interferometer sensitivity if no action was made for reduction. For example, at 100 Hz, the value of seismic noise would be $\tilde{h}_s(f=100) \cong 0.7 \cdot 10^{-13} 1/\sqrt{Hz}$, that is vary far from the desired detectivity $\tilde{h} = 10^{-23} 1/\sqrt{Hz}$.

In order to isolate the interferometer from the seismic noise, all the optics are suspended to Superattenuators (SA) [30], that act as passive mechanical

filters and perform, from the top of the chain to the bottom where the mirror is suspended, an attenuation of the vibration given by:

$$A(\omega) = \frac{\tilde{x}_{s'}}{\tilde{x}_s} \propto \prod_{n=1}^N \frac{\omega_n^2}{(-\omega^2 + \omega_n^2)} \quad (1.11)$$

being $\tilde{x}_{s'}$ the mirror vibration reduced by the chain of N pendula of resonance frequencies ω_n .

We have already said that the design of the SA provides that all the resonance frequencies are below 2 Hz, and therefore the seismic noise characterizes the sensitivity curve at low frequency, while in the detection bandwidth over 10 Hz, where $\omega \gg \omega_n \quad \forall n$, the SA damping is $A \propto \omega^{-2N}$ and the residual seismic noise transferred to the mirror is absolutely negligible.

1.3.2 Shot noise

The shot noise is the quantum limit to the phase detection due to the statistic fluctuation of the number of photons collected by the photodiode at the output of the interferometer.

The laser beam that reaches the photodiode has a number of photons n with uncertainty Δn described by the Poisson statistics for coherent light $\Delta n = \sqrt{n}$ [31]. In addition, the uncertainty in measuring the phase and the photons number is regulated by the quantum uncertainty relation in measuring $\Delta\phi \cdot \Delta n \geq 1$. Therefore, the uncertainty on the phase is:

$$\Delta\phi \geq \frac{1}{\sqrt{n}} \quad (1.12)$$

Moreover, the energy E collected by the photodiode of quantum efficiency η is $E = \eta n \hbar \omega_0$, where \hbar is the Planck's constant and ω_0 the laser angular frequency. So, if we consider that $E = P \Delta t$, being P the laser power and Δt the measure time, by simple algebra the phase uncertainty can be rewritten as:

$$\Delta\phi \geq \sqrt{\frac{\hbar \omega_0}{\eta P \Delta t}} \quad (1.13)$$

or, in terms of power spectral density:

$$\Delta\tilde{\phi} = \Delta\phi\sqrt{\Delta t} \geq \sqrt{\frac{\hbar\omega_0}{\eta P}} \quad (1.14)$$

Finally, from eq. (1.8), the shot noise in the Virgo antenna is:

$$\tilde{h}_{sn} \geq \frac{\lambda}{4\pi L'} \sqrt{\frac{\hbar\omega_0}{\eta P}} \quad \left(\frac{1}{\sqrt{\text{Hz}}} \right) \quad (1.15)$$

From this last result, we see that it is possible to reduce the shot noise by increasing the laser power inside the interferometer. This is done placing the *recycling mirror* in front of the input laser as shown in figure 1.4. In fact, as we have already discussed, the Virgo interferometer is locked in the configuration of dark fringe, and this means that the light is almost all reflected back toward the laser. The recycling mirror reflects back the light toward the beam splitter, and then it increases the effective power that enters the interferometer. In practice, the recycling mirror and the whole interferometer form a new cavity, in which the recycling mirror is the first mirror and the interferometer is the second one. If the cavity is in resonance with the input laser, the power that comes on the beam splitter and then enters the interferometer increases of a factor depending on the Finesse of the cavity. In the case of Virgo, the Finesse of the recycling cavity is 50, and therefore the optical power of the input laser is raised from 20 *W* to 1 *kW* inside the interferometer. So, being 95% the quantum efficiency of the InGaAS photodiode, and remembering that $\lambda=1064 \text{ nm}$ and $L'=96 \text{ km}$, the Virgo shot noise level is:

$$\tilde{h}_{sn} \cong 3 \cdot 10^{-23} \frac{1}{\sqrt{\text{Hz}}} \quad (1.16)$$

which fulfils the detectivity requirements in the central band at 100 *Hz*.

1.3.3 Thermal noise

The thermal noise affects the suspensions and the mirrors of the interferometer [32], [33], [34]. It is originated by the stochastic thermal motion of the atoms contained in the mechanical structures: in fact, this motion produces stochastic forces that excite the resonance modes of the suspensions and the normal modes of the mirrors. The power spectral density of those stochastic forces was calculated by Uhlenbeck and Ornstein in the fluctuation-dissipation theorem and corresponds to:

$$\tilde{F} = \sqrt{\frac{4K_B T M}{\tau}} \left(\frac{N}{\sqrt{\text{Hz}}} \right) \quad (1.17)$$

where M is the mass, T the temperature, K_B the Boltzmann's constant and τ the time constant.

The thermal noise due to the suspension can be calculated using the transfer function of the pendulum of resonance frequency ω_0 and quality factor Q ; in this case the power spectral density of the mirror displacement is:

$$\tilde{x}_{tPend} = \frac{\tilde{F}/M}{-\omega^2 + \omega_0^2 + i\frac{\omega}{\tau}} = \sqrt{\frac{4K_B T}{QM\omega_0^3}} \frac{1}{1 - \left(\frac{\omega}{\omega_0}\right)^2 + i\frac{\omega}{Q\omega_0}} \quad (1.18)$$

or, in terms of amplitude:

$$\tilde{x}_{tPend} = \sqrt{\frac{4K_B T}{QM\omega_0^3}} \frac{1}{\sqrt{\left[1 - \left(\frac{\omega}{\omega_0}\right)^2\right]^2 + \left(\frac{\omega}{Q\omega_0}\right)^2}} \quad (1.19)$$

In the detection bandwidth, where $\omega \gg \omega_0$, the thermal noise reduces to:

$$\tilde{x}_{tPend} = \sqrt{\frac{4K_B T \omega_0}{QM}} \frac{1}{\omega^2} \quad (1.20)$$

and, in terms of gravitational detectivity, it is:

$$\tilde{h}_{tPend} = \frac{2\tilde{x}_{tPend}}{L(3km)} = \frac{2}{L\omega^2} \sqrt{\frac{4K_B T \omega_0}{QM}} \quad (1.21)$$

Using the Virgo parameters $Q=10^6$, $\omega_0=2\pi \text{ rad/s}$, $T=300 \text{ K}$ and $M=20 \text{ kg}$ for the mirror mass, we can calculate that the thermal noise of eq. (1.21) is relevant in the spectral range between 3 Hz and 30 Hz , while it decreases rapidly for higher frequencies due the term $1/\omega^2$.

The thermal motion of the atoms also excite the normal modes of the mirror which have resonance frequencies at several kHz, and therefore above the bandwidth of detection.. In order to calculate the analytical expression of this thermal noise, we can schematize the mirror as a set of independent harmonic oscillators of normal frequencies ω_i , quality factors Q_i , time constants τ_i and effective masses M_i . In this case the amplitude of the mirror displacement has the following spectral density:

$$\tilde{x}_{tMir} = \sum_i \sqrt{\frac{4K_B T}{Q_i M_i \omega_i^3}} \frac{1}{\sqrt{\left[1 - \left(\frac{\omega}{\omega_i}\right)^2\right]^2 + \left(\frac{\omega}{Q_i \omega_i}\right)^2}} \quad (1.22)$$

In the detection bandwidth, where $\omega \ll \omega_i \forall i$, this expression reduces to:

$$\tilde{x}_{tMir} \cong \sqrt{\frac{4K_B T}{Q_1 M_1 \omega_1^3}} \quad (1.23)$$

and hence

$$\tilde{h}_{tMir} \cong \frac{2}{L} \sqrt{\frac{4K_B T}{Q_1 M_1 \omega_1^3}} \quad (1.24)$$

where the index 1 refers to the fundamental normal mode of the mirror. This value is generally lower than the other noises, except for the range from 30 Hz to 200 Hz , where it is the most relevant and characterizes the lower limit of the Virgo detectivity.

1.3.4 Virgo sensitivity curve

The Virgo sensitivity curve is the lower level of spectral detectivity that is possible to achieve taking into account the contribution of all the possible noises that affect the interferometer.

In the previous subsections we have discussed only the seismic noise, the shot noise and the thermal noise, because these are the fundamental disturbances that characterize the Virgo sensitivity curve in the different spectral regions. In particular, the seismic noise limits the sensitivity at low frequency below 3 Hz, the thermal noise characterizes the sensitivity from 3 Hz to 200 Hz, and the shot noise is essentially the upper limit above 200 Hz. This can be easily seen in figure 1.5, where we report the Virgo sensitivity curve as officially accepted by the Groups of research of the Virgo Project.

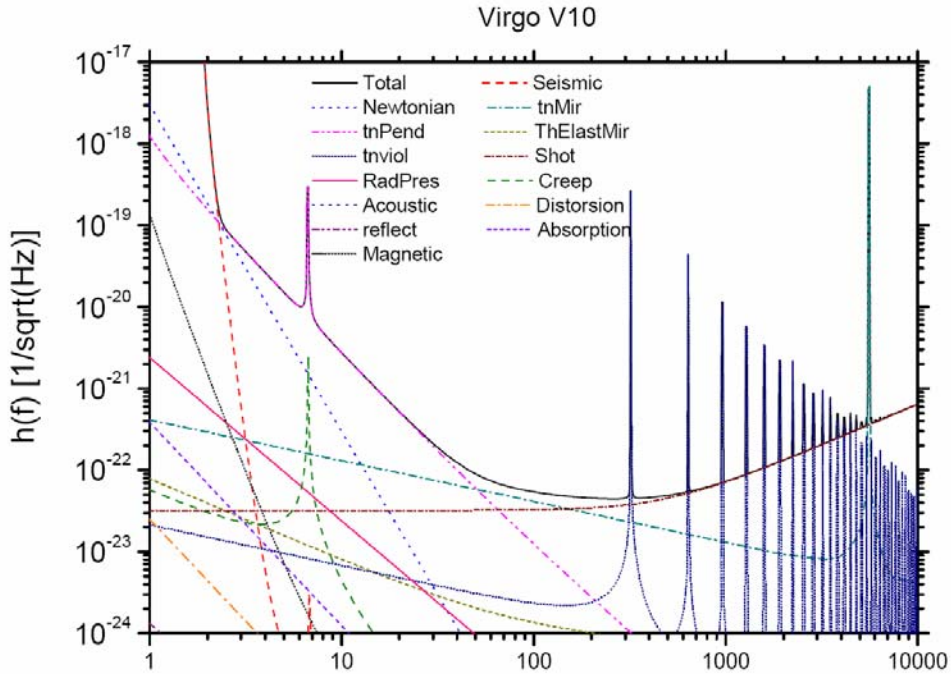


Figure 1.5: Virgo sensitivity curve with the limiting noise sources. The most relevant are the seismic noise at low frequency up to 3 Hz, the thermal noise from 3 Hz to 200 Hz and the shot noise at higher frequencies

The graph also shows other several curves of noise, that have been assessed and/or measured in the recent years by the researchers of the different Virgo Groups for a complete characterization of the interferometer [35],..., [44]. Today, a strong effort is still being done to investigate the possibility of reducing some of these noises, not only to improve the performance of the present antenna, but also to open prospects for the implementation of the new interferometer that is Advanced Virgo.

In particular, in our work of research, we have put our attention to the phase noise that is originated in the interferometer by the coupling between the input laser jitter and the optics misalignments, as we are going to discuss in the next section of this Chapter. We will see that this noise affects the Virgo interferometer and imposes very strict statements to the optical alignment, and also it put serious limits to the improvement of advanced Virgo. Thus, the scope of our PhD work is to develop and to demonstrate the effectiveness of a novel control system, based on Adaptive Optics technique, which promises to solve the problem as it is able to significantly reduce this form of noise. All the details about this work of research will be discussed in the next Chapters of the present Thesis.

1.4 Noise from coupling of interferometer asymmetries with input laser beam jitters

We have seen that the fundamental noises limits the detectivity of Virgo interferometer and that the expected sensitivity curve reaches levels of about $\tilde{h} = 10^{-23} \text{ } 1/\sqrt{\text{Hz}}$ in the central band at 100 Hz. Nonetheless, to reach such extreme values, other kinds of noise must be assessed and suppressed, and among them there is the noise generated by the coupling between the interferometer asymmetries and the input laser beam geometrical fluctuations, or beam jitters.

The interferometer asymmetries can be interpreted as perturbations of the fundamental mode in each of the two Fabry Perot cavities put in the arms of the Michelson. This means that the spatial wave function of each arm is represented as the sum of the fundamental Gaussian mode TEM_{00} and of the higher order Hermite-Gauss modes TEM_{mn} of an ideal cavity. In the same way, the geometrical fluctuations of the input laser beam can be represented as fluctuations of higher order modes of a pure TEM_{00} beam perfectly matched to an ideal interferometer [45].

In order to understand how these two effects can couple and generate phase noise at the output of the interferometer, let us make reference to figure 1.6 which represents the scheme of a recycled Michelson interferometer with Fabry Perot cavities in the two arms.

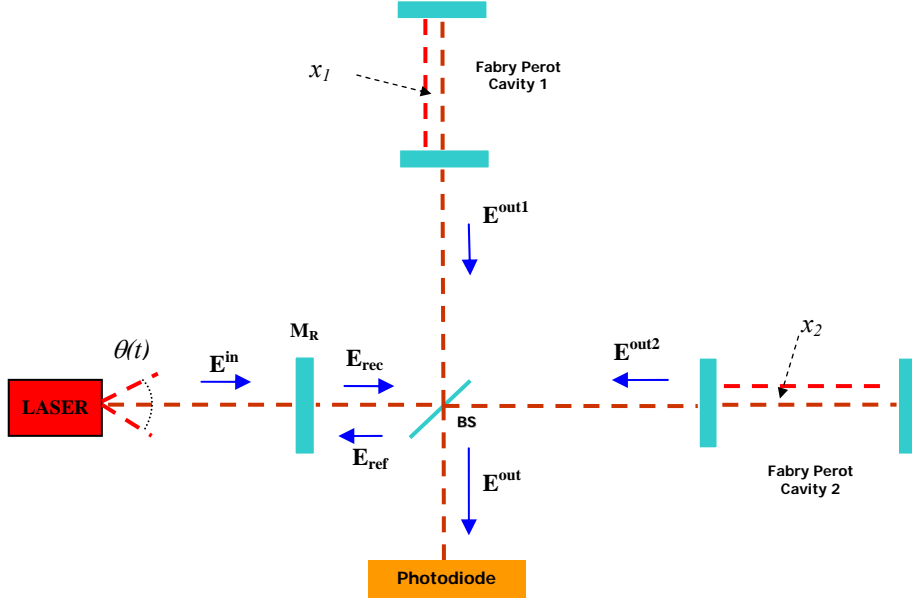


Figure 1.6: recycled Michelson interferometer with Fabry-Perot cavities in the two arms. In this picture we assume that the input laser beam has an angular jitter $\theta(t)$ while the two cavities have a lateral asymmetry x_1 and x_2 .

If we assume fixed the position of the recycling mirror and consider the misalignment as a lateral translation $x_{1,2}$ or an angular rotation $\theta_{1,2}$ of the optical axis of the two Fabry-Perot cavities 1 and/or 2, the modes Ψ_1 and Ψ_2 inside the cavities are perturbed at first order as:

$$\Psi_{tot}^{1,2} \approx \Psi_0 + \varepsilon_{1,2}^{t,r} \Psi_1 \quad (1.25)$$

where in the case of translation $\varepsilon_{1,2}^t = x_{1,2}/w_0$ and in the case of rotation $\varepsilon_{1,2}^r = i\theta_{1,2}(\pi w_0/\lambda)$, while w_0 and λ are the laser beam waist and wavelength respectively.

On the other hand, it has been demonstrated that the geometrical fluctuations of a laser beam can be interpreted as perturbations of the fundamental

Gaussian mode. So, a laser source of angular frequency ω_0 , affected by jitter, emits a perturbed beam which at first order can be approximated as:

$$E^{in} \approx A(\Psi_0 + \beta(t)\Psi_1)e^{i\omega_0 t} \quad (1.26)$$

being Ψ_0 the fundamental Gaussian mode and Ψ_1 the first order Hermite Gauss spatial mode. The perturbation coefficient $\beta(t)$ represents the geometrical fluctuation of the laser beam, and in particular it is $\beta(t) = \beta_l(t) = l(t)/w_0$ in the case of lateral beam jitter, and $\beta(t) = \beta_\alpha(t) = i\theta(t)(\pi w_0/\lambda)$ for the angular jitter. In these two last expressions we have used $l(t)$ and $\theta(t)$ as the lateral and the angular deviation of the laser beam from its optical axis.

Let us now consider, without loss of generality, the case when the two Fabry-Perot cavities are translated by an amount x_1 and x_2 and the input beam has an angular jitter of angular frequency ω , that corresponds to $\beta_\alpha(t) = (1/2)i\beta_0[\exp(i\omega t) - \exp(-i\omega t)]$, being $\beta_0 = \theta_0(\pi w_0/\lambda)$

From this last assumption, the incident field of eq. (1.26) can be represented as a vector of two components, the first one projected on the fundamental mode Ψ_0 , and oscillating at frequency ω_0 , and the second one projected on the mode Ψ_1 and oscillating at the sideband frequencies $\omega_0 + \omega$ and $\omega_0 - \omega$:

$$E^{in} = E_0^{in} + E_1^{in} = A\Psi_0 e^{i\omega_0 t} + A\Psi_1 i \frac{\beta_0}{2} (e^{i(\omega_0 + \omega)t} + e^{i(\omega_0 - \omega)t}) \quad (1.27)$$

The perturbed incident beam couples with the interferometer misalignment and then the field inside the recycling cavity is [46]:

$$E^{rec}(\omega_0 + \omega) = M(\omega_0 + \omega)E^{in}(\omega_0 + \omega) \quad (1.28)$$

where the two dimensional matrix M , calculated as a sum of all the reflections of the beam going forth and back in the interferometer, is:

$$M(\omega) = t_R \begin{pmatrix} \frac{1}{1 - r_R r_0 f(\omega) e^{i\varphi}} & \frac{\varepsilon}{2} \left(\frac{1}{1 - r_R r_0 f(\omega) e^{i\varphi}} - \frac{1}{1 + r_1 r_R} \right) \\ \frac{\varepsilon}{2} \left(\frac{1}{1 - r_R r_0 f(\omega) e^{i\varphi}} - \frac{1}{1 + r_1 r_R} \right) & -\frac{1}{1 + r_1 r_R} \end{pmatrix}$$

(1.29)

Here, $r_0 f(\omega) e^{i\varphi}$ and r_1 are the reflectivity of the Fabry Perot cavities for the mode Ψ_0 and Ψ_1 respectively, $f(\omega) \cong [1 + (c\omega/4\pi LF)^2]^{-1/2}$, $\varphi = 4LF\omega/\pi c$, c is the speed of light and $\varepsilon = \varepsilon_1 + \varepsilon_2 = (x_1 + x_2)/w_0$. And also, L is the cavity length, F the Finesse, r_R and t_R the reflectivity and the transmittivity of the recycling mirror.

From eq. (1.28) it is possible to calculate the two fields E^{out1} and E^{out2} outgoing the cavities and therefore their phase difference $\delta\theta$ at the output of the Michelson:

$$\delta\phi = \mathbf{Re} \left((\varepsilon_1 - \varepsilon_2) \beta_0 \frac{r_1 + r_0 f(\omega) e^{i\varphi}}{r_0} \frac{1 - r_0 r_R}{1 + r_1 r_R} \right) \quad (1.30)$$

which shows that the coupling between the misalignment of the interferometer $\varepsilon_1 - \varepsilon_2$ and the angular jitter of the input laser beam β_0 generates an additional phase noise into the system. Similar results can be demonstrated for the coupling between the angular misalignment of the cavities and the lateral jitters of the input beam.

1.5 Passive suppression and requirements for active prefiltering of the laser jitters

The phase noise calculated in eq. (1.30) suggests that if the laser geometrical fluctuations are not reduced, the necessity of achieving the sensitivity limit imposes very strict statements to the tolerance of the interferometer asymmetries. On the other hand, it is not very easy to assure that a large and complex structure like Virgo antenna, which is exposed to daily variation of the environmental conditions (wind, temperature, pressure, etc.), could maintain a perfect alignment for a long term period of several years. Therefore, since Virgo proposal, the suppression of the input laser beam jitters has been taken into account and currently it is passively performed by the *mode-cleaner* [47], a triangular Fabry-Perot cavity 144 m long with Finesse 1000 used in transmission between the input laser and the interferometer, as shown in Figure 1.7.

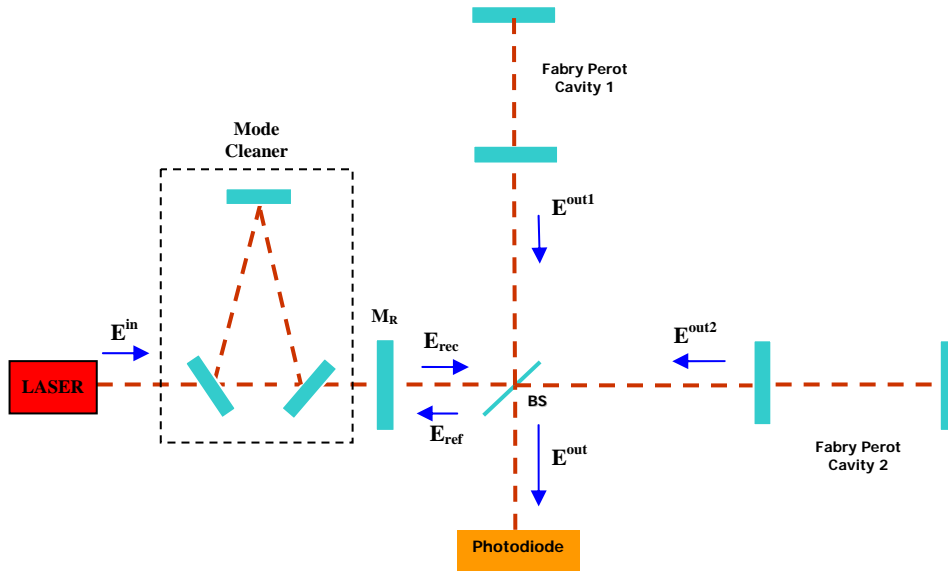


Figure 1.7: scheme of the Virgo interferometer and Mode Cleaner for the passive filtering of the input laser beam jitters.

The input laser beam is cleaned up because its initial jitters are interpreted by the triangular cavity as not resonant higher order modes and hence reflected back. The noise is reduced by the same order of magnitude of the cavity Finesse, that is by a factor 10^{-3} . Nevertheless, the residual fluctuations of the laser beam outgoing the mode-cleaner still impose very strict statements to the interferometer alignment, which is actually performed at an rms accuracy close to 10^{-9} rad at the best of the present technology.

The possibility of pre-filtering the laser beam would add a safety factor to the mode cleaner performances [48], [49], [50], and also would allow to relax the strict statements of alignment. Furthermore, a system able to better control the laser beam geometrical fluctuations could be used to correct the expected thermally induced aberrations in the next generation high power interferometers, so to assure suitable beam matching with mode cleaner [51]. In Advanced Virgo, where a 200 W laser will be used, the thermal effects are expected to strongly reduce the power coupled with the passive cavity. The consequent loss of power is assessed on about 90% , due to distortion caused by absorbing media in intermediate optics like the Faraday isolator.

A compensation of such effect can be obtained using negative expansion coefficient materials [52], but residual fluctuations of the low order Gaussian

modes still impose a further reduction with 40 *dB* at low frequency (< 1 *Hz*) in order to lower the power lost into higher order modes under 1%. This can be considered the first requirement for the design of a pre-filtering system.

Moreover, the phase noise of eq. (1.30) depends on the product of the coefficients of asymmetries times the coefficients of the higher order Gaussian modes of the perturbed input beam. In Virgo, typical values for asymmetry coefficients are about 10^{-3} and the phase detectivity limit corresponding to the sensitivity curve is $\delta\tilde{\phi} \cong 10^{-11} \text{ rad}/\sqrt{\text{Hz}}$, which means that the coefficients of the laser Gaussian modes of order 1 and 2 at the input of the interferometer must be less than $10^{-8} \frac{1}{\sqrt{\text{Hz}}}$, and therefore less than

$10^{-5} \frac{1}{\sqrt{\text{Hz}}}$ before the mode cleaner with modes suppression factor of 10^{-3} .

This means that the jitters noise reintroduced by the pre-filtering system before the mode cleaner must respect this upper limitation over the whole GW measurement band extending from 10 *Hz* to 10 *kHz*. In particular, for a beam waist of 1 *mm*, considering the TEM_{10} mode, the condition of a

coefficient $< 10^{-5} \frac{1}{\sqrt{\text{Hz}}}$ corresponds to an angular jitter $\tilde{\theta}_x < 3 \cdot 10^{-9} \frac{\text{rad}}{\sqrt{\text{Hz}}}$;

this limitation is generally satisfied by a quite laser beam in the frequency region above 100 *Hz*, but not in the tens of hertz, where an order of magnitude more has been measured [53]. Therefore jitters reduction of more than 20 *dB* is necessary in the spectral region up to few tens of *Hz*, and this can be considered the second important requirement for the correction of this kind of noise in interferometric GW antennas.

Several kinds of systems have been proposed to correct the laser perturbation in accordance to Virgo requirements. In particular, systems based on thermal deformation of mirrors or lenses have been demonstrated to work [54], but they need complex optical schemes, auxiliary high power lasers and exhibit the band limitations typical of any system using thermal processes. Alternatively, Adaptive Optics techniques have been explored for active pre-filtering of the laser beam, but the traditional systems based on the Shack-Hartmann sensor have shown serious limitations for this particular application where high sensitivity and wideband correction is required [55].

Starting from this context, we have investigated the possibility of implementing a novel Adaptive Optics system based on the interferometric detection of the wavefront.

Our system is proposed for the active prefiltering of the input laser beam in cascade with the mode cleaner as shown in figure 1.8.

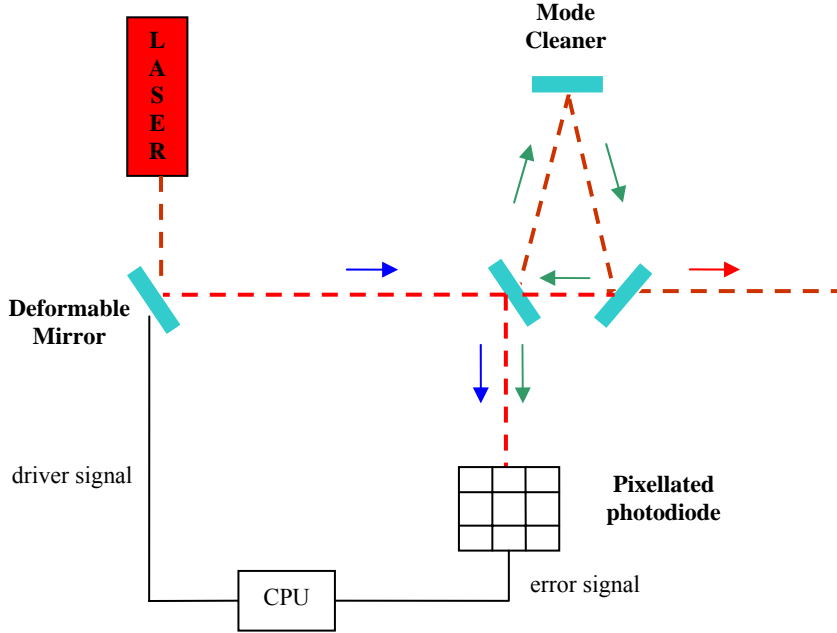


Figure 1.8: scheme of implementation of the proposed AO system in cascade with the mode cleaner to perform laser active prefiltering in Virgo antenna. The deformable mirror is the actuator of a typical feedback control where the error signal is extracted on the pixellated photodiode by the interference of the input laser beam (blue arrow) with the beam reflected back by the mode cleaner (green arrow) which contains all the higher order modes not resonant with the cavity. The Central Processing Unit (CPU) receives the error signal and generates the driver commands for the adaptive mirror.

In this configuration the AO system consists of a deformable mirror acting on the laser beam before the mode cleaner and of a pixellated photodiode used to detect the laser perturbation and provide the error signal to the central processing unit. Here the error signal is converted into the driver command for the deformable mirror, according to the typical configuration of closed loop control. The error signal is extracted on the pixellated photodiode by the interference of the input beam with the beam reflected back by the mode cleaner containing all the higher order modes not resonant with the cavity. In the following of the present work, after a short investigation of the Adaptive Optics technology that is currently available, we present the Project of our system and demonstrate that it fulfils the Virgo requirements for the active prefiltering of the input laser beam.

Chapter 2

Adaptive Optics

In this Chapter, we present the principal properties of the Adaptive Optics (AO), that is a technology developed in the last thirty years for wavefront control and light aberrations correction. We start with a short discussion about the phenomenon of aberration, showing the physical meaning in terms of geometrical optics and also in the wavelike approach, where aberration is described as perturbation of the wavefront surface. The aberrated phase profile can be expanded into a complete set of orthonormal polynomials named Zernike functions, which represent the fundamental modes of aberration.

After that, we make an overview of AO, ranging from the first approaches up to the most recent applications. In particular, we show the standard configuration of an AO system, the main components and the principle of operation for the automatic correction of the wavefront aberration. We discuss the traditional use of AO in astronomy and the novel applications in the fields of medicine and industry. Furthermore, we show how AO can help to control the laser optical characteristics, thus widening its possible application in the fields of telecommunications, remote sensing, industry, high precision measurements. Finally, we outline the state of the art of the technology and the future developments in which research is now committed.

2.1 Optical aberration and Zernike polynomials

In the theory of wave optics, diffraction sets an unavoidable limit to the resolving power of any imaging system, because for its effect a point like source is spread on the image plane into a finite size spot [56]. In order to improve the resolution, it is common to design the optical systems with diaphragms of aperture D very large compared to the wavelength λ of the incoming radiation [57]. In fact these is the only way to minimize the diffraction parameter λ/D which is proportional to the spread of the image, like in the case of the Airy's disk [58].

Nonetheless, in the geometrical model of the light propagation, when very large values of the transverse dimension D are used, the paraxial approximation is not valid anymore and this cause another effect of imaging degradation, that is the *optical monochromatic aberration* [59]. In fact, skew rays passing through wide apertures of the optical systems are focused into different points thus spreading the spot of the image. From an analytical point of view, the paraxial assumption allows to stop at the first order the power series expansion of the trigonometrical functions involved into the Snell's law [58]. On the contrary, if we consider rays with large divergence α from the axis, in the equation:

$$\sin\alpha = \alpha - \alpha^3/3! + \alpha^5/5! - \alpha^7/7! + \dots \quad (2.1)$$

we need to consider at least the third order term, or $\sin\alpha \cong \alpha - \alpha^3/3!$.

The third order theory brings to much more complicated formulas where the direction of the rays of light suffers of the five monochromatic primary (or Seidel) aberrations, that are well known as *spherical aberration*, *coma*, *astigmatism*, *curvature of field* and *distortion*. Higher order aberrations coming from the higher order terms of eq. (2.1) are usually neglected because of their very small effects. Optical systems based on refractive surfaces also suffer for chromatic aberration, due to the dispersion of light. This implies that the image of a not monochromatic source is focused by the system into different image points depending on the colour. This is called *chromatic aberration*.

In wave optics, aberration is described as the distortion of the light wavefront. In fact, the geometrical rays are everywhere perpendicular to the surface of the wavefront, and hence if their direction is modified by aberration, it is immediate to see that this corresponds to a variation of the wavefront profile. In figure 2.1 we compare the spherical wave and the plane wave in the ideal case and in the case of generic aberration.

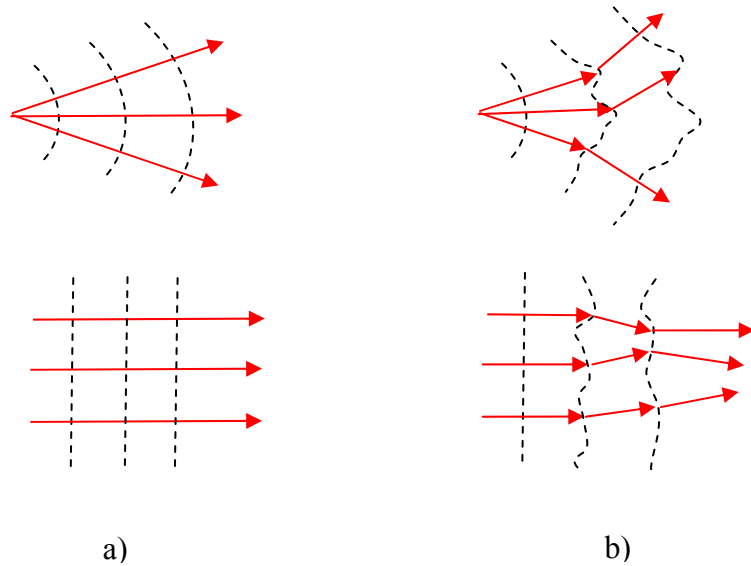


Figure 2.1: spherical wave and plane wave in the ideal case a) and with aberration b). It can be seen the deviation of the rays direction, and the distortion of the wavefront

In particular, the aberrated light wave emerging from the exit pupil of a convergent optical system has a perturbed wavefront which deviates from the ideal spherical profile (see figure 2.2).

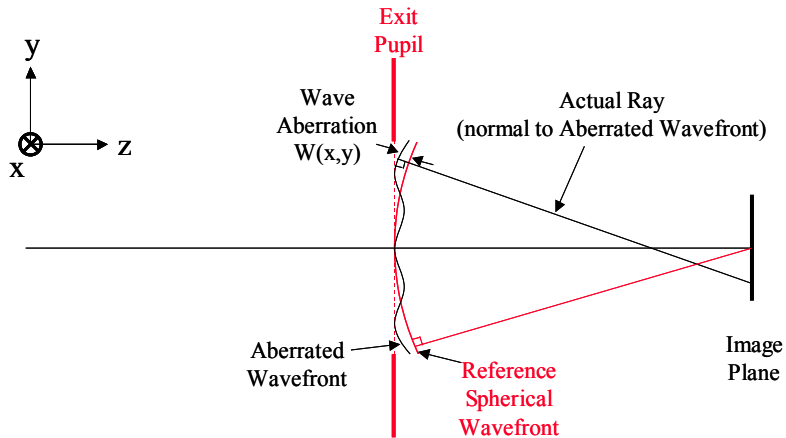


Figure 2.2: aberrated wave emerging from a convergent optical system and Wave Aberration Function

The perturbation of the wavefront is analytically represented using the *Wave Aberration Function*, or *Optical Path Difference* $W(x,y)$, which is the difference between the actual and the ideal wavefront in the plane transverse to the optical axis.

The Wave Aberration Function is represented in different sets of coordinates and it is expanded in different series of functions, depending on the symmetry and the geometry of the problem. A standard representation is the Taylor polynomial expansion in polar coordinates [60]:

$$W(r, \theta) = W_{020}r^2 + W_{040}r^4 + W_{131}r^3 \cos \theta + W_{222}r^2 \cos^2 \theta + W_{220}r^2 + W_{311}r \cos \theta + \dots \quad (2.2)$$

where W_{klm} are the wave aberration coefficients, r and θ are the polar coordinates in the transverse plane and the different terms correspond to the primary aberrations (defocus, spherical aberration, coma, astigmatism, field curvature and distortion respectively). The radial coordinate r is very often normalized to the radius a of the circular optical aperture (pupil) $\rho=r/a$. Higher order terms are usually neglected. The terms in the Taylor series do not form an orthogonal set of basis functions and are not recommended for data fitting of experimental measurements of wave front aberrations.

Instead, Zernike polynomials, so named from the scientist Frits Zernike who first used them in 1934 [61], form a complete set of functions or modes that are orthonormal over a circle of unit radius and are convenient for serving as a set of basis functions. This makes them suitable for accurately describing wave aberrations as well as for data fitting. They are usually expressed in polar coordinates, and are readily convertible to Cartesian coordinates. These polynomials are mutually orthogonal and therefore mathematically independent. Zernike polynomials $Z_{J,n,m}$ are normally expressed in polar coordinates (ρ, θ) where $0 \leq \rho \leq 1$ and $0 \leq \theta \leq 2\pi$. Figure 2.3 shows the coordinate system of the unit circle over which they are defined.

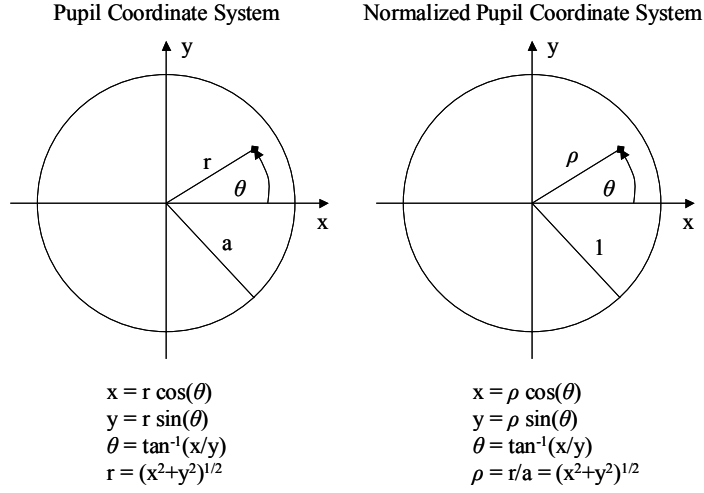


Figure 2.3: pupil coordinate system

So, in the two dimensional domain over the circle of unit radius $\rho=r/a$, each continuous function can be expanded as a linear combination of Zernike polynomials. This means that each phase front profile, whatever complicated, has a wave aberration function that can be expressed as a weighted sum of Zernike polynomials through suitable coefficients:

$$W(\rho, \theta) = \sum_{n=0}^k \sum_{m=-n}^{+n} W_n^m Z_n^m(\rho, \theta) \quad (2.3)$$

being k the polynomial order of the expansion and W_n^m the coefficient of the Z_n^m mode. Table 2.1 shows the mathematical expression of the Zernike polynomials up to the fourth order, and their physical meaning relative to the primary aberrations. The order of the polynomial is n , the number is J and m is the factor multiplying the angle θ .

The 0 order is a constant, and corresponds to a rigid translation of the wave front. The first order corresponds to the tip-tilt of the wave front, that is a rigid rotation around the x and y axis (being z the optical axis). The second and third order correspond to defocus, astigmatism and coma, while the fourth order represents spherical aberration and defocus. Figure 2.4 shows the surfaces of the first polynomials corresponding to basic optical aberrations. In the real case, the aberrated wavefront is a generic superposition of those fundamental modes

n	J	M	$Z_{J,n,m}$	<i>Aberration</i>
0	0	0	1	Costant
1	1	-1	$2\rho\sin\theta$	Tilt y, distortion
1	2	1	$2\rho\cos\theta$	Tilt x, distortion
2	3	-2	$\sqrt{6}(\rho^2\sin 2\theta)$	Astigmatism $\pm 45^\circ$
2	4	0	$\sqrt{3}(2\rho^2 - 1)$	Field Curvature, Defocus
2	5	2	$\sqrt{6}(\rho^2\cos 2\theta)$	Astigmatism $0^\circ, 90^\circ$
3	7	-1	$\sqrt{8}(3\rho^3 - 2\rho)\sin\theta$	Coma y
3	8	1	$\sqrt{8}(3\rho^3 - 2\rho)\cos\theta$	Coma x
4	12	0	$\sqrt{5}(6\rho^4 - 6\rho^2 + 1)$	Spherical aberration, defocus

Table 2.1: Zernike Polynomials

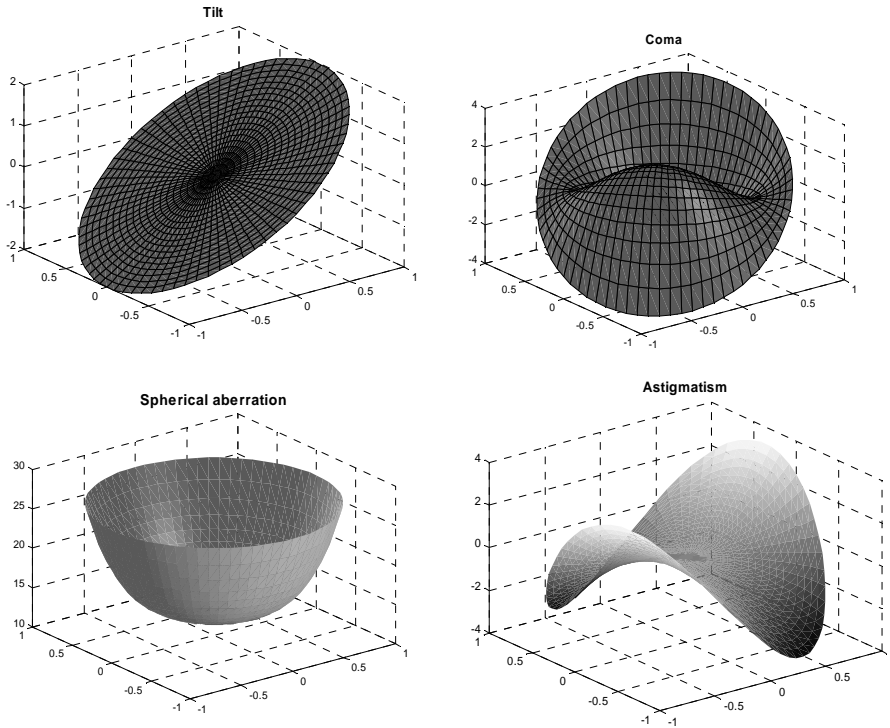


Figure 2.4: wavefront of the basic aberrations

2.2 Scheme and operation of a standard AO system

The static aberrations that affect the optical systems are nowadays well corrected by optical designers thanks to techniques of ray tracing simulation based on powerful software [62], [63]. Skilled technicians very often design high quality optical systems where the resolving power is close to the lower limit imposed by diffraction.

Nevertheless, stochastic phase front aberrations occur when light passes through non homogeneous and non uniform refractive materials, whose index of refraction randomly depends on space and on time, that is $n=n(r,t)$.

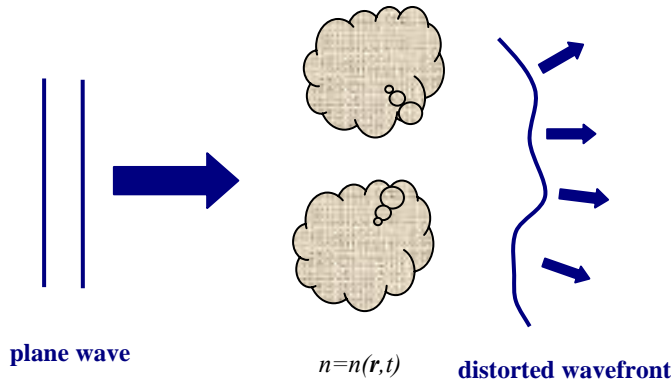


Figure 2.5: plane wave distorted by a non homogeneous refractive medium

Let us consider, for example, the star light which passes through the atmosphere of the Earth before being collected by the telescopes. Because of its turbulence, the index of refraction of the atmosphere has a stochastic time variation. Hence light coming from the stars, which in the ideal case should be represented by a perfect transverse plane wave, in the real case undergoes optical aberrations and reaches the detectors on the ground with perturbed wavefront.

Such stochastic and time varying aberrations cannot be statically compensated by the optical designer, but need a dynamical correction of the wavefront distorted during its optical path from the source to the detector. This correction is performed using sophisticated techniques developed in the 70's and called *Adaptive Optics (AO)* [64],..., [67].

Although several kinds of AO systems have been proposed in the last years, depending on the available technology, on the cost and on the specific

application, they are all based on a standard configuration where we recognize the main components and the fundamental mode of operation.

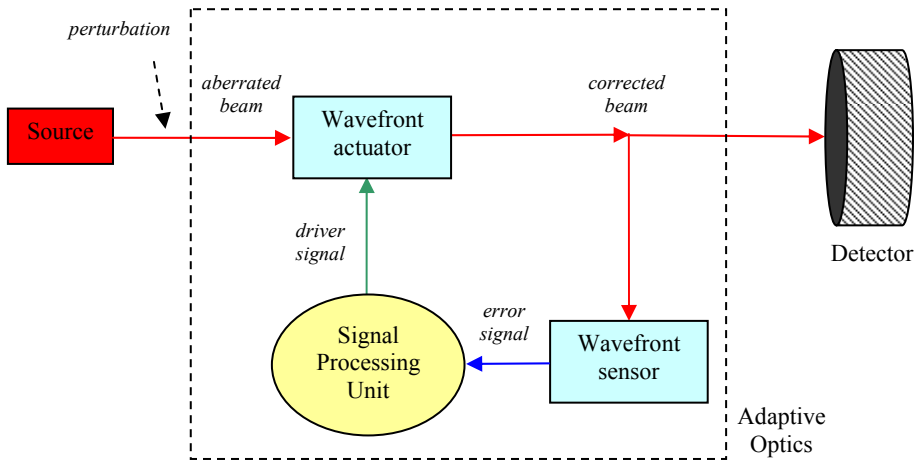


Figure 2.6: general scheme of an AO system. The light beam is corrected by AO while running through its optical path and reaches unperturbed the detector.

With reference to figure. 2.6, the AO system is represented in the dashed line rectangle and stands between the source and the detector for the wavefront correction. It is made of three main components that are the wavefront sensor, the wavefront actuator, and the signal processing unit.

The principle of operation is based on the typical scheme of a closed loop automatic control.

The incident perturbed beam is corrected by the wavefront actuator and then sent to the detector, apart from a derivation deviated to the wavefront sensor for the measurement of the phase front profile necessary for the generation of the error signal that is supplied to the central unit. Here the signal is processed and the measured phase profile is interpreted in terms of superposition of the Seidel aberrations. Usually the signal processing consists in the calculation of coefficients which best approximate the wave aberration function to the expansion in Zernike polynomials. Once the Zernike coefficients are calculated, the driver signal is sent to the actuator, which deforms the wavefront in such a way to compensate the original aberration. In fact, the profile forced by the actuator is the conjugate of the incident aberrated wavefront, obtained by applying weighted primary aberrations which are exactly the opposite of those measured by the sensor.

In such a way, AO acts as a feedback control system on several degrees of freedom for the simultaneous correction of the aberration modes.

2.3 Main components and operative parameters

We have seen that an AO system is made of three main components, which are required to implement the basic functions of an automatic control.

They are in particular:

1. the sensing element, for the measurement of the wavefront aberration
2. the actuating element, for the correction of the wavefront aberration
3. the reconstructor, made of a processing unit which acquires and processes the error signal from the sensor, and sends driver commands to the actuator for the phase front reconstruction.

In this section we present the general characteristics of the standard wavefront sensors and actuators; the processing unit is differently implemented depending on the typical application, and therefore discussion is delayed to the Chapter 3 where we present the specific processor designed for our AO system.

2.3.1 Wavefront Aberration Measurement

The wavefront sensor measures the discrepancy of the actual phase pattern from the ideal profile, that is the Wave Aberration Function.

The Shack-Hartmann sensor [66],[67],[68] is the standard method for wavefront sensing in AO, while other are techniques like the *shearing interferometry* [66],[67] are rarely used.

A schematic of the Shack-Hartmann system is shown in figure 2.7.

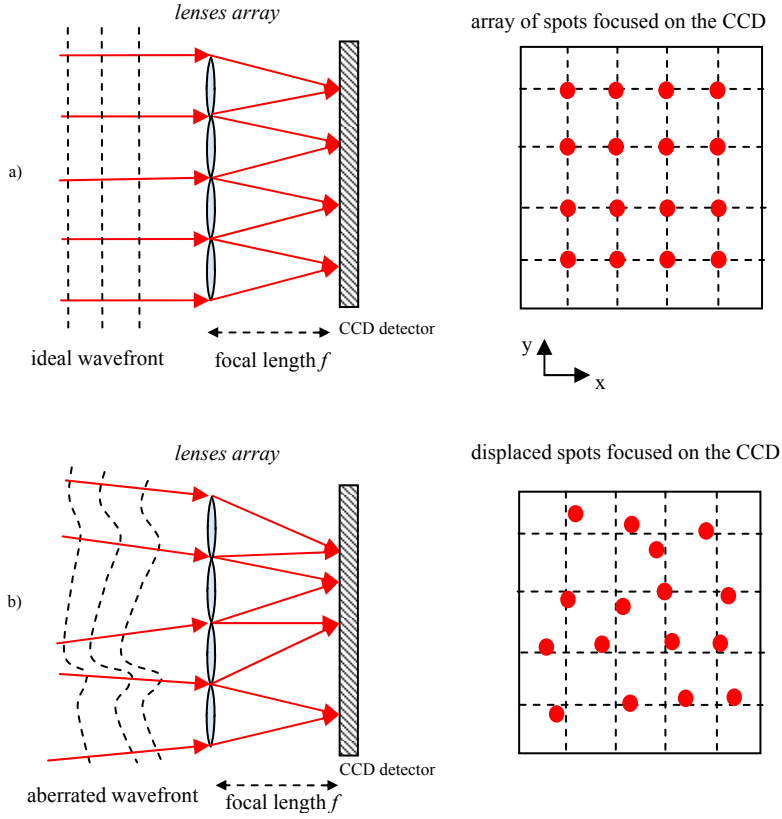


Figure 2.7: Shack-Hartmann Sensor and Lenses Array

The incident light beam is sent to an array of small identical lenses, and each one of them collects a part of the total beam and focuses it on the focal plane. The lenses lay all in the same transverse plane, and therefore the focal plane is the same, and corresponds to the sensitive surface of a light detector, typically a CCD. If the incident beam is an ideal transverse plane wave, all the spots focused on the CCD sensitive surface coincide with the ideal array of the focal points of the lenses, as seen in the case *a)* of figure 2.7. Instead, if the incident beam has an aberrated phase profile, the spots focused on the CCD have a displacement Δx and Δy from the ideal position, as showed in the case *b)*.

From the measurement of Δx and Δy it is possible to calculate the actual wave aberration function. In fact, let us consider the *centroide* C , that is position of one spot focused on the CCD. The two coordinates (x_C, y_C) of the *centroide*

are given by the weighted average of the intensities around the ideal reference position:

$$x_C = \frac{\sum_{i=1}^{N_x} \sum_{j=1}^{N_y} x_i I_{ij}}{\sum_{i=1}^{N_x} \sum_{j=1}^{N_y} I_{ij}} \quad ; \quad y_C = \frac{\sum_{i=1}^{N_x} \sum_{j=1}^{N_y} y_j I_{ij}}{\sum_{i=1}^{N_x} \sum_{j=1}^{N_y} I_{ij}} \quad (2.4)$$

In eq. (2.4) x_i and y_i are the coordinates of the single pixel of the CCD, I_{ij} is the corresponding intensity and N_x and N_y are the number of pixels around the ideal position which we use in the weighted average for the calculation of the centroid.

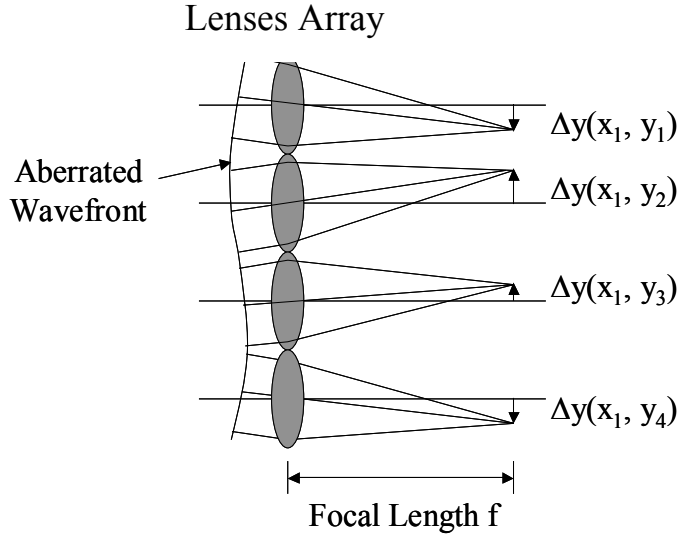


Figure 2.8: local displacement of the spot in a Shack-Hartmann wavefront sensor

The lenses array converts the local sections of the wavefront into focused spots at the CCD. If the incident wavefront is a perfect plane then the focused spots are not displaced from the optical axes of the various lenses. Instead, an aberrated incident wavefront produces a non-zero spot displacement. So for each lens there is an x -displacement, Δx , and a y -displacement, Δy , as shown in figure 2.8, where, for the sake of simplicity, we consider only the one

dimensional displacement Δy at fixed coordinate x_l . By simple trigonometrical considerations, it is easy to see that the displacement divided by the focal length of the lens is equal to the local slope of the wavefront function $W(x,y)$, or:

$$\frac{\partial W(x,y)}{\partial x} = \frac{\Delta x(x,y)}{f} \quad ; \quad \frac{\partial W(x,y)}{\partial y} = \frac{\Delta y(x,y)}{f} \quad (2.5)$$

Therefore, once the displacement data have been measured by the CCD, we can integrate the partial derivatives and obtain the Wave Aberration Function, which can be fit to a Zernike polynomial expansion like:

$$W(x,y) = \sum_j W_j Z_j(x,y) \quad (2.6)$$

The expansion coefficients W_j are determined by the scalar product of $W(x,y)$ with the corresponding Zernike polynomials $Z_j(x,y)$ and permit to estimate the total aberration in terms of normal modes.

2.3.2 Actuators for wavefront aberration control

The actuator of the AO system is a transducer for wavefront control. In terms of geometrical optics, this corresponds to change the optical path of the rays of light in such a way that some of them are retarded or anticipated in comparison to the others. This can be achieved using one of the two laws of refraction or reflection. In fact, by refraction we can modify the speed and the angle of light propagation, while using reflection we can lengthen or shorten the path of the rays, and also modify the direction. In both cases, the optical path is suitably changed in order to correct the phase aberration.

Techniques based on refraction make use of electro optic materials, such as liquid crystals, where we can change the index of refraction applying different levels of voltage. In this way, we can retard, in only some parts of the transverse plane, the rays of light, and therefore we achieve the necessary wavefront correction. A typical electro optic crystal is made of silicon

bismuth oxide ($Bi_{12}SiO_{20}$). Such kind of actuators present spectral absorption and index of refraction strictly dependent on the wavelength. So, high intensity monochromatic light can only be corrected using that technique, which is not commonly adopted.

On the contrary, actuators based on reflection are widely used and we can say that they are the only kind of transducers used in AO [69]. These actuators are essentially deformable mirrors, whose profile can be changed according to suitable geometry. In such a way, by assuming a transverse profile which is the conjugate of the actual wavefront profile of the incident light, the earlier rays must run a longer path under their reflection, and therefore the reflected wavefront is corrected by aberration.

Several technological solutions have been proposed for the implementation of deformable mirrors. In the current scenario, we find different models, depending on the cost, on the application and on the expected performances. A deformable mirror for telescope application, where a diameter of several meters is required, has different characteristics from a mirror used to compensate aberrations of a laser spot of few millimetres.

The first large scale mirrors proposed for astronomy had the reflecting surface made of discrete segments moved by pistons (segmented mirrors). In the earlier model, each piston moves its own segment ahead and back, while in more sophisticated systems each reflective part is moved by two or more pistons and can be tilted. So, it permits to achieve more complex mirror profiles which better match the requested pattern for correction. But, in any case, these actuators suffer for a loss of light energy in the gaps between the segments, and this is a serious limitation when low intensity light must be corrected.

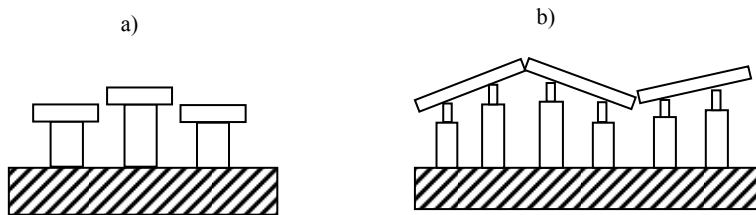


Figure 2.9: segmented a) single piston and b) multi piston deformable mirrors

Recently, small scale deformable mirrors have been built using MEMS (Micro Electro Mechanical System) technology [70], [71] for novel applications on micrometer scale such as the correction of the human eye

retina imaging in ophthalmoscopy. This kind of mirror has millimetric or sub millimetric reflective elements moved by piezoelectric actuators.

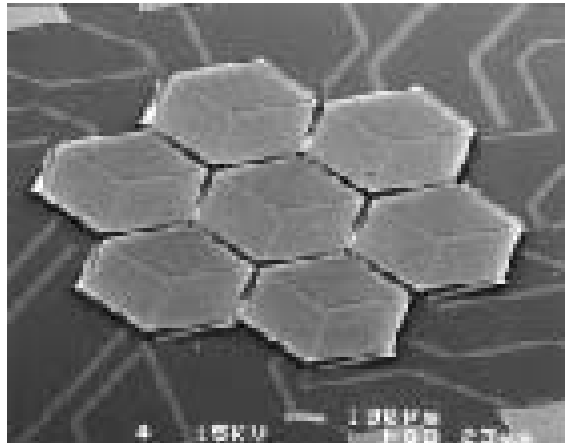


Figure 2.10: MEMS segmented mirror

Another class of deformable mirrors is made of continue reflecting membrane devices that are widely used in laboratory and industrial applications. The most common types are the micromachined membrane deformable mirror (MMDM), the piezoelectric deformable mirror (PZT) and the bimorph mirror (BM).

The first consists of a micromachined multilayer silicon nitride membrane covered with a special reflecting coating that is usually aluminium. It is based on the technology of silicon bulk micromachining and is suspended over an array of electrodes that locally deform the membrane for capacitive effect.

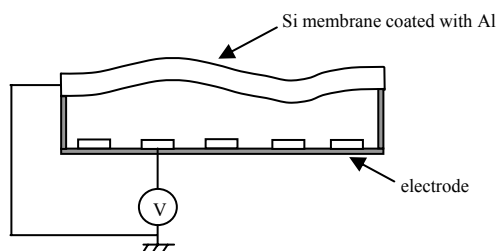


Figure 2.11: micromachined membrane deformable mirror (MMDM)

The PZT mirror is made of a reflective quartz plate with free edge, deformed by actuators of piezoelectric material, like lead zirconium titanate, which act as pistons, as they push or pull the membrane upon voltage application.

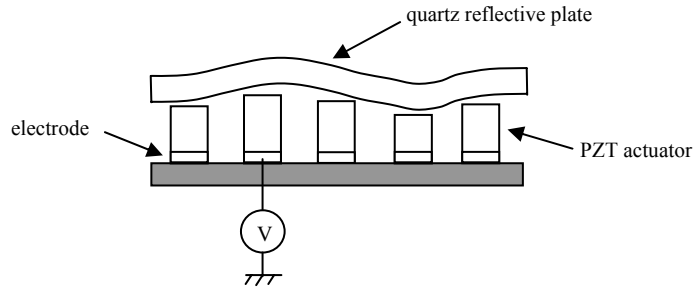


Figure 2.12: piezoelectric deformable mirror (PZT)

The bimorph mirror is made of two piezoelectric layers of ceramic lead magnesium niobate (PMN) actuated by electrodes on the back face and the front face, which induce an electric field into the material. For the presence of the electrical field, the PMN deforms and the reflecting surface assumes the desired profile.

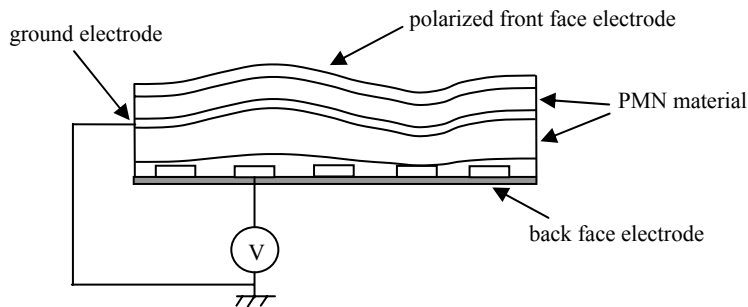


Figure 2.13: bimorph mirror (BM)

2.3.3 Operative parameters and performances of an AO system

Several parameters characterize an AO system in terms of operation and performance. Most of them have general validity and can be applied to any

system, while some others strictly refer to AO for telescopes, that for historical reasons is to date the reference field of that technology.

The *Fried parameter*, or *coherence length* r_0 , is the transverse dimension, at the input pupil of the imaging system, within which the wavefront is correlated. Fried's coherence length is a widely used descriptor of the level of atmospheric turbulence and depends on the atmospheric seeing conditions. This parameter is dependent on the wavelength of the incident light, according to the law $r_0 \sim \lambda^{6/5}$, and usually ranges between 10 and 20 *cm* for visible light.

The *isoplanatic angle* θ , in astronomy, is the maximum angle separating two coherent sources with the same wavefront perturbation. Therefore, in the case the original source which we want to correct it too weak, we can use a reference star within the isoplanatic angle to measure the wavefront aberration.

The *number of subapertures* N is the minimum quantity of wavefront samples necessary to obtain a good measurement of the aberration. It depends on the Fried parameter and on the aperture D of the system, following the rule $N \sim (D/r_0)^2$.

It is also very important the bandwidth of the automatic control which must be large enough to correct fast wavefront fluctuations.

In the table below we list typical values for a telescope of aperture $D=8$ *meters*.

λ (μm)	0.5	5	10
<i>Fried parameter: r_0 (cm)</i>	10	160	360
<i>Time to correction: τ (s)</i>	0.006	0.095	0.220
<i>Isoplanatic angle: θ (arcseconds)</i>	1.8	30	70
<i>Number of subapertures: N</i>	6400	12	4

Table 2.2: operative parameters of an AO system for a telescope of diameter $D=8$ meters

We see that the correction of visible light ($\lambda=0.5 \mu\text{m}$) sets very strict conditions, while Infrared (IR) and Far Infrared (FIR) ($\lambda = 5\div 10 \mu\text{m}$) allow to relax the statements.

In particular, we remark that for visible light, a bandwidth of the order of 1 *kHz* is required and a large number of subapertures (6400) must be provided

for the Shack Hartmann wavefront sensor. These two requirements are not easy to satisfy contemporarily, because if we increase the number of subapertures the processing unit has to calculate much more data, and this can result in a significative reduction of the bandwidth of the control speed. Therefore, a complex design should be provided for an optimized system. It is also worth noting that the isoplanatic angle is very small, which means that the low intensity of the star light is a critical issue; we will discuss this matter in the following section, as it refers to the specific case of AO for astronomy. The characterization of an AO system should also evaluate the residual errors of the components [64]. In particular, four sources of perturbation affect any AO system and are respectively the fitting, the temporal, the isoplanatic and the sensor noise error. The fitting error is due to the technology of the deformable mirror which cannot exactly match the shape of the distorted wavefront. The control bandwidth limits the correction of very fast aberrations and this induces temporal errors. In astronomical applications, isoplanatic error occurs when the wavefront beacon stands in a position not completely coherent with the target star. Finally, the sensor noise error is the intrinsic noise of the wavefront detector.

If we assume that these four errors are uncorrelated and have a Gaussian distribution, the total error of the AO system is expressed as the variance σ^2 in units of square radians as:

$$\sigma_{system}^2 = \sigma_{fitting}^2 + \sigma_{temporal}^2 + \sigma_{isoplanatic}^2 + \sigma_{sensor_noise}^2 \quad (2.7)$$

To evaluate the fitting error, we must consider that the more Zernike modes are corrected into the deformable mirror, the better the geometry of its surface matches the conjugate pattern for the wavefront compensation. Thus, if N_{Zern} is the number of completely corrected Zernike modes, the rms of the fitting error is:

$$\sigma_{fitting} = \frac{\sqrt{0.2944 N_{Zern}^{-\sqrt{3}/2} \left(\frac{D}{r_0} \right)^{5/3}}}{2\pi} \quad (2.8)$$

being D the aperture diameter and r_0 the Fried parameter as usual.

If we plot the fitting error against the number of corrected Zernike modes, we see that using the first 10÷15 modes is enough to achieve the lowest possible level of error.

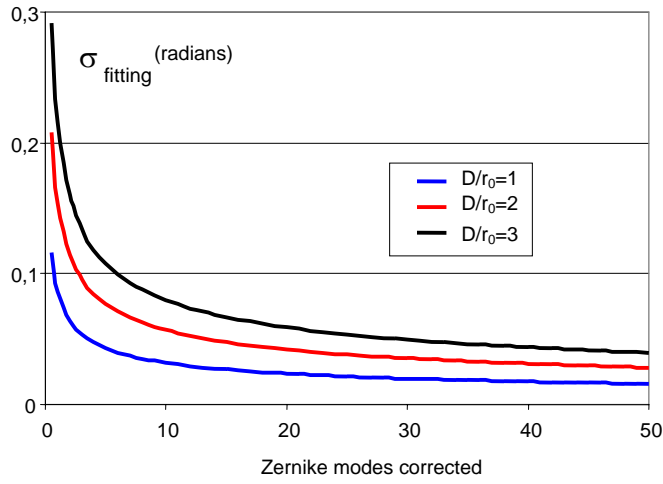


Figure 2.14: residual fitting error

The temporal error is related to the control bandwidth f_{3dB} and to the frequency f_0 of the aberration according to the following equation:

$$\sigma_{\text{temporal}} = \left(\frac{f_0}{f_{3dB}} \right)^{5/6} \quad (2.9)$$

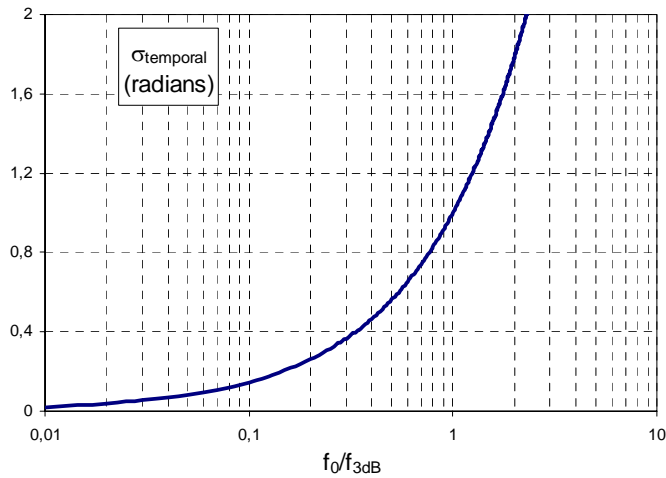


Figure 2.15: residual temporal error. f_0 frequency of the aberration, f_{3dB} bandwidth of the control system

From figure 2.5 we see that if the control bandwidth is higher than 10 times the perturbation frequency, that is $f_0/f_{3dB} < 0,1$, the residual error drops below $0,1$ radians.

The isoplanatic error is related to the distance Δx between the target star and the reference beacon. If D is the optical aperture and L the distance of the target from the sensor, the residual error for isoplanatic effect is:

$$\sigma_{isoplanatic} \approx \left(\frac{D}{L - \Delta x} \right)^{5/6} \quad (2.10)$$

The error, as expected, decreases with decreasing Δx , which occurs when the beacon get closer to the object.

Finally, the Shack Hartmann sensor introduces the following noise:

$$\begin{aligned} \sigma_{sensor_noise} &= \frac{2.96}{SNR} \left[2.25 + \left(\frac{\theta D}{\lambda} \right)^2 \right]^{1/2}, & r_0 > D \\ \sigma_{sensor_noise} &= \frac{2.96}{SNR} \left[2.25 \cdot \left(\frac{D}{r_0} \right)^2 + \left(\frac{\theta D}{\lambda} \right)^2 \right]^{1/2}, & r_0 < D \end{aligned} \quad (2.11)$$

with SNR Signal to Noise ratio of the sensor, D aperture of the imaging system, r_0 Fried parameter, λ wavelength and θ angular size of the source.

For a coherence length $r_0 = 10cm$, and a wavelength $\lambda = 0.5 \mu m$, two curves are plotted in figure 2.16 for two values of the Signal to Noise Ratio

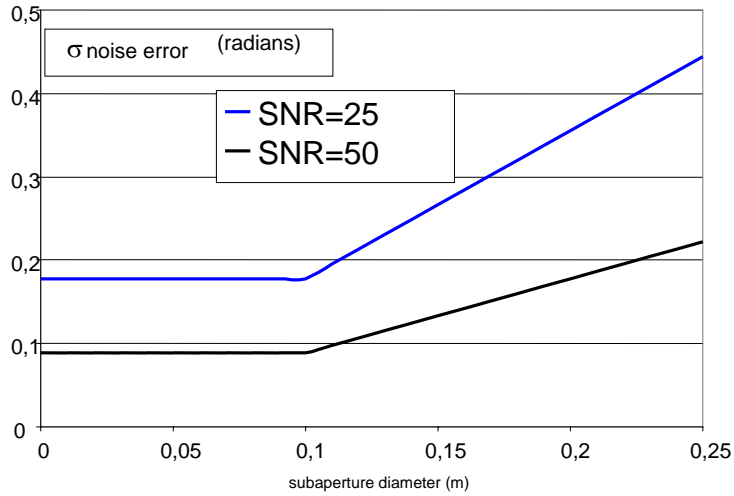


Figure 2.16: residual noise sensor error

We can see that the error induced by the sensor noise can be lowered using an high SNR and a subaperture diameter D smaller than the coherence length. For more details, which clearly overcome the scope of the present work, the interested reader is addressed to the referred bibliography.

2.4 Fields of application of AO

The first known Adaptive Optics system in the history was made in 212 BC, during the Syracuse siege, when Archimedes had the idea of using mirrors to focus the sun light and burned Roman ships. This was also the first use of Optics for Military applications.

Several centuries later, in 1730, Newton in his work *Optiks* wrote that Telescopes could not improve their performance and overcome the limitation of producing blurred images from astronomical objects, because of the turbulence of the atmosphere that distorts the wavefront of the light coming from the stars.

Nevertheless, even if the problem of the atmosphere blurring was know, there was not any technology able to solve the problem and only two centuries later, in the middle of 1900, Adaptive Optics was seriously investigated as a technology effective for the correction of the aberration in imaging systems.

Babcock first proposed AO in 1953 [72], but much of the technology remained classified by the Department of Defence of the United States and only after the declassification in 1991 the scientific research started a complete investigation.

Astronomy and Telescopes

The first non military application of AO has been in the field of astronomy and nowadays several large telescopes have been fitted with AO systems [73],[74].

The atmosphere is a mass of air which envelops the Earth and, due to the turbulence, is a not uniform and not homogeneous medium of propagation for light. This means that the index of refraction varies in time and in space along the path passed by the rays of light running from the stars to the ground telescopes.

This affects the quality of the image collected by the detectors and then reduces the resolving power much below the limit of diffraction. So, while in an ideal telescope the angular limit of detection α is given by the input pupil diameter, in a realistic uncorrected telescope, atmosphere blurring dramatically increases α as:

$$\alpha = 1.22 \frac{\lambda}{D} \rightarrow 1.22 \frac{\lambda}{r_0} \quad (2.12)$$

where r_0 is the Fried parameter that replaced the diameter D .

This means that, although we spend much money and realize a large scale telescope with 8 m diameter to get the angular resolution $\alpha = 1.5 \cdot 10^{-2}$ *arcseconds* given by normal diffraction, the actual value, in the best atmospheric seeing condition $r_0=20\text{cm}$, is not less than 0,6 *arcseconds*.

One possibility to overcome this problem is to implement space telescopes like Hubble which orbit outside from the Earth and therefore are not affected by atmosphere blurring. But, such kind of telescopes requests high technology much money for the construction, the commissioning and the operation.

On the other hand, ground telescopes have widely increased their performance using Active and Adaptive Optics, and nowadays they reach the best possible resolution with costs widely lower than those necessary for space detectors.

In general, even if a good design avoids most of the static aberrations discussed in Chapter 1, the quality of the image in terrestrial telescopes is still affected by two types of problems.

First of all, there are several quasi static disturbances due to the intrinsic nature of the experimental set up. In fact, perturbation of the image for loss of the focus, decentralization and deformation of the optical elements can be caused by mechanical, thermal and optical effects.

Nowadays, a suitable design and construction of the whole system, where several conditions are strictly respected, assure that the optical performances are long term maintained against the aging and the environmental perturbations. In particular, it is important the choice of high quality components, with high mechanical stiffness and low thermal expansion. Also, attention must be put in order that components dissipating heat (like motors and power electronics) must stand far from the optics, and that the whole system, once aligned, is protected from wind by the use of covers. Unfortunately, such structural adjustments are very expensive, especially for the large size telescopes that have been built in these last years, with primary mirrors of 4 meters necessary to collect as much optical power as possible.

The solution to relax the strict statements of the structure and in the same time to assure the quality of the image against the quasi static perturbation has been found by using Active Optics. This technology is based on the idea of installing into the telescope some optical elements which are autocorrective, as they can automatically compensate the slow deviation from the initial optical alignment. The quasi static nature of the perturbation allow to use elements moving at very low frequencies, typically 0.05Hz or less.

Telescopes using Active Optics are the 3.5 m diameter New Technology Telescope ESO at La Silla (Cile) since 1989, the 10 m primary mirror Keck Telescope at Mauna Kea , Hawai since 1992 and the four 8.2 thin mirrors VLT operating at Paranal (Cile).

In addition, Adaptive Optics has been applied to these telescopes for the dynamic correction of aberrations induced by the turbulence of the atmosphere. Figure 2.17 shows the schematic of a typical AO system for telescope.

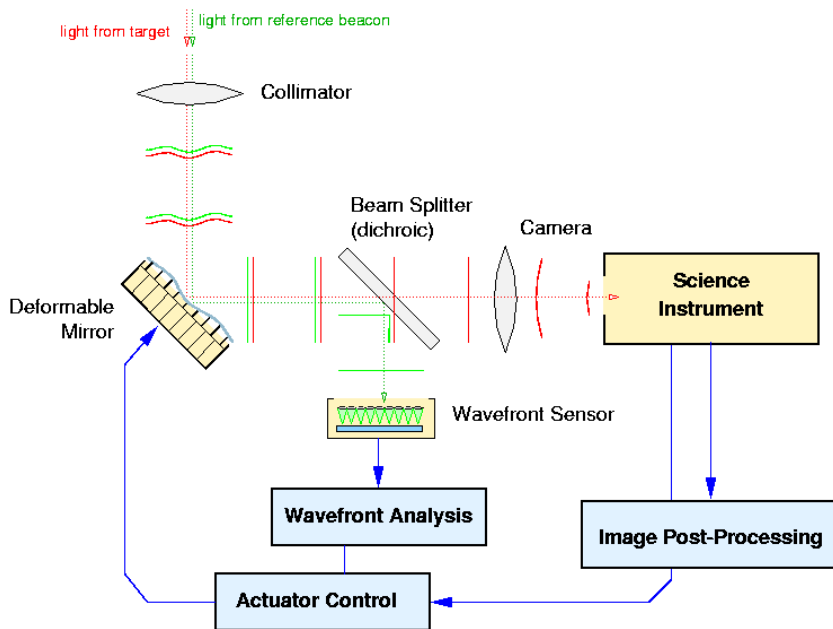


Figure 2.17: schematic of an Adaptive Optics system for telescope

The initially plane wavefront, travelling 20 km through the turbulent atmosphere, is strongly perturbed and, across the diameter of a large telescope, the phase error can be several microns large. In a typical case AO should detect low intensity star light and correct a minimum wavefront distortion of 1/50 micron in 1 kHz bandwidth. This statements require a very sophisticated and performing system.

Because of the weakness of the target, it is common to collect light from a reference star of sufficient intensity, provided that it stands within the isoplanatic angle. In this case, the light from the reference beacon, usually named *Natural Guide Star (NGS)*, is deviated by a dichroic beam splitter to the wavefront sensor. The control system sends the deformable mirror the actuator commands so that the light of the target, although of low intensity, can reach the detector with a corrected phase profile.

As the isoplanatic angle for visible light is very small, unless the telescope is directed to a big cluster of stars, the probability of finding a coherent Natural Guide Star is not more than 0,5%÷1%.

Advanced AO systems are promising to overcome this limitation using artificial reference stars, also referred to as *Laser Guide Stars (LGS)* [75].

The proposed method is to direct a pulsed laser beam to the sodium atoms present in mesosphere, at an altitude of about 90 km, and to collect the back scattering produced by those atoms as they go into resonance with the laser light. Alternatively, the laser beam is focused at an altitude of 20 km and excites molecules and particles located in the low stratosphere; also in this case back scattering occurs for Rayleigh diffusion and the artificial reference star is made. Such a method allows to achieve the beacon very close to the astronomical target, and the scattered light is deviated to the wavefront sensor to produce the error signals.

The diameter of the deformable mirrors usually does not exceed 20 cm and the number of actuators (usually piezoelectric pistons) is chosen upon a trade-off between the precision of the correction and the budget. Difficulties and costs rapidly increase passing from IR to the visible light. In fact, for an astronomical object emitting IR radiation, an 8 meters diameter telescope achieves a near perfect correction with only ten actuators. Instead, for visible light over 6400 pistons are required, and the same number of subapertures for the wavefront sensor, which in turn should be very sensitive and low noise in order to detect the perturbed wavefront of the weak reference beacon.

Also, the processing unit has strict statements which correspond to costly hardware and software. To get an idea of the high capacity of calculation required, let us consider that for IR light correction the processor must elaborate per each millisecond a set of about ten commands to send to the actuator; the number largely increases for visible light correction, as in this case in the same meanwhile of one millisecond the processor must elaborate a set of 6400 commands, which means its computing power must exceed several billion operations per each millisecond. It is clear to the reader how difficult and expansive is to realize such performing systems.

Anyway, the use of AO in ground telescopes has been widely diffused in the recent years, and the quality of the images has reached the limit of diffraction for IR radiation and is near to for visible light too. Some images from ground telescope are even better than those collected by space telescopes, as we can see in figure 2.18, where we see that Keck Telescope with AO produces an image of Titan, Saturn's largest moon, with a quality higher than the image produced by Hubble Space Telescope.

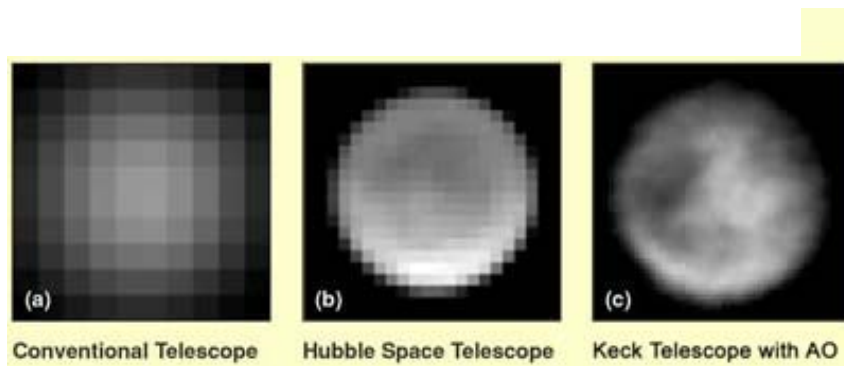


Figure 2.18: image of Titan, Saturn's largest Moon, by a) conventional telescope, b) Hubble Space Telescope and c) Keck Telescope with AO

New fields of application

AO is being investigated for application to new interesting fields, such as biomedical imaging, industrial processes and laser control [76]. In the recent years, AO systems have been integrated into commercial products, including cameras, CD players and large TV screens.

Following is a list of the principal applications that one can find in the current scenario.

- Medical imaging
 - ophthalmoscopy, Vision Science
 - oncology
- Consumer goods
- Industrial processes, quality control, metrology
- Laser control for
 - communication
 - high precision measurements in big experiments like gravitational wave detection
 - environmental monitoring

The detailed discussion of each of these fields is clearly beyond the core of our work, so stop our attention to some of the applications that our experimental facility could be proposed to.

Many people are increasing their interest in AO for medical imaging, and in particular its applications to ophthalmoscopy and Vision Science, where

important results have already been achieved [77], [78]. Several institutes are following this field of research and development, especially in U.S., like the Center for Adaptive Optics at the University of California, the Center for Visual Science, at the University of Rochester [79], and also at the University of Huston. Novel ophthalmic instruments equipped with AO have been demonstrated and are now in use by clinicians.

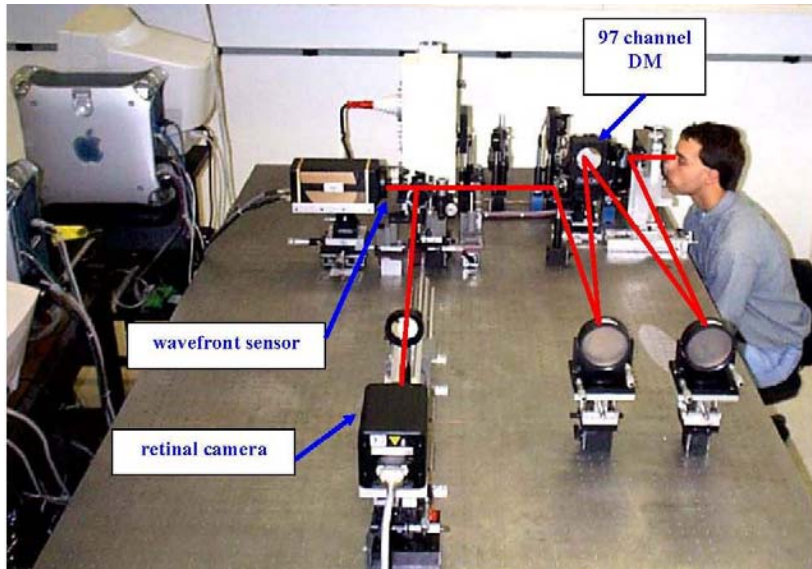


Figure 2.19: experimental AO set up for ophthalmoscopy at the University of Rochester

Two main goals are expected from the application of AO to human eye sciences: the vision correction and the retina imaging.

Vision Science is committed to the vision improvement. Traditional technology only operates standard correction on defocus and astigmatism, while AO systems are expected to achieve higher order aberration reduction tailored to individuals. Some people say that one day AO will enable “super” vision, giving eye more capability it has in normal condition [80].

The ability of AO to correct the monochromatic aberrations of the eye has also induced scientists and clinicians to investigate new opportunities to image *in vivo* the normal and diseased retina at unprecedented spatial resolution [81],...[84]. Currently, in the traditional *in vivo* retina imaging performed by ophthalmoscopes (fig. 2.20), it is not possible to achieve a spatial resolution below $5\ \mu m$, and this does not allow to clearly detect the fundamental elements of the retina, that are rods and cones whose dimensions are about $1\ \mu m$.

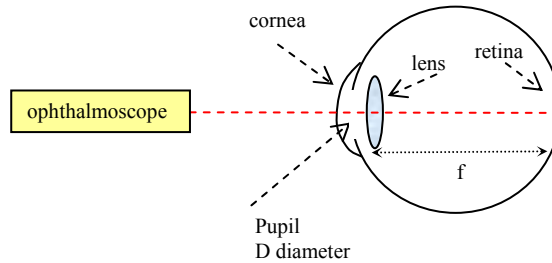


Figure 2.20: ophthalmoscopy of the human eye

The protective outer called *cornea* is transparent and allows light to enter the eye through the *pupil*, the circular opening in the center of the front part, larger or smaller depending on the light brightness. The probe beam entering the pupil passes through the *lens* and is focused on the *retina*, which is innermost layer in the eye. It converts images into electrical impulses that are sent along the optic nerve to the brain where the images are interpreted. The retina can be compared to the film of a camera. It is composed of light sensitive cells known as rods and cones interconnected by a complex mesh of neurons that provide early stage visual processing. Rod cells are primarily in the outer retina, do not discriminate colours, have low spatial resolution, support vision in low light (“night vision”), are sensitive to object movement and provide peripheral vision. Cone cells are densely packed within the central visual field, function best in bright light, process acute images and discriminate colours.

This optical system has a spatial resolution limit of $5\ \mu\text{m}$ set by the law of diffraction, $r = 1.22f\ \lambda/D$, being $\lambda \sim 0.5\ \mu\text{m}$ the wavelength of the probe light, $f \sim 17\text{mm}$ the focal length and $D \sim 2\text{-}3\ \text{mm}$ the normal aperture of the pupil. This is also the resolving power of the ophthalmoscope which interrogates the eye using the back scattered light of the beam focused on the retina. If we want to minimize the diffraction, we need to force the patient to enlarge the pupil up to $7\ \text{mm}$. In the ideal case, we would obtain a resolution $r \cong 1.5\ \mu\text{m}$, small enough to detect the retina’s details. But, in the real case, the enlargement of the pupil causes the retina imaging to suffer for ocular aberrations, and also for vibrations of the eye which stands in a not natural position. This effects limit again the resolution to about $5\ \mu\text{m}$.

The application of AO to the novel ophthalmic instruments allows to correct aberration and achieve the spatial resolution of $1\mu m$. The retina imaging is largely improved, as shown in the figure below.

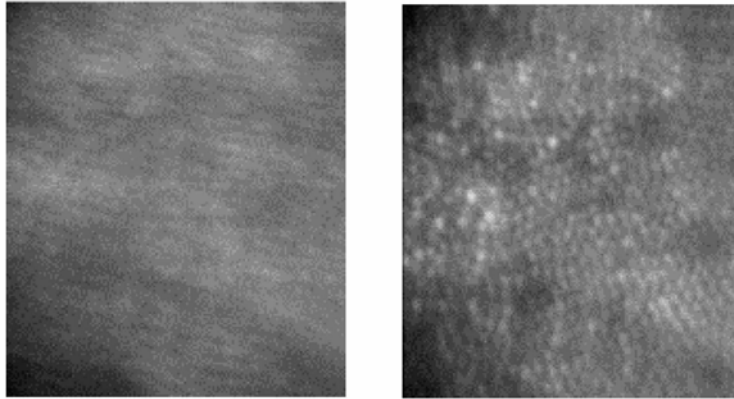


Figure 2.21: images of the human retina without (left) and with AO (right). Photoreceptors are clearly visible in the corrected image.

Other fields of biomedical imaging like oncology are getting advantage by application of AO to the diagnostic devices. The improved resolution in the detection of small details of the human body can help in the early diagnosis of cancer.

Interesting applications of AO have been demonstrated in the field of industry, especially for metrology and quality control. AO techniques have been adopted to measure the flatness of silicon wafers through the measurement of the wavefront distortion of the light beam reflected back by the wafer surface. The same method could be used for dynamic measurements of vibrating surfaces, provided that the bandwidth of the system is wide enough to follow the fast variations of the vibrating profile.

The quality control can also be extended to the environmental monitoring, where AO has been proposed to measure flows of particles, gases and heat, detected by the variation of the index of refraction that they produce in air.

AO is also applied to free space optical communications, where lasers are used in air between two optical fiber networks [85]. In fact lasercom systems for distances of several km are affected by beam spreading and scintillations induced by the atmospheric turbulence. Such problem cannot be compensated increasing the optical power because of eye safety and power consumption limitations, while considerable improvement is expected using AO correction.

Laser shaping is also performed by AO techniques, to improve the beam collimation and reduce the geometrical aberrations. This can help in industrial fields where high power lasers are used for cutting, welding and fusion.

2.5 State of the art and future outlooks of the AO technology

So far, we have presented an overview of the current technology of AO, showing the principle of operation, the main components, the classical use for astronomy and the new fields of applications.

We like now to finish this chapter with a summarize of the future expected advances, which promise to be very interesting in the next years, as they involve not only the basis research in Physics, but also the technological development and the industrialization where Engineering is committed.

Many technological challenges regard the AO for astronomy, where the main problems as seen before concern with the low brightness of the target star, the necessity of small phase correction (1/50 micron), the rapid variation of the wavefront due to the speed of the atmosphere turbulence ($\tau < 1$ ms), the small percentage of the sky covered by the isoplanatic angle at visible wavelength and the large dimensions of the mechanical structures in Very Large Telescopes (VLT) which require primary mirrors exceeding 8 m, big and costly hardware components, and powerful processing units.

R&D has undertaken to develop fast and low noise detectors in order to sense faint reference stars and very fast processors exceeding $10^9 \div 10^{10}$ operations per each millisecond.

Particular attention is dedicated to the improvement of the Deformable Mirror of large diameter over 30 cm and driven by thousands of actuators. It is clear that at the best of the present technology the speed of response of the deformable mirror is the principal limit to the bandwidth of the whole control system, as the sensor transfer function can be considered absolutely flat over 10kHz, and big improvements have already been obtained in the velocity of the processing unit. The new generation of mirrors promises to reach bandwidths of several kilohertz.

As concerns the methods for artificial reference beacons, LGS technology is now operating with high power reliable sodium lasers at a number of Observatories, but routine demonstration of their potential for getting very high sky coverage has not yet been achieved. A new advanced technique, called Multi-Conjugate Adaptive Optics (MCAO), which would permit to

obtain in the same time 3D data (2D spatial and 1D spectral information) is still in its initial experimentation.

At the University of Durham, it has been started a project of research called *FAOS-Future Adaptive Optics Systems* which is a collection of initiatives investigating the possibility of hardware improvement for AO systems. In fact, they consider that the requirement of evolution in CPU power for future AO systems surpasses the CPU scaling predicted in the ordinary HW/SW technology, and therefore they want to match the traditional software AO control loops with dedicated hardware acceleration to improve price, performance and physical size tradeoffs. They assess high speed (10kHz), compact and highly embedded AO systems.

AO techniques have allowed remarkable results in Vision Science for high resolution imaging of the human eye, and in particular to obtain in vivo images on the micrometer scale for earlier diagnosis and treatment of retina diseases. The key component of AO for Vision Science is the adaptive mirror, which must have operative parameters, size and cost very different from those traditionally implemented for telescopes. In particular, deformable mirrors for astronomy are expensive, costing \$ 100.000 for a 100 channel system, and have large apertures of the order of 10÷30cm. Moreover, they have a maximum central deflection of about 5 μm , which is usually sufficient for the wavefront correction of the star light. On the contrary, deformable mirrors for Vision Science should have an aperture comparable with the eye's pupil (~ several millimetres), should be compact, low cost, and capable of moving at least 12 μm to correct the defocus of the eye which can reach peak to valley wavefront errors of up to 25 μm (the effect of correction is doubled on reflection). In order to fulfil these strict statements, recently it has been proposed to make use of the MEMS – Micro Electro Mechanical Systems technology, which promises very low cost, high reliability, integrated into chips and performing mirrors. Texas Instruments has realized a digital micromirror device comprising 1 million mirror segments; it is a high technology microsystem, used for high quality displays, but cannot be used for AO because of its bistable nature. Indeed OKO-Flexible Technology manufactures a family of Micromachined Membrane Deformable Mirror (MMDM) [86], [87] based on the silicon bulk micromachining technology [88], [89]. It has a membrane electrostatically driven by an array of actuators and is suitable for AO application to Vision Science, because it has a diameter of the order of 1 cm, reaches central deflections of the order of 10÷15 μm and has a bandwidth up to 500 Hz. We will come back to this argument in the following, as we have adopted one of MMDM mirrors produced by OKO in our experimental prototype. Liquid Crystal Devices

[90] are also investigated for wavefront actuator implementation, as they perform very high spatial resolution and then permit to correct higher order aberration modes.

Many AO applications are being also explored in the field of consumer goods, such as display and data storage devices, as well as in the field of quality control of industrial processes (metrology, imaging through turbulent media, etc). Clearly in this case the strong effort is not only devoted to improve the operative performances, which are usually sufficient, but also and mainly to realize a low cost, compact and reliable device within a reliable supply chain, in accordance with typical concepts of industrial engineering.

In Table 2.3 we summarize the main issues here discussed per each field of application.

Field of application	Current issues and expected advances
<i>Astronomy</i>	<ul style="list-style-type: none"> ➤ big and costly structures, powerful CPU ➤ fast and very low noise detectors for fainter reference stars. ➤ very fast processors exceeding $10^9 \div 10^{10}$ operations per each millisecond. ➤ Deformable Mirror of 30cm diameter, 10^3 actuators, bandwidth over 1kHz. ➤ Laser Guide Star (LGS) for very high sky coverage ➤ Multi-Conjugate Adaptive Optics (MCAO) for 3D data ➤ <i>FAOS-Future Adaptive Optics Systems</i> Project at the University of Durham
<i>Vision Science</i>	<ul style="list-style-type: none"> ➤ deformable mirrors traditionally developed for large telescopes ➤ aperture comparable with the eye's pupil (\sim several millimetres) ➤ compact, low cost ➤ maximum deflection over 12 μm ➤ MEMS technology ➤ Liquid Crystal Devices: high resolution, spectral absorption
<i>Consumer goods and industrial processes</i>	<ul style="list-style-type: none"> ➤ low cost, compact and reliable devices ➤ reliable supply chain
<i>Laser beam control</i>	<ul style="list-style-type: none"> ➤ manipulating the shape of high power lasers for industrial processes ➤ lasers for communication systems ➤ reduction of laser jitter noise in the Virgo detection bandwidth $10\text{Hz} \div 10\text{kHz}$.

Table 2.3: future developments of Adaptive Optics

Chapter 3

Project of the Adaptive Optics system based on interferometric techniques for the automatic control of laser beam jitters in air

We have seen that the applications of AO in the recent years have gone beyond the classical use of astronomy and have entered several fields of science and technology, giving significative benefits to imaging systems where optical quality is a strict statement. We have also seen that interesting outlooks are expected from the implementation of AO to the laser control, as the possibility of manipulating the intensity profile will open new scenarios in the field of high power lasers for industrial processes and in the field of laser based communications.

Nevertheless, even if performing AO systems have already been achieved and new ones are promised to be developed in the next future, none of them seems to be suitable for Virgo application, where wideband and low noise control of the laser beam jitters is required.

From the scenario explored in Chapter 2, it appears that all the efforts for the development of AO technology have been focused to implement performing actuators and processing units, while no attention has been paid to the wavefront sensor, because the standard Shack Hartmann system is commonly accepted as the best solution. On the contrary, we have previously said that the usual Shack Hartmann technique is quite unlikely to be used in the field of GW interferometric antennas because low sensitivity and band limitations are difficult to overcome. For example, even considering a reasonable upgrade of the state of the art, the Shack Hartmann sensor used for the measurement of wavefront global tilt has a residual noise in the region of the tens of Hz of the order of $10^{-8} \text{ rad}/\sqrt{Hz}$ [76], which corresponds to the same order of magnitude of the jitters measured in a free laser operating in quiet laboratory conditions [53].

Starting from this considerations, we have developed an Adaptive Optics system where the phase front detection is performed using an interferometric technique alternative to the Shack Hartmann method. Our Project consists in the design of the system, the implementation of an experimental prototype and the characterization of it in order to validate the theoretical model and to

demonstrate the effectiveness of the AO control in compliance to Virgo requirements [91], [92], [93].

In this Chapter, we present the design of the interferometric AO system based on the Michelson configuration.

A small section is devoted to recall the basic concepts of Gaussian Optics, from the laser beam properties to the laws of propagation in air.

After that, starting from the supposition that small jitters can be described as perturbations of the fundamental Gaussian mode, we demonstrate a correspondence between the higher order Hermite Gauss modes and the Zernike polynomials that expand the phase profile. That is, a laser beam affected by jitters can also be interpreted as a light wave with aberrated wavefront. This allows to design an AO system which measures the laser beam perturbations in terms of higher order Hermite Gauss modes and calculates the commands for wavefront correction in terms of Zernike polynomials.

We present the optical design of the proposed AO system and in particular the interferometric technique for wavefront detection. This technique is based on the interference of the two beams of the Michelson locked on the middle fringe working point. The intensity at the output of the interferometer is read by a pixellated photodiode which produces a set of photocurrents that are proportional to the phase difference of the two beams in a specific portion of wave front area. These photocurrents are amplified and linearly combined so that they provide signals corresponding to coefficients of the Hermite Gauss modes that perturb the laser beam. These coefficients are used as error signals and fed back to the AO control for the generation of the correction commands supplied to the deformable mirror.

We also present the design of the feedback control system operating on six degrees of freedom and in particular the scheme of the block diagram where the regulator and the controlled system are highlighted, as well as the manipulated and the controlled variables. In particular, we present the technique for the extraction of the error signals from the controlled system and the diagonalization of the transfer matrix for the simultaneous control of six modes of aberration.

3.1 Gaussian Optics and higher order Hermite Gauss modes

The electric and magnetic field of a laser beam of wavelength λ is given by the solution of the Helmotz scalar wave equation [94]:

$$\nabla^2 u + k^2 u = 0 \quad (3.1)$$

where $k=2\pi/\lambda$.

This equation is usually solved in free space to obtain the simple solutions of plane and spherical waves.

In Cartesian coordinates, being x and y the transverse axes and z the longitudinal direction of propagation, if we suppose a solution like:

$$u = \Psi(x, y, z)e^{-jkz} \quad (3.2)$$

and assume that the variation of Ψ with z is small compared to the dependence on x and y , we can write:

$$\frac{\partial^2 \Psi}{\partial x^2} + \frac{\partial^2 \Psi}{\partial y^2} - 2jk \frac{\partial \Psi}{\partial z} = 0 \quad (3.3)$$

where we have neglected the term $\frac{\partial^2 \Psi}{\partial z^2}$.

This is the paraxial approximation which can be correctly used in the case of a Gaussian beam, because it has a finite transverse size (few millimetres) and a privileged direction of propagation with small divergence ($\theta \leq 0.5 \text{ rad}$).

The solution of eq. (3.3) has the form:

$$\Psi_{00}(r, z) = A(z)e^{\left[\frac{-jkr^2}{2q(z)}\right]} \quad (3.4)$$

where we have used the radial coordinate $r = (x^2 + y^2)^{1/2}$.

The function Ψ_{00} , which represents the spatial distribution of the EM wave, exhibits a transverse Gaussian profile with respect to the distance r from the axis. It is also worth noting that this expression is formally identical to the solution of the spherical wave, where the radius of curvature is replaced by the complex Gaussian parameter $q(z)$, which is calculated reintroducing eq.

(3.4) into (3.3). In particular, if we fix the origin of the axis z_0 where the Gaussian beam has its minimum transverse size of radius w_0 , named *spot* or *beam waist*, the following relations hold:

$$q = q_0 + z = j \frac{\pi w_0^2}{\lambda} + z \quad (3.5)$$

and

$$\frac{1}{q} = \frac{1}{R(z)} - j \frac{\lambda}{\pi w^2(z)} \quad (3.6)$$

We have here introduced the beam radius $w(z)$ and the radius of curvature $R(z)$ which depend on the longitudinal coordinate z as:

$$w(z) = w_0 \left[1 + \left(\frac{z}{z_R} \right)^2 \right]^{1/2} ; \quad R(z) = z \left[1 + \left(\frac{z_R}{z} \right)^2 \right] \quad (3.7)$$

The term $z_R = \frac{\pi w_0^2}{\lambda}$ is usually referred to as *Rayleigh range* and it corresponds to the distance from the beam waist at which the spot size increases by a factor $\sqrt{2}$ from its initial value.

The complex term $A(z)$ is also calculated as $A(z) = A(0) \frac{w_0}{w(z)} e^{j\phi_0}$, being $A(0)$

and $e^{j\phi_0}$ the initial amplitude and phase respectively. The term ϕ_0 is a phase shift difference between the laser mode and the ideal plane wave.

We can finally rewritten the wave solution of eq. (3.2) as:

$$u(r, z) = \Psi_{00} e^{-jkz} = A(0) \frac{w_0}{w(z)} e^{j \left[\phi_0 - \frac{kr^2}{2R(z)} \right]} e^{-\frac{r^2}{w^2(z)}} e^{-jkz} \quad (3.8)$$

In order to normalize this expression, so that $\int |u|^2 2\pi r dr = |A|^2$, we obtain:

$$u(r, z) = A \sqrt{\frac{2}{\pi w^2(z)}} e^{j \left[\phi_0 - \frac{kr^2}{2R(z)} \right]} e^{-\frac{r^2}{w^2(z)}} e^{-jkz} \quad (3.9)$$

where we have redefined $A(0)=A$.

We can now understand the physical meaning of the introduced parameters. In fact, we see that $R(z)$ is the radius of curvature of the wavefront and that $w(z)$ is the beam radius, or the distance from the axis where the transverse Gaussian profile of the beam is $1/e$ reduced from the peak. The beam radius represents the spot size of the Gaussian beam.

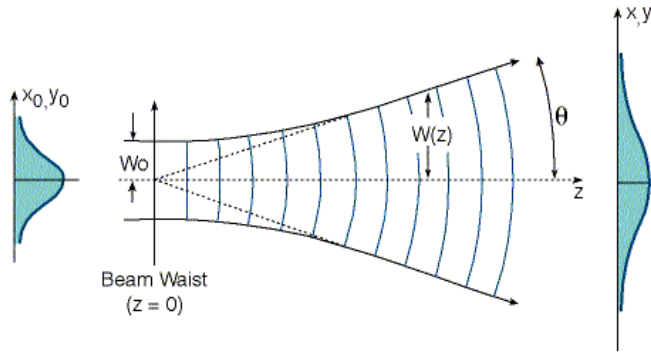


Figure 3.1: propagation of the Gaussian beam. The beam has its origin in the beam waist w_0 and propagates with asymptotic divergence $\theta = \lambda/\pi w_0$.

It is worth noting that in the Gaussian beam the waist $w(z)/w_0$ increases

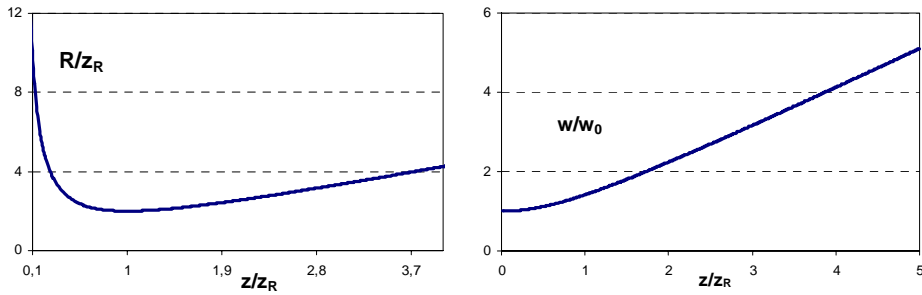


Figure 3.2: radius of curvature R/z_R and beam radius w/w_0 against the coordinate z normalized to the Rayleigh range z_R

while the radius of curvature $R(z)$, initially infinite in the origin, has a minimum in $z=z_R$ (figure 3.2) and then tends again to infinite at large distance, where the wavefront is plane and the beam has a far field diffraction angle given by:

$$\theta = \frac{\lambda}{\pi w_0} \quad (3.10)$$

The intensity distribution of the Gaussian beam is:

$$I(r) = I_0 e^{-\frac{2r^2}{w^2(z)}} \quad (3.11)$$

and drops to $1/e^2$ times its initial value at a distance w_0 from the axis.

The Gaussian mode is only one of the infinite solutions of the Helmotz equation in a laser cavity. There are other similar functions that solve eq. (3.3) and form a complete and orthogonal set of modes of propagation. Therefore, every arbitrary distribution of monochromatic light can be expanded in terms of these modes.

It is demonstrated [94] that these solutions are equal to:

$$\Psi_{nm}(x, y, z) = \Psi_{00}(x, y, z) H_n \left(\sqrt{2} \frac{x}{w(z)} \right) H_m \left(\sqrt{2} \frac{y}{w(z)} \right) e^{j(m+n)\phi_0} \quad (3.12)$$

where H_n and H_m are respectively the Hermite polynomials of order n and m , and an additional phase shift difference proportional to $m+n$ is introduced into the Gaussian mode Ψ_{00} . These are called Hermite Gauss modes and correspond to the Gaussian mode when $n=m=0$.

It is worth noting that the parameters $w(z)$ and $R(z)$ are the same for all modes. This means that they have the same transverse amplitude scaling and the same phase front curvature along the axis.

A generic laser beam can be represented as a superposition of Hermite Gauss modes through coefficients c_{nm} :

$$\Psi(x, y, z) = \sum_{n,m=0}^{\infty} c_{nm} \Psi_{nm}(x, y, z) \quad (3.13)$$

where usually the coefficient c_{00} of the Gaussian mode is extremely large compared with the coefficients c_{nm} of the higher order polynomials.

3.2 Wavefront analysis of the perturbed Gaussian beam: correspondence between Hermite Gauss modes and Zernike polynomials

Let us consider a generic laser beam perturbed in the waist position by defocus and astigmatism [59]. If x' and y' are the two principal astigmatic axes rotated by the angle $\bar{\theta}$ (see figure 3.3),

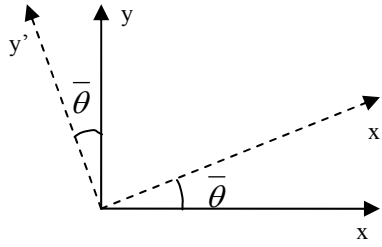


Figure 3.3: principal axes of astigmatism rotated by the angle $\bar{\theta}$

the following change of coordinates holds:

$$\begin{aligned} x' &= x \cos \bar{\theta} + y \sin \bar{\theta} \\ y' &= x \sin \bar{\theta} - y \cos \bar{\theta} \end{aligned} \quad (3.14)$$

These two axes correspond to the maximum and minimum curvature radii $R_{x'}$ and $R_{y'}$. Hence, from eq. (3.9) we can rewrite the perturbed wave function $\Psi(x', y')$ as:

$$\Psi(x', y') = \frac{A}{w_0} \sqrt{\frac{2}{\pi}} \exp \left[-\frac{x'^2 + y'^2}{w_0^2} - j \frac{\pi w_0^2}{\lambda R_{x'}} \frac{x'^2}{w_0^2} - j \frac{\pi w_0^2}{\lambda R_{y'}} \frac{y'^2}{w_0^2} \right] \quad (3.15)$$

Now we define the mean radius expressing the defocus:

$$\frac{1}{R} = \frac{1}{2} \left(\frac{1}{R_{x'}} + \frac{1}{R_{y'}} \right) \quad (3.16)$$

and the astigmatic factor [59]:

$$\delta \left(\frac{1}{R} \right) = \frac{1}{2} \left(\frac{1}{R_{x'}} - \frac{1}{R_{y'}} \right) \quad (3.17)$$

and therefore the following relations apply:

$$\frac{1}{R_{x'}} = \frac{1}{R} + \delta \left(\frac{1}{R} \right) \quad (3.18)$$

and

$$\frac{1}{R_{y'}} = \frac{1}{R} - \delta \left(\frac{1}{R} \right) \quad (3.19)$$

By substituting (3.18) and (3.19) into eq. (3.15), the expression of the perturbed field changes as:

$$\Psi(x', y') = \frac{A}{w_0} \sqrt{\frac{2}{\pi}} \exp \left[-\frac{x'^2 + y'^2}{w_0^2} - j \frac{\pi w_0^2}{\lambda} \left(\frac{1}{R} + \delta \left(\frac{1}{R} \right) \right) \frac{x'^2}{w_0^2} - j \frac{\pi w_0^2}{\lambda} \left(\frac{1}{R} - \delta \left(\frac{1}{R} \right) \right) \frac{y'^2}{w_0^2} \right] \quad (3.20)$$

and then:

$$\Psi(x', y') = \frac{A}{w_0} \sqrt{\frac{2}{\pi}} \exp \left[-\frac{x'^2 + y'^2}{w_0^2} - j \frac{\pi w_0^2}{\lambda R} \left(\frac{x'^2 + y'^2}{w_0^2} \right) - j \frac{\pi w_0^2}{\lambda} \delta \left(\frac{1}{R} \right) \left(\frac{x'^2 - y'^2}{w_0^2} \right) \right] \quad (3.21)$$

By using the fact that:

$$\begin{cases} x'^2 + y'^2 = x^2 + y^2 \\ x'^2 - y'^2 = (x^2 - y^2)(\cos^2 \bar{\theta} - \sin^2 \bar{\theta}) + 4xy \cos \bar{\theta} \sin \bar{\theta} \end{cases} \quad (3.22)$$

we can write:

$$\begin{aligned} \Psi(x, y) = & \frac{A}{w_0} \sqrt{\frac{2}{\pi}} \exp \left[-\frac{x^2 + y^2}{w_0^2} - j \frac{\pi w_0^2}{\lambda R} \left(\frac{x^2 + y^2}{w_0^2} \right) + \right. \\ & \left. - j \frac{\pi w_0^2}{\lambda} \delta \left(\frac{1}{R} \right) \left(\frac{x^2 - y^2}{w_0^2} \right) (\cos^2 \bar{\theta} - \sin^2 \bar{\theta}) - j \frac{\pi w_0^2}{\lambda} \delta \left(\frac{1}{R} \right) \frac{4xy}{w_0^2} \sin \bar{\theta} \cos \bar{\theta} \right] \end{aligned} \quad (3.23)$$

and therefore:

$$\begin{aligned} \Psi(x, y) = & \frac{A}{w_0} \sqrt{\frac{2}{\pi}} \exp \left[-\frac{x^2 + y^2}{w_0^2} - j \frac{\pi w_0^2}{2\lambda R} \left(2 \frac{x^2 + y^2}{w_0^2} - 1 \right) - j \frac{\pi w_0^2}{2\lambda R} + \right. \\ & \left. - j \frac{\pi w_0^2}{\lambda} \delta \left(\frac{1}{R} \right) \left(\frac{x^2 - y^2}{w_0^2} \right) \cos 2\bar{\theta} - j \frac{\pi w_0^2}{\lambda} \delta \left(\frac{1}{R} \right) \frac{2xy}{w_0^2} \sin 2\bar{\theta} \right] \end{aligned} \quad (3.24)$$

In this last equation we have used the well known trigonometric formulas:

$$\begin{cases} \cos^2 \bar{\theta} - \sin^2 \bar{\theta} = \cos 2\bar{\theta} \\ 2 \sin \bar{\theta} \cos \bar{\theta} = \sin 2\bar{\theta} \end{cases} \quad (3.25)$$

If we expand the exponential to first order, eq. (3.24) changes to:

$$\Psi(x, y) \approx \frac{A}{w_0} \sqrt{\frac{2}{\pi}} e^{-\left(\frac{x^2+y^2}{w_0^2}\right)} \left[1 - j \frac{\pi w_0^2}{2\lambda R} - j \frac{\pi w_0^2}{2\lambda R} \left(2 \frac{x^2+y^2}{w_0^2} - 1 \right) + \right. \\ \left. - j \frac{\pi w_0^2}{\lambda} \delta\left(\frac{1}{R}\right) \left(\frac{x^2-y^2}{w_0^2} \right) \cos 2\bar{\theta} - j \frac{\pi w_0^2}{\lambda} \delta\left(\frac{1}{R}\right) \frac{2xy}{w_0^2} \sin 2\bar{\theta} \right] \quad (3.26)$$

and using the expression of the Hermite Gauss modes Ψ_{mn} [94], [95], we can finally write the field as a perturbation to the second order of the fundamental mode:

$$\Psi(x, y) \approx A \left[\left(1 - j \frac{\pi w_0^2}{2\lambda R} \right) \Psi_{00} - j \frac{\pi w_0^2}{2\lambda R} \frac{1}{\sqrt{2}} (\Psi_{20} + \Psi_{02}) + \right. \\ \left. - j \frac{\pi w_0^2}{\lambda} \delta\left(\frac{1}{R}\right) \cos 2\bar{\theta} \frac{1}{\sqrt{2}} (\Psi_{20} - \Psi_{02}) - j \frac{\pi w_0^2}{\lambda} \delta\left(\frac{1}{R}\right) \sin 2\bar{\theta} \cdot \Psi_{11} \right] \quad (3.27)$$

On the other hand, using the coordinates $\rho^2 = (x^2+y^2)/w_0^2$ and $\theta = \tan^{-1} y/x$, from eq. (3.24) we can extract the imaginary part of the field Ψ which represents the phase front function Φ :

$$\Phi(\rho, \theta) \approx \frac{\pi w_0^2}{2\lambda R} + \frac{\pi w_0^2}{2\lambda R} (2\rho^2 - 1) + \frac{\pi w_0^2}{\lambda} \delta\left(\frac{1}{R}\right) \cos 2\bar{\theta} \rho^2 \cos 2\theta + \\ + \frac{\pi w_0^2}{\lambda} \delta\left(\frac{1}{R}\right) \sin 2\bar{\theta} \rho^2 \sin 2\theta \quad (3.28)$$

Using the definitions of real Zernike polynomials Z_n^m and formally restricting the analysis on the circle of radius equal to the beam waist, the wavefront can be rewritten as:

$$\Phi(\rho, \theta) \approx \frac{\pi w_0^2}{2\lambda R} Z_0^0 + \frac{\pi w_0^2}{2\lambda R} Z_2^0 + \frac{\pi w_0^2}{\lambda} \delta\left(\frac{1}{R}\right) \cos 2\bar{\theta} Z_2^2 + \frac{\pi w_0^2}{\lambda} \delta\left(\frac{1}{R}\right) \sin 2\bar{\theta} Z_2^{-2}$$

(3.29)

From eqs. (3.27) and (3.29) we see that, if the wavefront is analysed on the waist surface, there is a direct correspondence between Hermite-Gauss modes of the perturbed beam and wavefront Zernike polynomials. This allows for an easy evaluation of the higher-order Hermite-Gauss modes by the scalar product of the wavefront with the corresponding Zernike mode. For example, the coefficient of the mode $\frac{1}{\sqrt{2}}(\Psi_{20} + \Psi_{02})$ is $\frac{\pi w_0^2}{2\lambda R}$ and corresponds to the coefficient of the Zernike polynomial Z_2^0 representing defocus. The coefficient of the mode $\frac{1}{\sqrt{2}}(\Psi_{20} - \Psi_{02})$ is $\frac{\pi w_0^2}{\lambda} \delta\left(\frac{1}{R}\right) \cos 2\bar{\theta}$ and corresponds to the coefficient of the Zernike polynomial Z_2^2 representing astigmatism 90. The coefficient of the mode Ψ_{11} is $\frac{\pi w_0^2}{\lambda} \delta\left(\frac{1}{R}\right) \sin 2\bar{\theta}$ and corresponds to the coefficient of the Zernike polynomial Z_2^{-2} representing astigmatism 45. Consequently, a closed loop control system can be made generating driving commands for the deformable mirror in terms of Zernike polynomials while the estimate of efficiency of the feedback can be done directly in terms of Hermite-Gauss modes. The present analysis is carried out for Hermite-Gauss modes up to the second order which fulfils the requirements for noise reduction in gravitational wave interferometers.

3.3 Optical design of the interferometric AO system

The AO system that we propose for Virgo application is based on the Michelson interferometric scheme as shown in figure 3.4. The input laser is introduced into the interferometer and its fluctuations are detected in terms of Hermite Gauss coefficients by the measurement of the interference produced on the 5x5 pixellated photodiode placed at the output of the interferometer. In our model one of the two beams of the Michelson is the unperturbed reference and the other is the aberrated beam that we want to correct.

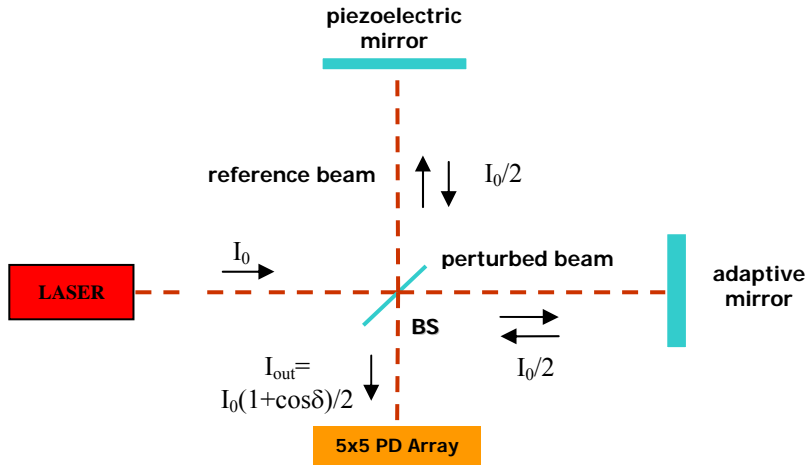


Figure 3.4: scheme of the AO system in the typical Michelson interferometric configuration

The variation of the output intensity I_{out} in the Michelson is [58]:

$$I_{out} = \frac{I_0}{2}(1 + \cos \delta) \quad (3.30)$$

where the average phase difference δ of the two beams is given by $\delta = \frac{4\pi}{\lambda}(L_1 - L_2)$, being L_1 and L_2 the length of the first and the second arm respectively.

Using a piezoelectric mirror in the arm of the reference beam, the interferometer is locked on the middle fringe working point in order to fix the

average phase difference to $\delta = \pi/2$. In this position the output intensity curve has its maximum slope as the derivative:

$$\frac{dI_{out}}{d\delta} = -\frac{I_0}{2} \sin \delta \quad (3.31)$$

reaches its minimum $-I_0/2$ and then provides high sensitivity phase detection, as shown in figure 3.5.

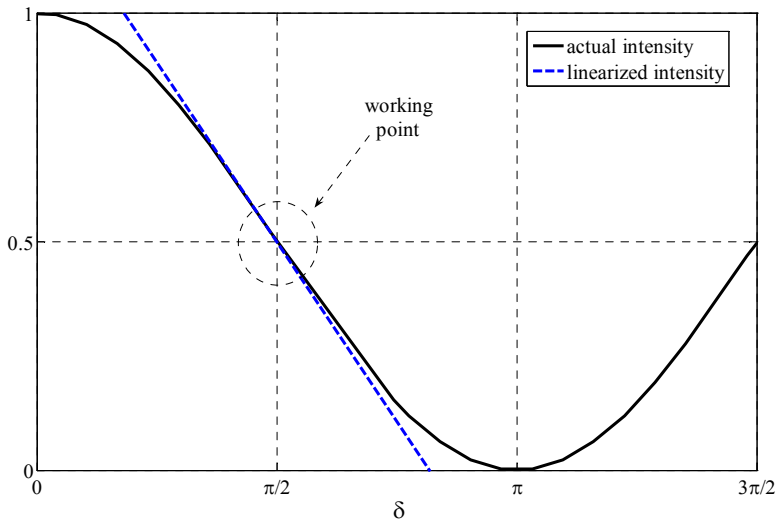


Figure 3.5: normalized output intensity plotted versus the phase difference δ . The actual signal is I_{out}/I_0 (black continuous line) and the linearized signal is I_{out}^{lin}/I_0 (blue dashed line). The interferometer is locked on the working point corresponding to $\delta = \pi/2$.

Furthermore, for small phase variations it is possible to approximate the actual output I_{out} with a linearized function I_{out}^{lin} , given by the expansion to first order of the Taylor series:

$$I_{out}(\delta) \approx I_{out}^{lin}(\delta) = I_{out}\left(\frac{\pi}{2}\right) + \left.\frac{dI_{out}}{d\delta}\right|_{\frac{\pi}{2}} \cdot \left(\delta - \frac{\pi}{2}\right) \quad (3.32)$$

In this optical scheme the typically small laser perturbations do not introduce 2π ambiguities in the wavefront and the intensity signal on each pixel of the photodiodes array is directly proportional to the phase difference of the

beams in that wavefront area. This corresponds to a linear response of the system and allows to describe the automatic control through a linear dynamical model.

The reconstruction of the wavefront profile, or more precisely of the phase difference of the two beams, could be made directly by a point-to-point measurement of the intensity from the 25 photodiodes of the array. But in this case one should achieve the error signals by the scalar product of the measured wavefront function times the Zernike polynomials and therefore this method, even if more sensitive, would not solve the bandwidth limitation exhibited by AO systems based on the Shack Hartmann sensor.

Conversely, we have chosen a more elegant and faster modal feed backing where the 25 signals are projected on the first and second order Hermite Gauss modes and, thanks to the analysis previously carried out, directly used as error signals for the generation of commands in terms of Zernike modes.

The Hermite Gauss coefficients are calculated by suitable linear combinations of the 25 intensity signals coming from the photodiodes array, according to the description detailed in Section 3.5.

For the moment, we remark the difference that stands between the classic AO system and our AO control based on interferometric techniques. With reference to Subsection 2.3.1, the classical AO scheme needs at least five different steps for the wavefront correction, that are:

1. image acquisition by CCD
2. centroide calculation
3. wavefront reconstruction by numerical integration of measured derivatives
4. scalar products of wave aberration function and Zernike polynomials for the calculation of aberration coefficients to use as error signals
5. error signals process and generation of commands for the deformable mirror

The ensemble of all these operations, even if at the best of the present technology, limits the control bandwidth below few tens of *Hz*.

Instead, in our scheme the 25 intensity signals are directly transformed into Hermite Gauss coefficients of first and second order. This means that in only one step we obtain the same result that is obtained in four steps using the classical Shack Hartmann sensor. This allows a considerable increase of the speed of the system.

3.4 Design of the feedback control system

We have implemented two different feedback controls: one for the lock in of the interferometer on the middle fringe working point and one more complicated for the automatic correction of the laser beam aberrations.

The design of these two control systems is based on the typical closed loop architecture described by linear dynamical mathematical models [96].

Let us shortly remind that a generic stationary system, with output signal $c(t)$ linearly depending on the input signal $m(t)$, is described by the simple scheme below where the parameter K represents the constant of proportionality between $c(t)$ and $m(t)$.

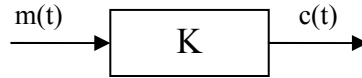


Figure 3.6: scheme of a linear dynamical system.

If K is simply a constant, the system is algebraic. Otherwise, its dynamical behaviour is described by linear differential equations with constant coefficients and the parameter K is replaced by a complex function $K(s)$ called *transfer function* of the system. The transfer function, which converts the Laplace transform of the input signal into the Laplace transform of the output signal, is strictly correlated with the frequency response necessary for the Fourier analysis of the system.

Without loss of generality, let us consider the algebraic case. In the ideal condition, the output of the system should each time obey the following expression:

$$c(t) = Km(t) \quad (3.33)$$

but unfortunately in real cases the system is affected by several perturbations (external disturbances, non linearity effects and variations of K) which cause eq. (3.33) to be modified into:

$$c(t) = Km(t) \pm \Delta c(t) \quad (3.34)$$

The term $\Delta c(t)$ indicates the output fluctuations induced by the system perturbations.

In order to reduce such fluctuations $\Delta c(t)$, we can use a feedback control system of the type schematized in figure 3.7.

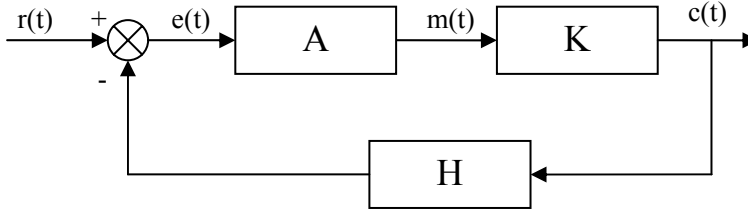


Figure 3.7: block diagram of a feedback control system

The output controlled signal $c(t)$ is fed back to the input by the transducer H which converts it into a form that is comparable with reference $r(t)$. The difference of $r(t)$ with the feedback gives the error signal $e(t)$, which is introduced into the cascade of amplifier and actuator represented by A . The output of A drives the manipulable variable $m(t)$ in order to fix $c(t)$ at the desired value.

This closed loop configuration allows to reduce the output fluctuations. In fact, the system is now described by the equations:

$$\begin{cases} c(t) = Ge(t) \pm \Delta c(t) \\ e(t) = r(t) - Hc(t) \end{cases} \quad (3.35)$$

from which we obtain:

$$c(t) = \frac{G}{1 + GH} r(t) \pm \frac{\Delta c(t)}{1 + GH} \quad (3.36)$$

being $G=AK$.

The parameter GH is named *open loop gain* and it determines robustness and efficiency of the system in lowering the output signal fluctuations $\Delta c(t)$ in the stationary state. In fact, if we assume that $GH \gg 1$, eq. (3.36) at regime state reduces to:

$$c(t) \approx \frac{1}{H} r(t) \pm \frac{\Delta c(t)}{GH} \quad (3.37)$$

where the output $c(t)$ is proportional to the reference signal $r(t)$ and the residual noise is strongly decreased, as $\frac{\Delta c(t)}{GH} \ll \Delta c(t)$.

It is worth noting that high values of the open loop gain have a negative impact on the transient behaviour of the system, as the correction operated by the feedback often induces unpleasant oscillations before the new stationary state is reached. If the gain is very high, it is possible that the system oscillates indefinitely and exhibits an unstable behaviour. In order to correct this effect it is common to provide into the loop a correcting network that both improves the system dynamical behaviour and keeps save the high level of static gain, or the value of GH at low frequency.

The general scheme of an efficient and stable feedback control system can be represented as in figure 3.8, where we can distinguish three principal blocks, or the Controlled System, the Transducer and the Regulator.

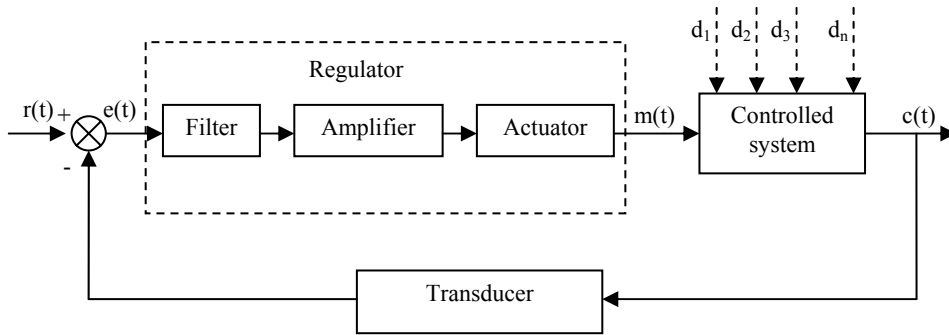


Figure 3.8: block diagram of a stabilized feedback control system

The Controlled System is characterized by the output $c(t)$ which is the variable that we want to control against the disturbances d_1, \dots, d_n by manipulating the variable $m(t)$.

The Transducer converts the output $c(t)$ and feeds it back into the comparator where it is subtracted from the reference signal $r(t)$.

The Regulator receives the error signal $e(t)$ and, after filtering for stability, amplifies and sends driver commands to the actuator for $m(t)$ manipulation.

The target of the closed loop control system is to maintain each time the controlled variable $c(t)$ proportional to the reference signal $r(t)$.

3.4.1 Control system for the interferometer *lock in*

The first feedback control has been designed to lock the interferometer on the half fringe working point.

We start from the definition of the controlled variable that is the total sum of the 25 optical intensities emerging in form of photocurrents from the 5x5 array of photodiodes.

Provided that these 25 photocurrents are amplified and converted into 25 voltage signals V_i (in the next Chapter we present the experimental set up in detail), we have added all these signals in order to obtain the total voltage:

$$V_{tot} = \sum_{i=1}^{25} V_i \quad (3.38)$$

which is exactly our controlled variable.

The actuator is a flat piezoelectric mirror placed in one of the two arms of the interferometer, as pictured in figure 3.4. It is driven by a voltage amplifier and moves longitudinally along the optical axis, lengthening or shortening the interferometer arm of length L_1 . So the optical path difference $\Delta L = L_1 - L_2$ (L_1 and L_2 are the length of the first and the second arm of the Michelson) is changed and this induces the variation of the average phase difference δ of the two beams, given by:

$$\delta(t) = \frac{4\pi}{\lambda} (L_1 - L_2) \quad (3.39)$$

This is the manipulable variable of the controlled system.

We have first calibrated the interferometer by measuring the two output voltage levels V_{max} and V_{min} corresponding respectively to maximum and minimum of the interference curve of eq. (3.30); secondly, we have calculated their medium value and used it as reference set point $V_r = (V_{max} + V_{min})/2$ that must be supplied to the piezoelectric mirror for the interferometer locking on the middle fringe working point of figure 3.5.

The error signal e , corresponding each time to the difference $V_r - V_{tot}$, is sent to the correcting filter and then to the amplifier of the piezo which is automatically moved back or forth in order to correct the small phase fluctuations and keep the interferometer on the working point. In our scheme the reference V_r and the output V_{tot} are both voltage signals and then the transducer is simply a connection between the output and the comparator.

Figure 3.9 shows the block diagram of the system with clearly identified the regulator, the controlled system, the transducer and the relative variables.

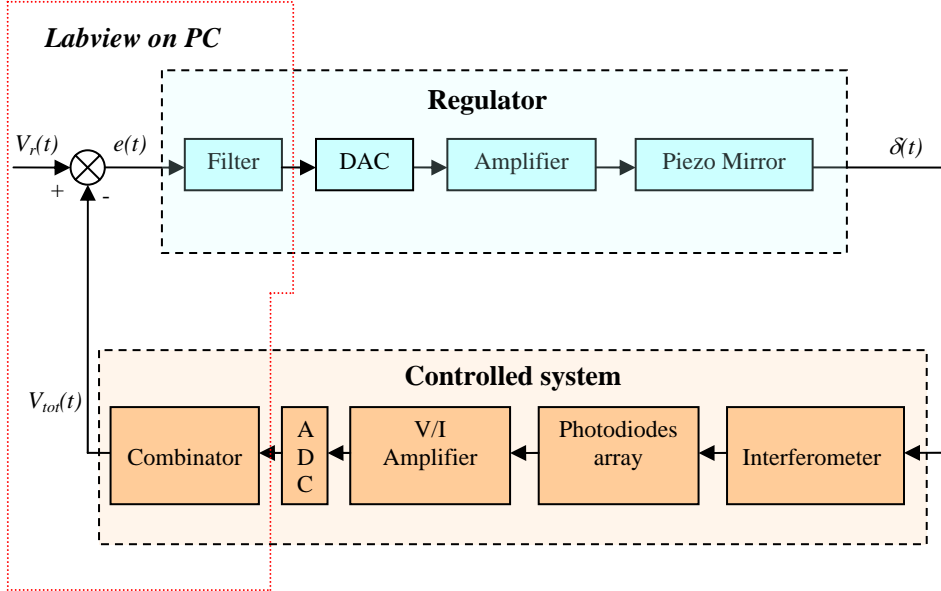


Figure 3.9: block diagram of the feedback control system for the lock in of the interferometer. The phase difference $\delta(t)$ between the two beams of the interferometer is the manipulable variable, the total voltage $V_{tot}(t)$ corresponding to the sum of the 25 intensities collected by the pixellated photodiode is the controlled variable. The piezoelectric mirror manipulates $\delta(t)$ by changing the optical path length of one arm. The data processing from the output of the Analogical Digital Converter (ADC) to the input of the Digital Analogical Converter (DAC) is performed by a Labview Virtual Instrument running on a standard PC.

In particular, we remark that the 25 voltage signals emerging from the photodiode amplifiers are first converted into digital form by an ADC board and then added to form the total voltage V_{tot} . Similarly, the driver signal emerging from the filter is converted into analogical form by a DAC board before entering the piezoelectric amplifier. All the operations of data processing from the output of the ADC to the input of the DAC are implemented by a Labview Virtual Instrument running on PC.

The control system dynamics is well described by the following equation:

$$V_{tot} = \frac{G}{1+G} V_r + \frac{1}{1+G} \Delta V_{tot} \quad (3.40)$$

being G the open loop gain of the system.

3.4.2 Control system for the correction of laser beam aberrations

The second feedback control that we have designed is the AO system for the correction of small laser beam fluctuations.

In this case the design is more complicated because we have to control several variables simultaneously. This means that each subsystem of the block diagram that represents the control is characterized by a matrix of transfer functions whose dimension depends on the number of input and output variables. We have designed the control system for the simultaneous correction of 6 modes of aberration that are respectively longitudinal mode, TiltX, TiltY, Astigmatism45, Astigmatism90 and Defocus. This means that we have to deal with 6 degrees of freedom. Furthermore, we have 25 signals emerging from the photodiodes array and 59 channels for the driver of the adaptive mirror. Therefore the different matrices that we have designed can have row and column indices equal to 6, 25 or 59.

The first step for the design of the control system is again the identification of the controlled and the manipulable variables. In this case, by suitably combining the 25 signals of the pixellated photodiode, we expect to achieve 6 voltage signals that linearly depend on the 6 aberration coefficients relative to first and second order Hermite Gauss modes. These voltage signals, which we define as S_i , $i=1,...,6$, form a 6x1 column vector

$$S(t) = \begin{pmatrix} S_1 \\ S_2 \\ S_3 \\ S_4 \\ S_5 \\ S_6 \end{pmatrix} \quad (3.41)$$

and represent the output controlled variables.

The manipulable variables are the six adimensional signals corresponding to longitudinal mode ϕ , TiltX a_x , the TiltY a_y , the Astigmatism45 a_{45} , the Astigmatism90 a_{90} and the Defocus a_D . They represent the geometrical distortion of the ideal wavefront and arranged into a 6x1 column vector M of form:

$$M(t) = \begin{pmatrix} \phi \\ a_x \\ a_y \\ a_{45} \\ a_{90} \\ a_D \end{pmatrix} \quad (3.42)$$

The reference set point R is the 6x1 column vector of voltages R_i , $i=1,...,6$:

$$R(t) = \begin{pmatrix} R_1 \\ R_2 \\ R_3 \\ R_4 \\ R_5 \\ R_6 \end{pmatrix} \quad (3.43)$$

which must be compared with the controlled variable S_i to generate the error signal. For the purpose of jitters suppression the reference signal is set to zero except for the first component ($R_1=V_r$, $R_i=0 \ \forall i=2,...,6$) that is fixed at the middle fringe value when the piezo is switched off. It is worth noting that by suitably changing the set point components R_i it is possible to manipulate the laser wavefront and generate artificial profiles that could be adopted for specific applications like sensing systems or industrial processes. This perspective is interesting upgrade of our system, but at the moment goes beyond the scope of the present work.

The architecture of control system is schematized in the block diagram of figure 3.10 where we recognize the three main blocks corresponding to Controlled system, Transducer and Regulator.

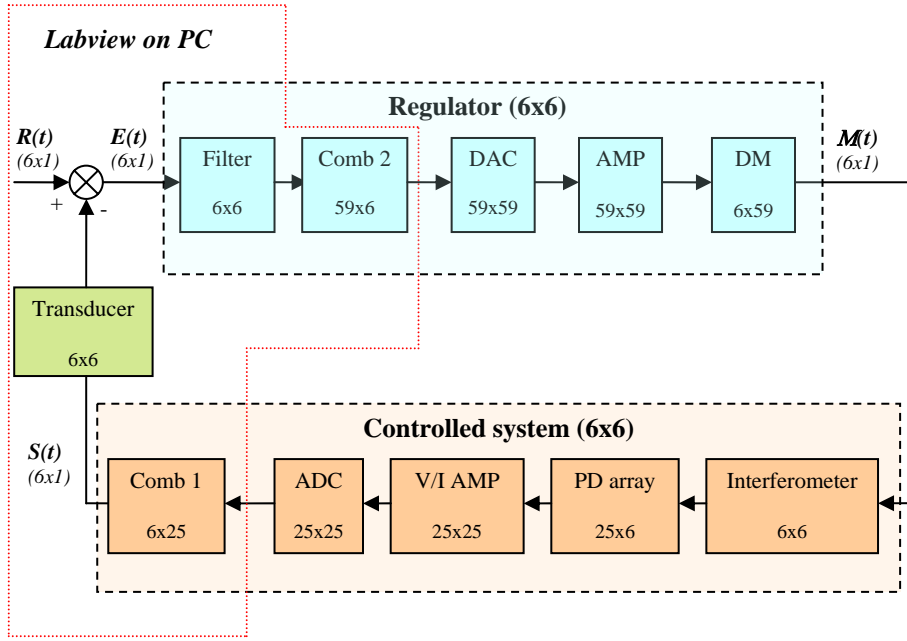


Figure 3.10: block diagram of the Adaptive Optics feedback control system for the laser beam correction. The aberration vector $M(t)$ is the manipulable variable, the vector $S(t)$ corresponding to 6 different combinations of 25 voltage signals generated by the pixellated photodiode is the controlled variable. The error signal $E(t)$ given by the difference between the reference $R(t)$ and $S(t)$ is converted into a set of 59 driver commands sent to the deformable mirror (DM) which corrects the aberrations by changing the geometrical pattern of its adaptive surface. The data processing from the output of the ADC to the input of the DAC is performed by a Labview Virtual Instrument running on a standard PC.

The Controlled system is constituted by the entire interferometer, the pixellated photodiode, the amplifiers, the ADC board and the Combinator 1. It is described by a 6×6 matrix of transfer functions which converts the 6×1 manipulable vector $M(t)$ of eq. (3.42) into the 6×1 controlled vector $S(t)$ of eq. (3.41). In detail, the 6 geometrical aberration signals are transformed by the interferometer into 6 different interference patterns which in turn are converted into a set of 25 photocurrents by the pixellated photodiode. After that, the amplifiers transform the 25 photocurrents into 25 amplified voltages and the ADC board converts them into digital form. Finally, the Combinator 1 is a 6×25 matrix that collects the 25 voltages and gives out the 6×1 column vector corresponding to the controlled variable S .

The vector S is directly compared with the set point R also expressed in terms of voltage; this means that the Transducer is simply a 6×6 identity matrix.

The error signal $E=R-S$ is sent from the comparator to the Regulator, made of the correcting filter, the Combinator 2, the DAC, the amplifiers and the Deformable Mirror that is the actuator of the system.

The Regulator is described by a 6×6 matrix of transfer functions. In fact, it is entered by the 6×1 vector E which, after passing through the filter is sent to the 59×6 Combinator 2 for the generation of the 59×1 column vector of commands provided to the actuator. The 59 commands are transformed into analogical form by the DAC and amplified for the electrostatic actuators of the deformable mirror. Finally the mirror, described by a 6×59 matrix, converts the 59 amplified voltages into 6 different geometrical profiles of its deformable surface for the manipulation of the vector $M(t)$.

Figure 3.11 represents the synthetic block diagram of the AO system. In the top Regulator and Controlled system have transfer matrices A and K respectively. In the bottom we see only one block representing the open loop system of transfer matrix $G=KA$. The loop is closed by the transducer that is simply a connection between the output and the comparator.

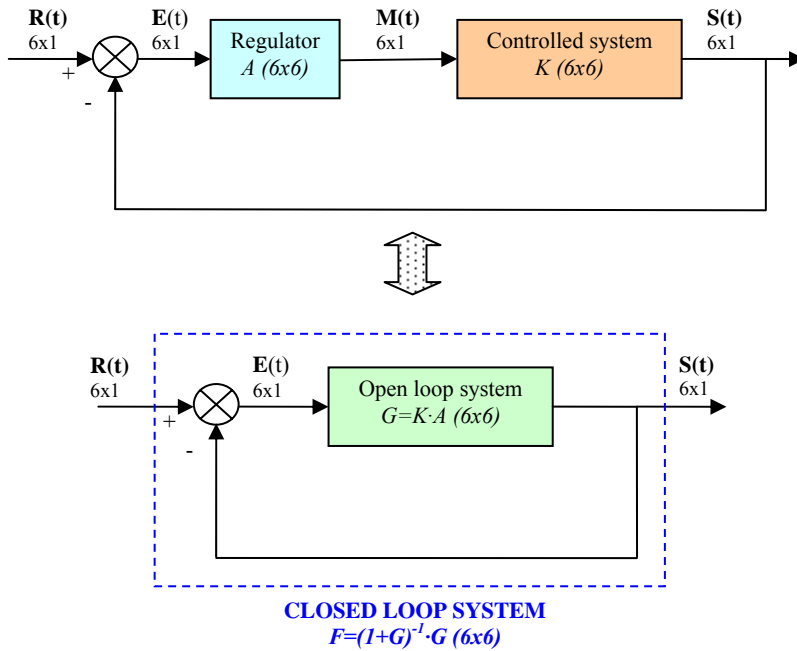


Figure 3.11: synthetic block diagram of the Adaptive Optics control system. The open loop 6×6 transfer matrix is G , the closed loop 6×6 transfer matrix is $F = (I + G)^{-1} \cdot G$.

Using the scheme of figure 3.11 we can analyse the mathematical model that describes the stationary state of the system, based on matrix equations as:

$$\begin{cases} S(t) = K \cdot A \cdot E(t) \pm \Delta S(t) \\ E(t) = R(t) - S(t) \end{cases} \quad (3.44)$$

from which:

$$S(t) = (1 + G)^{-1} \cdot G \cdot R(t) \pm (1 + G)^{-1} \cdot \Delta S(t) \quad (3.45)$$

This last matrix equation describes the dynamical behaviour of the closed loop AO system that we have designed to clean up laser beam jitters into the Michelson interferometer shown in figure 3.4.

Let us observe that the 6x6 matrix G :

$$G = K \cdot A = S \cdot E^{-1} \quad (3.46)$$

is the open loop gain, while the 6x6 matrix F :

$$F = (1 + G)^{-1} \cdot G \quad (3.47)$$

is the transfer function at closed loop.

In the ideal case we would like to have a completely diagonal matrix G because this would mean that the variables are all decoupled one with another.

In the real case G has non null off diagonal elements because there are coupling effects due to the sensing subsystem and to the actuator.

This condition could compromise effectiveness and stability of the control.

Nevertheless, we have arranged methods to suppress the coupling effects and to bring the off diagonal elements to acceptable residual values.

In the next two sections we show the calculation and the diagonalization of the 6x6 transfer matrix K relative to the sensing subsystem and of the 6x6 transfer matrix A of the Regulator.

3.5 Error signals extraction from the Controlled System and diagonalization of the 6x6 transfer matrix K

We have designed the AO system for the simultaneous correction of 6 aberration modes of the laser beam in air. In particular we have shown the block diagram of the feedback control in figure 3.10 and calculated the dynamics in eq. (3.45).

Now we need to investigate the method for the extraction of error signals from the Controlled System. This corresponds to determine the 6x25 transfer matrix of the Combinator 1 that converts the 25 voltages emerging from the amplified photodiodes into 6 voltage signals linearly depending on first and second order Hermite Gauss coefficients (also corresponding to longitudinal translation, TiltX, TiltY, Astigmatism45, Astigmatism90 and Defocus).

Let us consider the two beams of the Michelson interferometer of figure 3.4 and assume that E_1 is the field of the unperturbed beam in the first arm while E_2 is the field of the aberrated beam in the second arm. The field E_1 has $\pi/2$ phase difference with respect to E_2 , due to the interferometer middle fringe lock in, and therefore it can be written as:

$$E_1 = Ae^{j\frac{\pi}{2}}\Psi_{00} = Aj\Psi_{00} \quad (3.48)$$

On the other hand, using the results of Section 3.2, the aberrated field E_2 is given by:

$$E_2 = A \left[(1 + j\phi)\Psi_{00} + a_x\Psi_{10} + a_y\Psi_{01} + a_{45}\Psi_{11} + a_{90}\frac{1}{\sqrt{2}}(\Psi_{20} - \Psi_{02}) + a_D\frac{1}{\sqrt{2}}(\Psi_{20} + \Psi_{02}) \right] \quad (3.49)$$

where ϕ represents the instantaneous longitudinal translation of the two wavefronts and a_i are complex coefficients of the basic aberrations corresponding to perturbations of the fundamental Gaussian mode up to the second order.

The total normalized intensity at the output of the interferometer is given by:

$$I_{out} = \frac{|E_{tot}|^2}{2A^2} + \frac{|E_1 + E_2|^2}{2A^2} = (1 + \phi) |\Psi_{00}|^2 + \overline{a_x} \Psi_{00} \Psi_{10} + \overline{a_y} \Psi_{00} \Psi_{01} + \overline{a_{45}} \Psi_{00} \Psi_{11} +$$

$$\overline{a_{90}} \Psi_{00} \frac{1}{\sqrt{2}} (\Psi_{20} - \Psi_{02}) + \overline{a_D} \Psi_{00} \frac{1}{\sqrt{2}} (\Psi_{20} + \Psi_{02})$$
(3.50)

being $\overline{a_i} = \mathbf{Re} a_i + \mathbf{Im} a_i$ and neglecting terms higher than first order.

Using eq. (3.50) we can now demonstrate that the 25 signals emerging from the photodiodes can be transformed into 6 signals linearly depending on the aberration coefficients ϕ and a_i and therefore they can reintroduced as error signals into the system for the modal control of the laser beam.

Let us consider the 5x5 photodiodes array as schematized in figure 3.12.

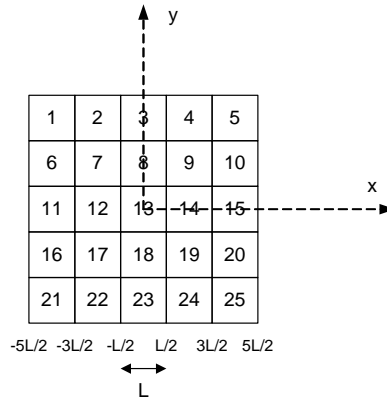


Figure 3.12: 5x5 array of photodiodes collecting the output intensity of the interferometer

Each single photodiode of area $L \times L$ collects only a part $I_{n,m}$ of the total intensity that is:

$$I_{n,m} = \int_{\alpha_x}^{\beta_x} dx \int_{\alpha_y}^{\beta_y} dy I_{out}$$
(3.51)

with:

$$n = -2, -1, 0, 1, 2 \quad ; \quad m = -2, -1, 0, 1, 2$$

and

$$\left\{ \begin{array}{l} \alpha_x = \left(n - \frac{1}{2} \right) L \\ \beta_x = \left(n + \frac{1}{2} \right) L \end{array} \right. ; \left\{ \begin{array}{l} \alpha_y = \left(m - \frac{1}{2} \right) L \\ \beta_y = \left(m + \frac{1}{2} \right) L \end{array} \right. \quad \forall n, m$$

Combining the 25 intensity signals $I_{n,m}$ it is possible to obtain 6 signals S_i linearly corresponding to the aberration coefficients.

In other words, our goal is to characterize the Controlled System through the following matrix equation:

$$\begin{aligned} S &= K \cdot M + H \\ \Downarrow \\ \begin{pmatrix} S_1 \\ S_2 \\ S_3 \\ S_4 \\ S_5 \\ S_6 \end{pmatrix} &= \begin{pmatrix} k_{11} & k_{12} & k_{13} & k_{14} & k_{15} & k_{16} \\ k_{21} & k_{22} & k_{23} & k_{24} & k_{25} & k_{26} \\ k_{31} & k_{32} & k_{33} & k_{34} & k_{35} & k_{36} \\ k_{41} & k_{42} & k_{43} & k_{44} & k_{45} & k_{46} \\ k_{51} & k_{52} & k_{53} & k_{54} & k_{55} & k_{56} \\ k_{61} & k_{62} & k_{63} & k_{64} & k_{65} & k_{66} \end{pmatrix} \cdot \begin{pmatrix} \phi \\ \overline{a_x} \\ \overline{a_y} \\ \overline{a_{45}} \\ \overline{a_{90}} \\ \overline{a_D} \end{pmatrix} + \begin{pmatrix} H_1 \\ H_2 \\ H_3 \\ H_4 \\ H_5 \\ H_6 \end{pmatrix} \end{aligned} \quad (3.52)$$

where k_{ij} are transfer functions for each degree of freedom and H_i are constants related to the geometry of the system.

This result can be achieved using the correspondence of 6 analytical integrals of I_{out} with 6 linear combinations of $I_{n,m}$ as shown below.

In fact, from eq. (3.50) the intensity I_{out} is expressed in terms of Hermite Gauss modes which in turn are even or odd functions in the square domain x, y with $x \in \left(-\frac{5}{2}L, \frac{5}{2}L \right)$ and $y \in \left(-\frac{5}{2}L, \frac{5}{2}L \right)$. So, if we integrate I_{out} over

that domain, changing each time the sign of integration in parts of it, we obtain that the contribution of some Hermite Gauss modes is null and therefore the total integral is only proportional to one of the six aberration coefficients. On the other hand, the integral analytically obtained can be put in correspondence with a specific linear combination of the 25 signals $I_{n,m}$

and thus we find the desired connection between this linear combination and the aberration coefficient.

Let us start from the integral of I_{out} over the whole domain where only the contribution of the even terms $|\Psi_{00}|^2$ and $\Psi_{00}(\Psi_{20} + \Psi_{02})$ is non null.

This is clear if we look at figures 3.13 and 3.14 which report the 3D plot of the two functions.

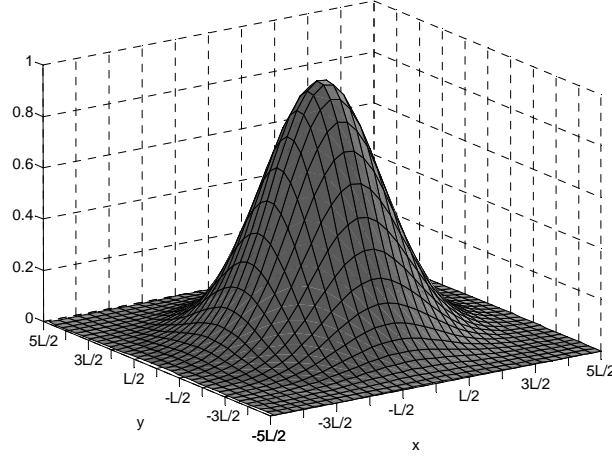


Figure 3.13: profile of $|\Psi_{00}|^2$ in the square domain of the photodiodes array

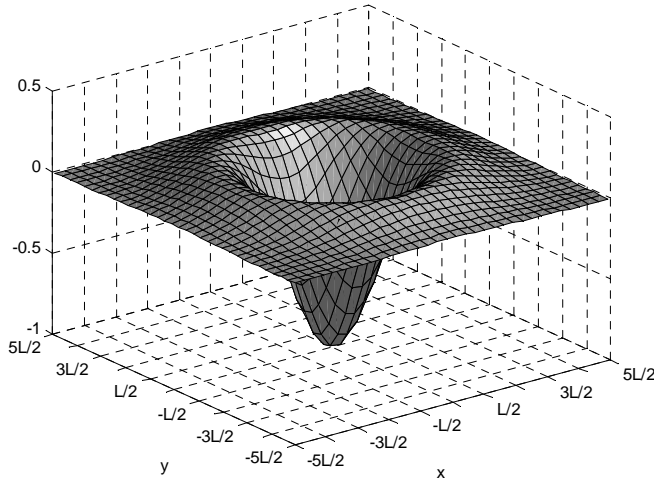


Figure 3.14: profile of $\Psi_{00} \frac{1}{\sqrt{2}}(\Psi_{20} + \Psi_{02})$ in the square domain of the photodiodes array

Hence the integral is:

$$\begin{aligned}
 S_1 = \int_{-\frac{5L}{2}}^{+\frac{5L}{2}} dx \int_{-\frac{5L}{2}}^{+\frac{5L}{2}} dy I_{out} &= (1 + \phi) \int_{-\frac{5L}{2}}^{+\frac{5L}{2}} dx \int_{-\frac{5L}{2}}^{+\frac{5L}{2}} dy |\Psi_{00}|^2 + \\
 &+ \overline{a_D} \int_{-\frac{5L}{2}}^{+\frac{5L}{2}} dx \int_{-\frac{5L}{2}}^{+\frac{5L}{2}} dy \frac{1}{\sqrt{2}} \Psi_{00} (\Psi_{20} + \Psi_{02}) = k_{11}(L, w_0)(1 + \phi) + k_{16}(L, w_0) \overline{a_D}
 \end{aligned}
 \tag{3.53}$$

where k_{11} and k_{16} are non null integrals depending on the length L of the single photodiode and on the beam waist w_0 .

On the other hand, the same result S_I can be achieved by the numerical sum of 25 measured intensities as:

$$S_1 = \sum_{n,m=-2}^{+2} I_{n,m}
 \tag{3.54}$$

Therefore, from eqs. (3.53) and (3.54) we can affirm that the signal produced by the sum of all the 25 intensities is a linear function of the two aberration coefficients ϕ and a_D . This is exactly what we have assumed before and allows to fill the first row of the matrix equation (3.52)

We find similar relationships between other linear combinations of $I_{n,m}$ and other aberration coefficients, playing with the even and odd Hermite Gauss functions.

The integral of I_{out} over the half plane where $x > 0$ less the integral of I_{out} over the half plane where $x < 0$ is null for all the Hermite Gauss functions apart from the term $\Psi_{00} \Psi_{10}$, as can be seen in figure 3.15.

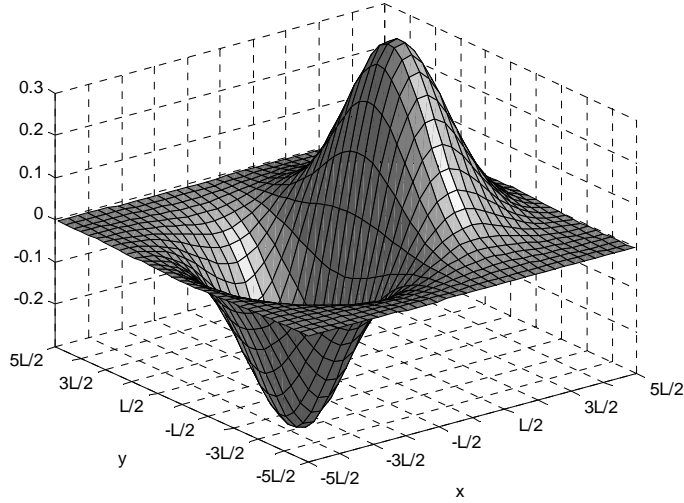


Figure 3.15: profile of $\Psi_{00}\Psi_{10}$ in the square domain of the photodiodes array

Therefore the integral S_2 corresponds to the aberration coefficient a_x :

$$\begin{aligned}
 S_2 &= \int_{-\frac{5L}{2}}^{+\frac{5L}{2}} dy \left[\int_0^{+\frac{5L}{2}} dx I_{out} - \int_{-\frac{5L}{2}}^0 dx I_{out} \right] = \\
 \overline{a_x} \int_{-\frac{5L}{2}}^{+\frac{5L}{2}} dy \left[\int_0^{+\frac{5L}{2}} dx \Psi_{00} \Psi_{10} - \int_{-\frac{5L}{2}}^0 dx \Psi_{00} \Psi_{10} \right] &= k_{22}(L, w_0) \cdot \overline{a_x}
 \end{aligned} \tag{3.55}$$

The same value is given by the numerical sum of the $I_{n,m}$ in the plane $x>0$ less the sum of the $I_{n,m}$ in the plane $x<0$. Referring to figure 3.12, the photodiodes 3, 8, 13, 18, 23 which stand across the y axis belong for their left half part to the plane $x<0$ and for their right half part to the plane $x>0$. Therefore the corresponding intensities are half added and half subtracted and the total contribution is null. This allows to neglect the terms $I_{n,m}$ with $n=0$. Then the signal S_2 is given by:

$$S_2 = \sum_{m=-2, -1, 0, 1, 2}^{n=1, 2} I_{n,m} - \sum_{m=-2, -1, 0, 1, 2}^{n=-2, -1} I_{n,m} \tag{3.56}$$

and we can say that, if we sum all the intensities from the photodiodes on the right side of the array and subtract all the intensities from the photodiodes on

the left side of the array, we have a signal proportional to the TiltX coefficient.

The signal proportional to the TiltY coefficient is obtained with an identical calculation. In fact, the integral of I_{out} over the half plane where $y > 0$ less the integral of I_{out} over the half plane where $y < 0$ is null for all the Hermite Gauss functions apart from the term $\Psi_{00}\Psi_{01}$, as can be seen in figure 3.16.

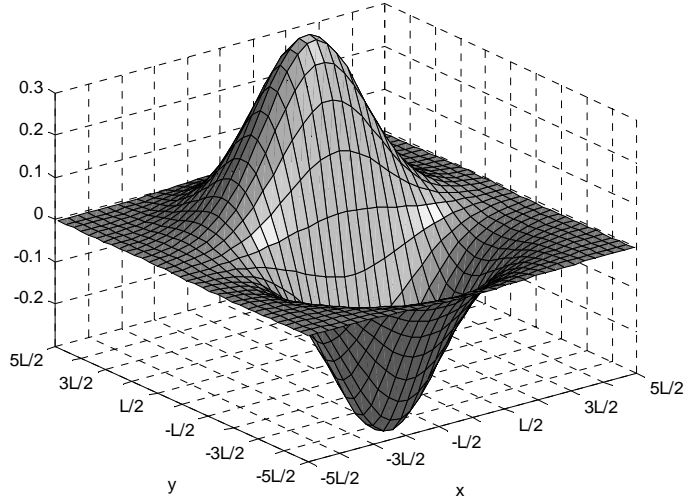


Figure 3.16: profile of $\Psi_{00}\Psi_{01}$ in the square domain of the photodiodes array

Therefore the integral S_3 corresponds to the aberration coefficient a_y :

$$S_3 = \int_{-\frac{5L}{2}}^{+\frac{5L}{2}} dx \left[\int_0^{+\frac{5L}{2}} dy I_{out} - \int_{-\frac{5L}{2}}^0 dy I_{out} \right] = \quad (3.57)$$

$$\overline{a_y} \int_{-\frac{5L}{2}}^{+\frac{5L}{2}} dx \left[\int_0^{+\frac{5L}{2}} dy \Psi_{00}\Psi_{01} - \int_{-\frac{5L}{2}}^0 dy \Psi_{00}\Psi_{01} \right] = k_{33}(L, w_0) \cdot \overline{a_y}$$

and is equal to the sum:

$$S_3 = \sum_{n=-2,-1,0,1,2}^{m=1,2} I_{n,m} - \sum_{n=-2,-1,0,1,2}^{m=-2,-1} I_{n,m} \quad (3.58)$$

Similarly, the integral corresponding to the coefficient of Astigmatism₄₅ is calculated using the symmetry of the function $\Psi_{00}\Psi_{11}$ plotted in figure 3.17.

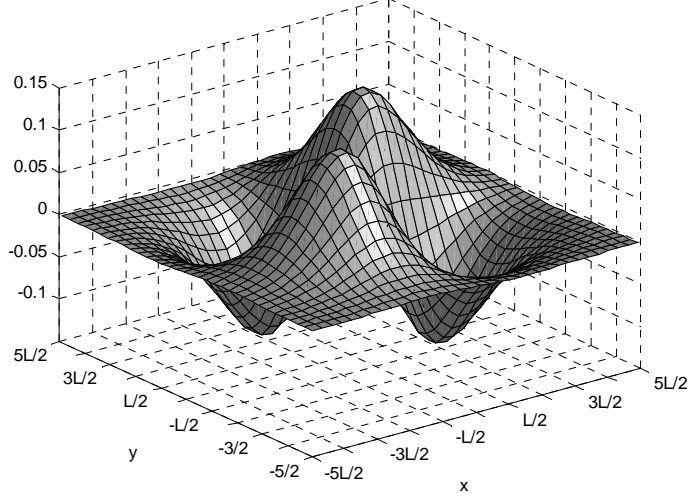


Figure 3.17: profile of $\Psi_{00}\Psi_{11}$ in the square domain of the photodiodes array

If we integrate the intensity I_{out} over first and third quadrant of the square domain and subtract the integrals over second and fourth quadrant, we get a signal proportional to a_{45} :

$$\begin{aligned}
 S_4 = & \int_0^{+\frac{5}{2}L} dx \int_0^{+\frac{5}{2}L} dy I_{out} + \int_{-\frac{5}{2}L}^0 dx \int_{-\frac{5}{2}L}^0 dy I_{out} - \int_0^{+\frac{5}{2}L} dx \int_{-\frac{5}{2}L}^0 dy I_{out} + \\
 & - \int_{-\frac{5}{2}L}^0 dx \int_0^{+\frac{5}{2}L} dy I_{out} = \overline{a_{45}} \cdot 4 \int_0^{+\frac{5}{2}L} dx \int_0^{+\frac{5}{2}L} dy \Psi_{00} \Psi_{11} = k_{44}(L, w_0) \cdot \overline{a_{45}}
 \end{aligned} \tag{3.59}$$

The result is equal to the sum of intensities from photodiodes of the first and third quadrant less the sum of intensities from photodiodes of the second and fourth quadrant..

$$S_4 = \sum_{n=1,2}^{m=1,2} I_{n,m} + \sum_{n=-2,-1}^{m=-2,-1} I_{n,m} - \sum_{n=1,2}^{m=-2,-1} I_{n,m} - \sum_{n=-2,-1}^{m=1,2} I_{n,m} \tag{3.60}$$

The contribution of the photodiodes across the x and y axes, that is $I_{n,m}$ at $n=0$ or $m=0$, is null for considerations analogue to what discussed before

The coefficient of Astigmatism₉₀ is related to the function $\Psi_{00} \frac{1}{\sqrt{2}} (\Psi_{20} - \Psi_{02})$ plotted in figure 3.18.

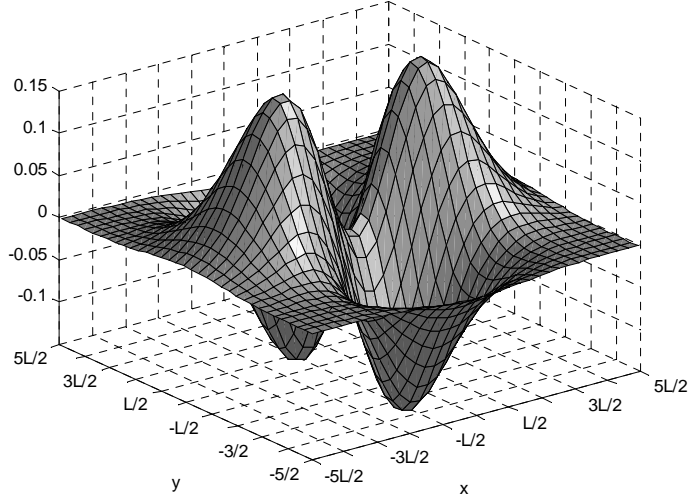


Figure 3.18: profile of $\Psi_{00} \frac{1}{\sqrt{2}} (\Psi_{20} - \Psi_{02})$ in the square domain of the photodiodes array

The integral where we get the coefficient a_{90} is:

$$\begin{aligned}
 S_5 &= \left[\int_{+\frac{3}{2}L}^{+\frac{5}{2}L} dx \int_{-\frac{3}{2}L}^{+\frac{3}{2}L} dy + \int_{-\frac{5}{2}L}^{-\frac{3}{2}L} dx \int_{-\frac{3}{2}L}^{+\frac{3}{2}L} dy - \int_{-\frac{3}{2}L}^{+\frac{3}{2}L} dx \int_{+\frac{3}{2}L}^{+\frac{5}{2}L} dy - \int_{+\frac{3}{2}L}^{+\frac{5}{2}L} dx \int_{-\frac{3}{2}L}^{+\frac{3}{2}L} dy \right] I_{out} = \\
 &= -\overline{a_{90}} \cdot 4 \int_{-\frac{3}{2}L}^{+\frac{3}{2}L} dx \int_{+\frac{3}{2}L}^{+\frac{5}{2}L} dy \Psi_{00} \frac{1}{\sqrt{2}} (\Psi_{20} - \Psi_{02}) = k_{55}(L, w_0) \cdot \overline{a_{90}}
 \end{aligned} \tag{3.61}$$

The corresponding signal is extracted from the following sum of intensities:

$$S_5 = \sum_{n=2}^{m=-1,0,1} I_{n,m} + \sum_{n=-2}^{m=-1,0,1} I_{n,m} - \sum_{n=-1,0,1}^{m=2} I_{n,m} - \sum_{n=-1,0,1}^{m=-2} I_{n,m} \tag{3.62}$$

Finally, the coefficient of Defocus is due to the contribution of $\Psi_{00} \frac{1}{\sqrt{2}} (\Psi_{20} + \Psi_{02})$ whose surface on the square domain of the photodiodes

has already been plotted in figure 3.14.

The contribution of the Defocus can be obtained by:

$$\begin{aligned}
 S_6 = & \left(\int_{-\frac{5}{2}L}^{+\frac{5}{2}L} dx \int_{+\frac{3}{2}L}^{+\frac{5}{2}L} dy + \int_{-\frac{5}{2}L}^{+\frac{5}{2}L} dx \int_{-\frac{5}{2}L}^{-\frac{3}{2}L} dy + \int_{+\frac{3}{2}L}^{+\frac{5}{2}L} dx \int_{-\frac{3}{2}L}^{+\frac{3}{2}L} dy + \right. \\
 & \left. + \int_{-\frac{5}{2}L}^{-\frac{3}{2}L} dx \int_{+\frac{3}{2}L}^{+\frac{3}{2}L} dy - \int_{-\frac{3}{2}L}^{-\frac{5}{2}L} dx \int_{+\frac{3}{2}L}^{+\frac{3}{2}L} dy \right) \left[(1 + \phi) |\Psi_{00}|^2 + \overline{a_D} \cdot \Psi_{00} \frac{1}{\sqrt{2}} (\Psi_{20} + \Psi_{02}) \right] = \\
 & = k_{61}(L, w_0) \cdot (1 + \phi) + k_{66}(L, w_0) \cdot \overline{a_D}
 \end{aligned} \tag{3.63}$$

corresponding to:

$$S_6 = \sum_{n=-2, -1, 0, 1, 2}^{m=2} I_{n,m} + \sum_{n=-2, -1, 0, 1, 2}^{m=-2} I_{n,m} + \sum_{n=2}^{m=-1, 0, 1} I_{n,m} + \sum_{n=-2}^{m=-1, 0, 1} I_{n,m} + \sum_{n=-1, 0, 1}^{m=-1, 0, 1} I_{n,m} \tag{3.64}$$

In conclusion, using the 6 correspondences shown above, we can calculate the 6 error signals ($S_1..S_6$) of eq. (3.52) by suitable combinations of the measured intensities $I_{n,m}$, as summarized in the following table 3.1.

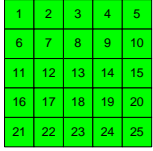

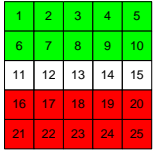



Aberration Signal	Theoretical estimate	Combination of the 25 intensities + -
<i>Longitudinal</i> S_1	$k_{11}(L, w_0)(1 + \phi) + k_{16}(L, w_0)\overline{a_D}$	
<i>TiltX</i> S_2	$k_{22}(L, w_0) \cdot \overline{a_x}$	
<i>TiltY</i> S_3	$k_{33}(L, w_0) \cdot \overline{a_y}$	
<i>Astigmatism45</i> S_4	$k_{44}(L, w_0) \cdot \overline{a_{45}}$	
<i>Astigmatism90</i> S_5	$k_{55}(L, w_0) \cdot \overline{a_{90}}$	
<i>Defocus</i> S_6	$k_{61}(L, w_0) \cdot (1 + \phi) + k_{66}(L, w_0) \cdot \overline{a_D}$	

Table 3.1: signal extraction of the six aberration coefficients from the combination of the 25 intensities $I_{n,m}$ emerging from the photodiodes array (green represents addition and red subtraction). S_i are the error signals reintroduced into the feedback control.

The 6x6 matrix equation (3.52) reduces to:

$$\begin{pmatrix} S_1 \\ S_2 \\ S_3 \\ S_4 \\ S_5 \\ S_6 \end{pmatrix} = \begin{pmatrix} k_{11} & 0 & 0 & 0 & 0 & k_{16} \\ 0 & k_{22} & 0 & 0 & 0 & 0 \\ 0 & 0 & k_{33} & 0 & 0 & 0 \\ 0 & 0 & 0 & k_{44} & 0 & 0 \\ 0 & 0 & 0 & 0 & k_{55} & 0 \\ k_{61} & 0 & 0 & 0 & 0 & k_{66} \end{pmatrix} \cdot \begin{pmatrix} \phi \\ \overline{a_x} \\ \overline{a_y} \\ \overline{a_{45}} \\ \overline{a_{90}} \\ \overline{a_D} \end{pmatrix} + \begin{pmatrix} k_{11} \\ 0 \\ 0 \\ 0 \\ 0 \\ k_{61} \end{pmatrix} \quad (3.65)$$

and still exhibits non null off diagonal elements that are the coefficients k_{16} and k_{61} due to the coupling between longitudinal mode ϕ and Defocus a_D . The other four modes are completely decoupled.

The coefficients k_{ij} correspond to scalar products of Hermite Gauss functions over the domain of the photodiodes array and depend on the ratio w_0/L . By suitably manipulating this ratio, we can reduce the off diagonal elements and in the same time maintain non null values for the diagonal terms.

In particular, if w_0/L tends to infinite (from a mathematical point of view this corresponds to integrate over a null range and from a physical point of view it means that the photodiodes have zero sensing area) all the coefficients are null and no measurement of aberration can be done. Therefore this case should be avoided.

On the contrary, let us consider the case when w_0/L tends to zero. From a mathematical point of view it means that the range of integration is $[-\infty, +\infty]$ while the physical meaning is that the beam is focused at the center of the matrix on the pixel no.13. We can see that the coefficients k_{11} , k_{22} , k_{33} and k_{44} have non null and constant values while the off diagonal element k_{16} tends to zero in accordance with the fact that the functions Ψ_{00} and $\frac{1}{\sqrt{2}}(\Psi_{20} + \Psi_{02})$

are orthogonal in the range $[-\infty, +\infty]$. But, the coefficients k_{55} and k_{66} are null and k_{61} tends to -1. So, we lose any information about Astigmatism90 and Defocus and have a high off diagonal element. Therefore the case $w_0/L \rightarrow 0$ should be avoided too.

We have found a trade off between the two extreme conditions and achieved large and stable diagonal elements and small off diagonal terms.

<i>Coefficient</i>	$w_0/L \rightarrow \infty$	$w_0/L \rightarrow 0$	$1.4 < w_0/L < 1.6$
k_{11}	0	1	0.99
k_{22}	0	0.8	0.78
k_{33}	0	0.8	0.78
k_{44}	0	0.64	0.6
k_{55}	0	0	0.4
k_{66}	0	0	0.65
k_{16}	0	0	-0.1
k_{61}	0	-1	-0.3

Table 3.2: coefficients k_{ij} in the extreme cases $w_0/L \rightarrow \infty$ and $w_0/L \rightarrow 0$ and at the trade off $1.4 < w_0/L < 1.6$

The trade off value is chosen in the range $1.4 < w_0/L < 1.6$: in fact, in this region all the coefficients k_{ii} are near their maxima and vary slowly with w_0/L , the coefficient k_{61} is negligible and k_{16} has a relative amplitude of 30% (see table 3.2).

In this condition the Controlled System is characterized and the transfer matrix K is diagonalized.

3.6 Calculation of the 6x6 transfer matrix A of the Regulator and diagonalization of the 6x6 matrix G relative to the open loop system

In order to complete design and characterization of our system, we need to investigate the matrix A of the Regulator from which we get the open loop gain $G=KA$.

To do that, we have initially locked the interferometer on the middle fringe state by closing the loop of the piezoelectric mirror as shown in figure 3.19.

Successively, we have measured the AO system response $S(t)$ to the reference signal $R(t)$ per each of the six degrees of freedom.

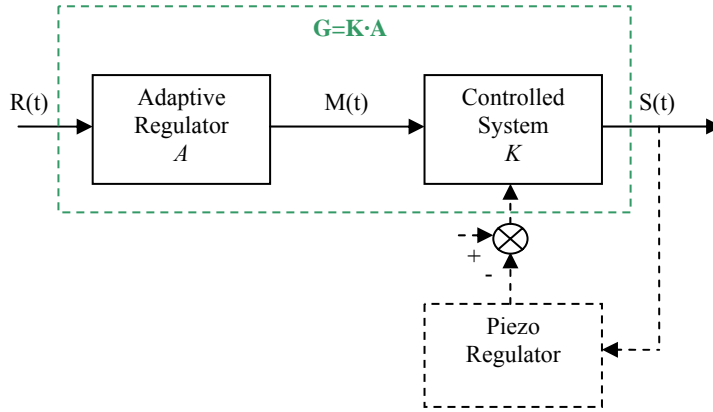


Figure 3.19: block diagram of the control system for calculation and diagonalization of G

In particular, with reference to figure 3.10, the first step has been the calculation of the 59×6 matrix U of the Combinator 2 that transforms the 6 reference signals into a set of 59 voltages V_h , $h=1,2,...,59$, according to:

$$\begin{pmatrix} V_1 \\ \cdot \\ \cdot \\ \cdot \\ V_{59} \end{pmatrix} = \begin{pmatrix} u_{11} & \dots & u_{16} \\ \cdot & \dots & \cdot \\ \cdot & \dots & \cdot \\ \cdot & \dots & \cdot \\ u_{59,1} & \dots & u_{59,6} \end{pmatrix} \cdot \begin{pmatrix} R_1 \\ \cdot \\ \cdot \\ \cdot \\ R_6 \end{pmatrix} \quad (3.66)$$

These voltages are applied to the electrostatic actuators of the adaptive mirror and deform its reflective surface due to attractive force. So, the wavefront of the laser beam incident on the mirror is modulated and after reflection it is described by the aberration vector $M(t)$ in accordance with the equation $M(t)=AR(t)$.

If we want to calculate the terms of the matrix U of the Combinator 2 we have to consider the geometry of the electrostatic actuators placed on the rear side of the mirror deformable membrane. Let us assume that the actuators array is centred on the x,y plane and that each electrode has its midpoint at the coordinates (x_h, y_h) , $h=1,2,...,59$, as shown in figure 3.20.

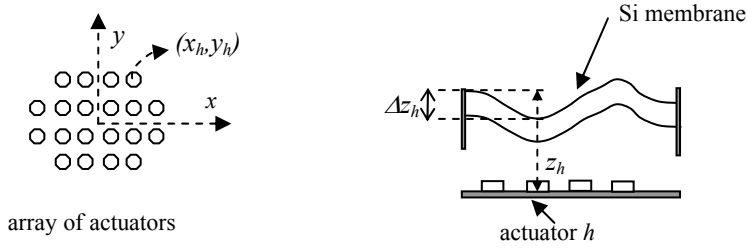


Figure 3.20: schematic of the actuators array (top view on the left) and deformable membrane (side view on the right). The actuators are placed below the reflecting surface that is moved by electrostatic forces

The electrostatic force is supposed to act as it was exactly concentrated in the center of each of the 59 actuators. We also assume that in each point the applied voltage causes the proportional displacement of that portion of surface (at first approximation we neglect non linearity effects of the membrane bond at its boundary). Then, if Δz_h ($h=1,2,\dots,59$) is in each point the displacement from the equilibrium position, we can achieve the desired pattern of the membrane by applying a set of voltages that are point by point proportional to the corresponding value of Δz_h .

For each degree of freedom the deformable surface should match one of the six geometrical configurations represented by the six Zernike polynomials. So, each of these six polynomials is calculated in the 59 positions (x_h, y_h) and the values are exactly the voltages that must be applied to get the corresponding configuration of the mirror membrane.

For example, if we want to find the set of 59 voltages corresponding to aberration a_y , which is the third degree of freedom in our system, we calculate the Zernike polynomial Z_1^{-1} in each of the 59 centres (x_h, y_h) of the actuators. The 59 values are exactly the 59 voltages that must be applied to the actuators and therefore they correspond to the third column u_{h3} ($h=1,2,\dots,59$) of the matrix U . Similarly we can calculate the other columns of U using the other Zernike polynomials until the transfer matrix of the Combinator 2 is completely defined.

After that, we determine the coefficients g_{ij} of the 6x6 matrix G relative to the open loop system of figure 3.19 which is described by the matrix equation:

$$\begin{pmatrix} S_1 \\ S_2 \\ S_3 \\ S_4 \\ S_5 \\ S_6 \end{pmatrix} = \begin{pmatrix} g_{11} & g_{12} & g_{13} & g_{14} & g_{15} & g_{16} \\ g_{21} & g_{22} & g_{23} & g_{24} & g_{25} & g_{26} \\ g_{31} & g_{32} & g_{33} & g_{34} & g_{35} & g_{36} \\ g_{41} & g_{42} & g_{43} & g_{44} & g_{45} & g_{46} \\ g_{51} & g_{52} & g_{53} & g_{54} & g_{55} & g_{56} \\ g_{61} & g_{62} & g_{63} & g_{64} & g_{65} & g_{66} \end{pmatrix} \cdot \begin{pmatrix} R_1 \\ R_2 \\ R_3 \\ R_4 \\ R_5 \\ R_6 \end{pmatrix} \quad (3.67)$$

where $R_i(t)$ are reference input signals that we introduce into the Regulator to directly measure the response of the system.

In particular, if we apply input signals to only one of the 6 degrees of freedom, for example R_3 which corresponds to TiltY, eq. (3.67) reduces to:

$$\begin{pmatrix} S_1 \\ S_2 \\ S_3 \\ S_4 \\ S_5 \\ S_6 \end{pmatrix} = \begin{pmatrix} g_{11} & g_{12} & g_{13} & g_{14} & g_{15} & g_{16} \\ g_{21} & g_{22} & g_{23} & g_{24} & g_{25} & g_{26} \\ g_{31} & g_{32} & g_{33} & g_{34} & g_{35} & g_{36} \\ g_{41} & g_{42} & g_{43} & g_{44} & g_{45} & g_{46} \\ g_{51} & g_{52} & g_{53} & g_{54} & g_{55} & g_{56} \\ g_{61} & g_{62} & g_{63} & g_{64} & g_{65} & g_{66} \end{pmatrix} \cdot \begin{pmatrix} 0 \\ 0 \\ R_3 \\ 0 \\ 0 \\ 0 \end{pmatrix} = \begin{pmatrix} g_{13}R_3 \\ g_{23}R_3 \\ g_{33}R_3 \\ g_{43}R_3 \\ g_{53}R_3 \\ g_{63}R_3 \end{pmatrix} \quad (3.68)$$

Thus, by measurement of the six output signals S_i we calculate the coefficients g_{i3} ($i=1,2,...6$) representing the third column of the matrix G . Similarly, if we send the reference input signal R_i per each degree of freedom, we measure all the columns of G . It is worth noting that the coefficients g_{ij} are transfer functions and therefore their measurement consists into the complete characterization of $g_{ij}(\omega)$ in terms of amplitude and phase as it is widely discussed in Chapter 5.

For the system efficiency and stability it is strongly recommended that the matrix G is diagonal and therefore we need to check per each column if the off diagonal elements g_{ij} ($i \neq j$) are null or at least very small compared with the diagonal terms g_{ii} .

If this condition is fulfilled the system is ready to operate. If not, and this is commonly the case due to coupling effects, we must find a procedure for the diagonalization.

The method that we adopt is based on the manipulation of the matrix U by suitably changing one or more of its columns till reaching the diagonalization of G . In detail, let us consider to introduce into the system an input signal

$R_i(t)$ for a certain degree of freedom and measure the corresponding column of the matrix G . If one off diagonal element associated to the degree of freedom $j \neq i$ is comparable with the diagonal term associated to I , we change the set of 59 voltages of the matrix U (associated to i) by subtracting at each actuator a voltage proportional to the value used to generate the deformation associated with j . The physical meaning is clearly understood: if we excite the mirror on one degree of freedom and it responds exciting also a second degree of freedom for coupling effects, we can compensate by subtracting to the input excitation a signal that is proportional to the excitation on the second undesired mode. This method can be iteratively performed until the off diagonal term is acceptably lower than the diagonal coefficient. We can analytically demonstrate this method using the matrix equations of the system.

The matrix A of the Regulator can be detailed as:

$$A(6 \times 6) = \begin{pmatrix} dm_{11} & \dots & dm_{1,59} \\ \cdot & \dots & \cdot \\ \cdot & \dots & \cdot \\ \cdot & \dots & \cdot \\ dm_{61} & \dots & dm_{6,59} \end{pmatrix} \cdot \begin{pmatrix} u_{11} & \dots & u_{16} \\ \cdot & \dots & \cdot \\ \cdot & \dots & \cdot \\ \cdot & \dots & \cdot \\ u_{59,1} & \dots & u_{59,6} \end{pmatrix} \quad (3.69)$$

where dm_{ij} ($i=1, \dots, 6$ and $j=1, \dots, 59$) is the transfer matrix of the deformable mirror that transforms the set of 59 voltages into 6 different geometrical configurations of the membrane. In this equation, for the sake of simplicity, we have neglected the matrices of the filter, the DAC and the amplifier, that are diagonal and do not influence the present demonstration.

The matrix G of the system is given by:

$$\begin{aligned}
G(6 \times 6) = K \cdot A = & \begin{pmatrix} k_{11} & 0 & 0 & 0 & 0 & 0 \\ 0 & k_{22} & 0 & 0 & 0 & 0 \\ 0 & 0 & k_{33} & 0 & 0 & 0 \\ 0 & 0 & 0 & k_{44} & 0 & 0 \\ 0 & 0 & 0 & 0 & k_{55} & 0 \\ k_{61} & 0 & 0 & 0 & 0 & k_{66} \end{pmatrix} \times \\
& \times \begin{pmatrix} dm_{11} & \dots & dm_{1,59} \\ \cdot & \dots & \cdot \\ \cdot & \dots & \cdot \\ \cdot & \dots & \cdot \\ dm_{61} & \dots & dm_{6,59} \end{pmatrix} \cdot \begin{pmatrix} u_{11} & \dots & u_{16} \\ \cdot & \dots & \cdot \\ \cdot & \dots & \cdot \\ \cdot & \dots & \cdot \\ u_{59,1} & \dots & u_{59,6} \end{pmatrix} \quad (3.70)
\end{aligned}$$

neglecting the term k_{16} as stated in the previous Section.

Let us assume that in the third column corresponding to TiltY the term g_{13} associated to longitudinal mode is comparable with g_{33} . This physically means that if we induce on the mirror rigid rotation around Y axis with command R_3 we also induce for coupling effect the partial longitudinal translation as if the mirror was excited by the command R_1 . We can compensate this undesired effect subtracting from the mode R_3 a signal proportional to the longitudinal mode. To do that, we modify the third column of U , given by the coefficients u_{i3} , subtracting per each i the corresponding term $-\alpha u_{i1}$, being α a real constant suitably chosen.

We rewrite eq. (3.70) in the form:

$$g_{ij} = \begin{pmatrix} k_{11} \sum_{h=1}^{59} dm_{1h} u_{h1} & \cdot & k_{11} \sum_{h=1}^{59} dm_{1h} u_{h3} & \dots & \dots & \dots \\ \cdot & \cdot & \cdot & \dots & \dots & \dots \\ k_{33} \sum_{h=1}^{59} dm_{3h} u_{h1} & \cdot & k_{33} \sum_{h=1}^{59} dm_{3h} u_{h3} & \dots & \dots & \dots \\ \cdot & \cdot & \cdot & \dots & \dots & \dots \\ \cdot & \cdot & \cdot & \dots & \dots & \dots \\ \cdot & \cdot & \cdot & \dots & \dots & \dots \end{pmatrix} \quad (3.71)$$

where attention is paid to terms g_{11} , g_{13} , g_{31} and g_{33} which are involved in our demonstration.

From simple algebra we see that, if the coefficients u_{i3} are reduced by $-\alpha u_{i1}$, the matrix g_{ij} is transformed into:

$$g_{ij}^1 = \begin{pmatrix} g_{11} & \cdot & g_{13}^1 & \dots\dots\dots \\ \cdot & \cdot & \cdot & \dots\dots\dots \\ g_{31} & \cdot & g_{33}^1 & \dots\dots\dots \\ \cdot & \cdot & \cdot & \dots\dots\dots \\ \cdot & \cdot & \cdot & \dots\dots\dots \\ \cdot & \cdot & \cdot & \dots\dots\dots \end{pmatrix} \quad (3.72)$$

where the apical label 1 refers to the first step of iteration.
In particular, the coefficients of the third column are:

$$\begin{cases} g_{13}^1 = g_{13} - \alpha g_{11} \\ g_{33}^1 = g_{33} - \alpha g_{31} \end{cases} \quad (3.73)$$

Under the assumption that g_{11} is big compared with g_{31} , this last equation provides that g_{13}^1 is strongly reduced in comparison with g_{33}^1 . Clearly in the opposite case, if $g_{11} < g_{31}$, we can change the sign of α and obtain that g_{33}^1 increases much more than g_{13}^1 . In both cases, we maximize the diagonal term with respect to the off diagonal elements.

If necessary, we can iteratively repeat the operations until the coefficients at the step n fulfil our requirements

$$\begin{cases} g_{13}^n = g_{13} - n\alpha g_{11} \\ g_{33}^n = g_{33} - n\alpha g_{31} \end{cases} \quad (3.74)$$

Usually the diagonalization is quite well achieved after few iterations.
At the end of this procedure the residual off diagonal terms of matrix G can be neglected and eq. (3.67) transforms to:

$$\begin{pmatrix} S_1 \\ S_2 \\ S_3 \\ S_4 \\ S_5 \\ S_6 \end{pmatrix} = \begin{pmatrix} g_{11} & 0 & 0 & 0 & 0 & 0 \\ 0 & g_{22} & 0 & 0 & 0 & 0 \\ 0 & 0 & g_{33} & 0 & 0 & 0 \\ 0 & 0 & 0 & g_{44} & 0 & 0 \\ 0 & 0 & 0 & 0 & g_{55} & 0 \\ 0 & 0 & 0 & 0 & 0 & g_{66} \end{pmatrix} \begin{pmatrix} R_1 \\ R_2 \\ R_3 \\ R_4 \\ R_5 \\ R_6 \end{pmatrix} \quad (3.75)$$

which describes the dynamics of the AO control system at open loop. Similarly, the dynamics of the AO control at closed loop is described by:

$$\begin{pmatrix} S_1 \\ S_2 \\ S_3 \\ S_4 \\ S_5 \\ S_6 \end{pmatrix} = \begin{pmatrix} f_{11} & 0 & 0 & 0 & 0 & 0 \\ 0 & f_{22} & 0 & 0 & 0 & 0 \\ 0 & 0 & f_{33} & 0 & 0 & 0 \\ 0 & 0 & 0 & f_{44} & 0 & 0 \\ 0 & 0 & 0 & 0 & f_{55} & 0 \\ 0 & 0 & 0 & 0 & 0 & f_{66} \end{pmatrix} \begin{pmatrix} R_1 \\ R_2 \\ R_3 \\ R_4 \\ R_5 \\ R_6 \end{pmatrix} \quad (3.76)$$

where the transfer functions f_{ii} belong to matrix F of eq. (3.47) and are related to the terms g_{ii} as:

$$f_{ii} = \frac{g_{ii}}{1 + g_{ii}} \quad (3.77)$$

This last equation expresses per each degree of freedom the relationship between the open loop gain and the closed loop response of the control system.

Chapter 4

Implementation of the Prototype

Our Doctoral Thesis has started from the presentation of the Virgo Project for the detection of gravitational waves. We have shortly discussed the problem of noise reduction in the Virgo antenna and in particular we have focused our attention to the noise originated by the coupling between the interferometer asymmetries and the input laser beam jitters. The reduction of this kind of noise is still an open issue in actual GW interferometric detectors as well as in the advanced antennas that are going to be implemented in the next future. In fact, none of the techniques up to date proposed has yet demonstrated to fulfil the specific requirements for the reduction of laser beam jitters.

We have investigated the wide scenario of the Adaptive Optics technology, the state of the art and the current applications in the fields of Astronomy, Industry and Medicine. This research has allowed us to see that actual AO systems, although very performing for their specific applications, do not satisfy the statements of wideband and high sensitivity laser jitters reduction requested for GW detectors.

Starting from this context, we have proposed a novel AO system based on the interferometric detection of the perturbed wavefront, upon the persuasion that our system could meet the Virgo requirements. In particular, we have developed the theoretical model that predicts the dynamical behaviour of the system and designed the architecture of the optical scheme and of the adaptive control.

The following of our PhD work has consisted in the implementation of the first prototype for the characterization and the validation of the Project.

In this fourth Chapter we present the scheme of the AO system Prototype that we have put into operation in the laboratory of Applied Optics at the University of Salerno. We detail the geometry of the Michelson configuration and the characteristics of the main components. Whenever necessary attention is paid to put in evidence that the experimental setup has been built in strict compliance with the statements of the design, because this is the first condition for the success of the Project.

We present the He Ne Laser Source that has been introduced into the interferometer for the correction of the jitters, reporting the technical data and the characteristics given by the manufacturer Melles Griot. We also show the characteristics of the Adaptive Mirror produced by OKO on Micromachined

Deformable Membrane technology and driven by its own electronics. The overview of the main components is ended with the description of the array of photodiodes made by Hamamatsu and amplified by electrical boards that we have designed and made for that purpose.

A short section is devoted to the mode matching between the input laser beam and the interferometer; in particular we show the optical arrangement for the positioning of the beam waist on the adaptive mirror and on the pixellated array of photodiodes.

Finally, we describe the data processor of the closed loop control and the blocks of operative functions that we have performed using LabView on a standard PC.

4.1 Architecture of the AO interferometric system

We have implemented the Prototype of the AO system in the Applied Physics laboratory led by Professor Fabrizio Barone at the University of Salerno.

The optical configuration is based on the typical scheme of the Michelson interferometer as shown in figure 4.1. In order to test the technique of wavefront control, we assume that arm 1 is passed through by the reference unperturbed beam and arm 2 is passed through by the aberrated beam that we want to clean up. In fact, the two beams that recombine at the output of the Michelson form an interference figure that is used to generate 6 signals proportional to the six aberration modes as discussed in detail in Chapter 3. These signals are subtracted from the reference set point to produce the error signals sent to the deformable mirror.

The experimental control loop has been closed using a LabView Virtual Instrument running on standard PC for the data processing from the sensing element to the actuator.

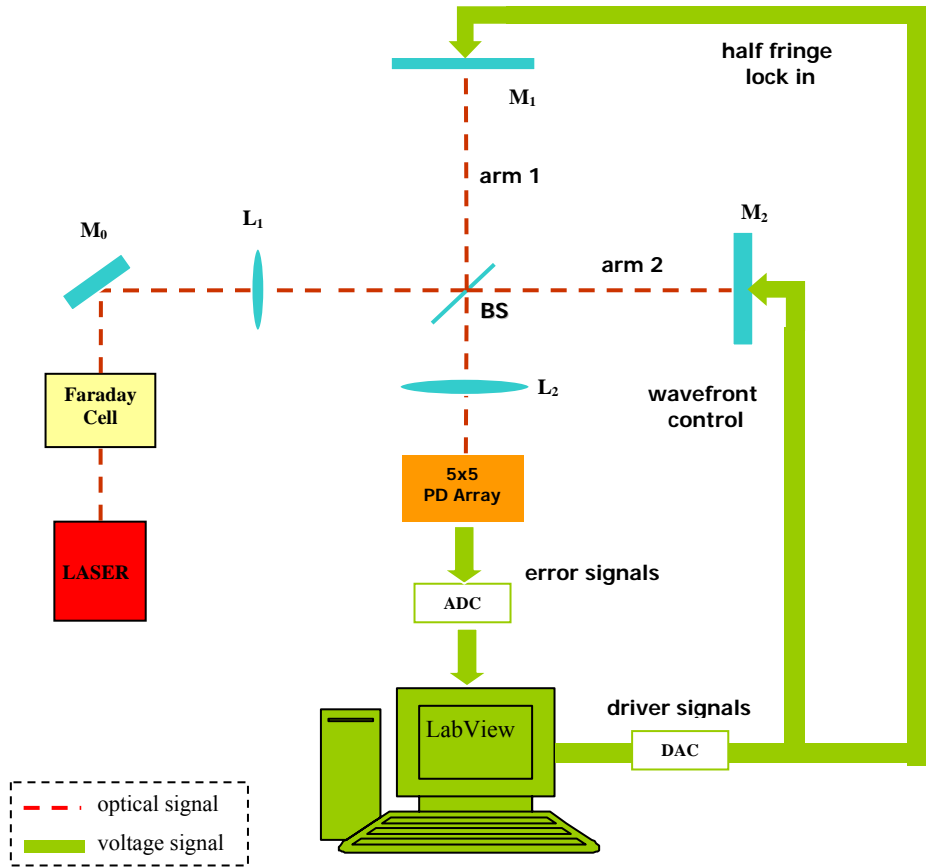


Figure 4.1. Optical Scheme of the Adaptive Optics System Prototype. M_0 mirror for TiltX and TiltY alignment, L_1 convergent lens for the mode matching with the adaptive mirror M_2 , L_2 convergent lens for the mode matching with the 5x5 PD-Photodiodes Array. BS is the beam splitter and M_1 the piezoelectric mirror for the middle fringe lock in. The 25 voltage output signals emerging from the photodiodes are collected by the ADC board and sent to the PC where the Labview Virtual Instrument processes the data and generates the command signals. These are converted by the DAC into analogical form and sent through dedicated bus to the Piezo and to the Adaptive mirrors for the lock in and the wavefront control respectively. The equipment is installed on a seismically isolated bench.

The source of the input beam is a stabilized Laser He-Ne, $\lambda=632.8 \text{ nm}$, $P=1 \text{ mW}$, made by Melles Griot, which is passed through a Faraday cell to avoid disturbances due to light back reflected by the interferometer. The mirror M_0 is used for the first optical adjustment as it allows to correct macroscopic TiltX and TiltY misalignments.

The spot size is matched to the adaptive mirror and to the photodiodes array using the lenses L_1 and L_2 respectively, as we describe in the following.

The input beam is split into two half intensity parts by the beam splitter BS. One half beam runs in arm 1 and is used for the lock in of the interferometer on the half fringe working point using the piezoelectric mirror M_1 . The other beam passes through the arm 2 and is corrected by the Adaptive mirror M_2 .

The interference fringe pattern at the output of the Michelson is collected by the 5x5 rectangular array of photodiodes that generate 25 voltage signals sent to the ADC board for the digital conversion.

The closed loop control for the lock in and the adaptive correction is performed using the Labview programmed PC that processes the data coming from the photodiodes and generates the command signals for the actuators. From the scheme of figure 4.1 we see that a part of commands is generated for the piezoelectric actuator and another set of voltages is produced for the adaptive mirror. In both cases the voltage signals are first converted by the DAC into analogical form and then sent to the actuators through dedicated bus lines. All the equipments are installed on a seismically isolated bench manufactured by Newport.

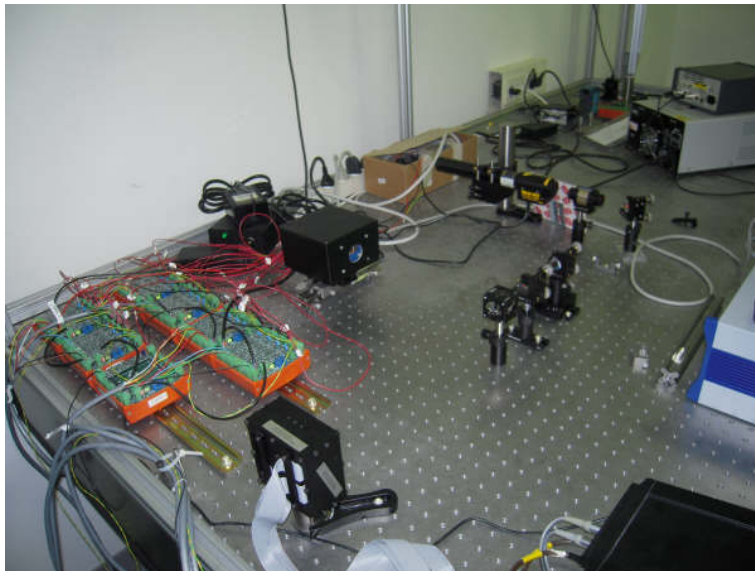


Figure 4.2: Picture of the Adaptive Optics System Prototype implemented at the University of Salerno in the laboratory of Applied Optics led by Professor Fabrizio Barone

Figure 4.2 shows the picture of the experimental setup implemented in our laboratory for the tests of characterization.

4.2 Laser Source

The Laser source is a stabilized Laser He-Ne, $\lambda=632.8$ nm, $P=1$ mW, made by Melles Griot [97].



Figure 4.3: picture of the stabilized Helium Neon laser used in the experimental setup

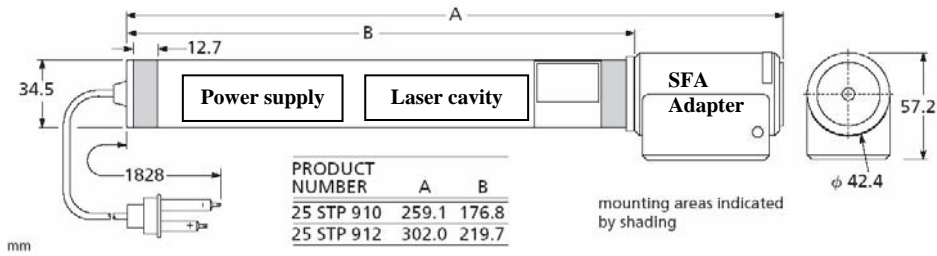


Figure 4.4: scheme of the laser manufactured by Melles Griot. The product we have used is the code 25 STP 912

It is ideal for such applications as interferometry which require a single, invariant frequency with large coherence length. In fact, it oscillates on a single-longitudinal-mode and has a coherence length measured in kilometres. It also exhibits excellent power stability for long periods of time ($<0.2\%$ power fluctuation over 8 hours), while the frequency stability is 1 MHz at nominal frequency 473.61254 THz

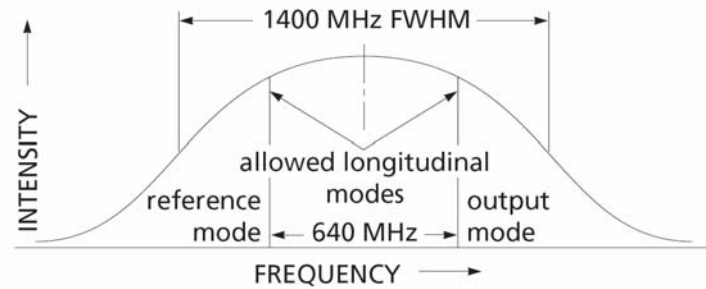


Figure 4.5: helium neon gain curve showing two orthogonally polarized modes. Only one of them is allowed to exit the system

The laser system produces two orthogonally polarized longitudinal modes as shown in figure 4.5. The two modes are separated into two beams by polarization components and their amplitudes are compared electronically. The cavity length is then adjusted to maintain the proper relationship between the modes. Only one beam is allowed to exit the system.

The transverse mode is the fundamental Gaussian TEM_{00} with beam diameter ($1/e^2$) equal to 0.54 mm and full cone beam divergence of 1.5 mrad [98]. This corresponds to the beam waist $w_0 = 0.27 \text{ mm}$ and the far field diffraction angle

$$\theta = \frac{\lambda}{\pi w_0} = 0.75 \text{ mrad}, \text{ according to the geometry pictured in figure 4.6.}$$

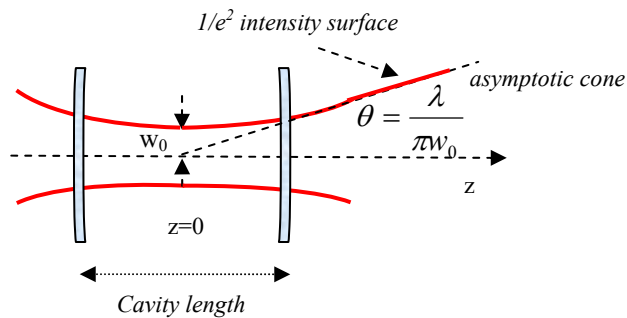


Figure 4.6: propagation of the laser beam from waist plane to far field

4.3 Adaptive mirror

The adaptive mirror used as actuator for the wavefront correction is a Micromachined Membrane Deformable Mirror (MMDM) manufactured by OKO Technologies Flexible Optical B.V. and driven by proprietary electronics. It is produced on the technology of silicon bulk micromachining widely diffused in the field of the Micro Electro Mechanical Systems (MEMS) [99].

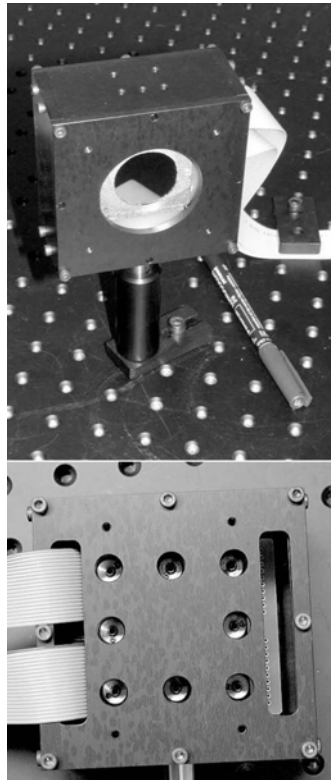


Figure 4.7: front side and back side of the deformable mirror manufactured by OKO

The device is made of a silicon chip mounted over a concentric electrostatic electrode structure. The chip contains the multilayer silicon nitride membrane specially coated on the front side for the realization of the mirror reflecting surface. The control electrode structure is contained in the PCB. The scheme of the system is illustrated in figure 4.8.

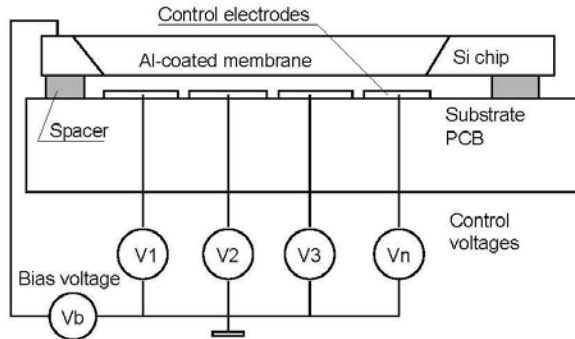


Figure 4.8: schematic section of the micromachined adaptive mirror

The reflective membrane has a circular shape of 30 mm diameter and its initial profile can be adjusted using 8 micrometric screws placed on the back side of the mirror mount. After, the attractive force applied by the actuators induces deformation of the membrane with maximum deflection at the center of 15 μm on bandwidth of 500 Hz, that at the state of the present technology sets the upper limit to the frequency response of the whole control system. The array of 59 actuators under the membrane is formed by electrodes printed on the basis of the PCB to form a circular structure of 20 mm diameter.

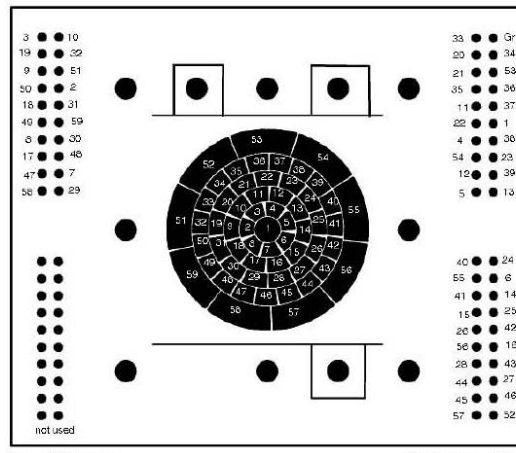


Figure 4.9: array of 59 electrodes disposed on the PCB in circular form with 20 mm total diameter

The electrodes are addressed to 59 channels grouped into three sets of voltages generated by three 24ch 8 bit PCI DAC boards [100] in cascade with

three high voltage driver boards. Each of the three amplifiers contains 20 non-inverting DC amplifiers with gain 59 that raise the voltage up to 300V for the electrodes. The electrical scheme of the DC amplifier is shown in the figure below.

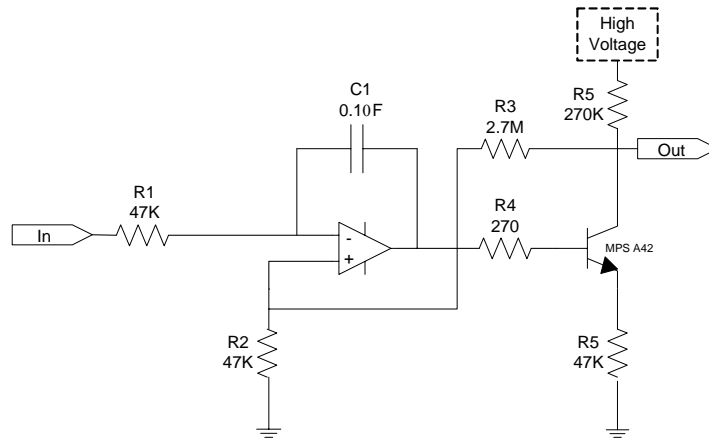


Figure 4.10: electrical scheme of the DC amplifier driving the electrode actuator of the deformable membrane (OKO proprietary electronics)

4.4 Array of photodiodes

The sensor at the output of the Michelson is an array of 25 of photodiodes manufactured on a 28 pin chip by Hamamatsu Photonics [101].

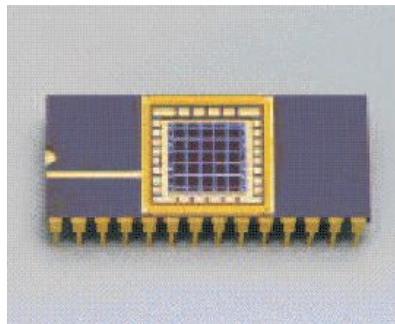


Figure 4.11: 28 pin chip Hamamatsu containing the 5x5 photodiodes array

The 2-D array is arranged in a 5x5 square matrix with active area of total dimension $7.3 \times 7.3 \text{ mm}^2$. In particular each single pixel has an active area of $1.3 \times 1.3 \text{ mm}^2$ and a spacing distance of 0.2 mm from the next one. Therefore the element pitch (center to center spacing) is 1.5 mm both in the X and Y direction. The array is encapsulated into a window of flat glass.

Each photodiode can be inversely polarized by the maximum reverse voltage of 15 V and operates in the temperature range from -20 to $60 \text{ }^\circ\text{C}$.

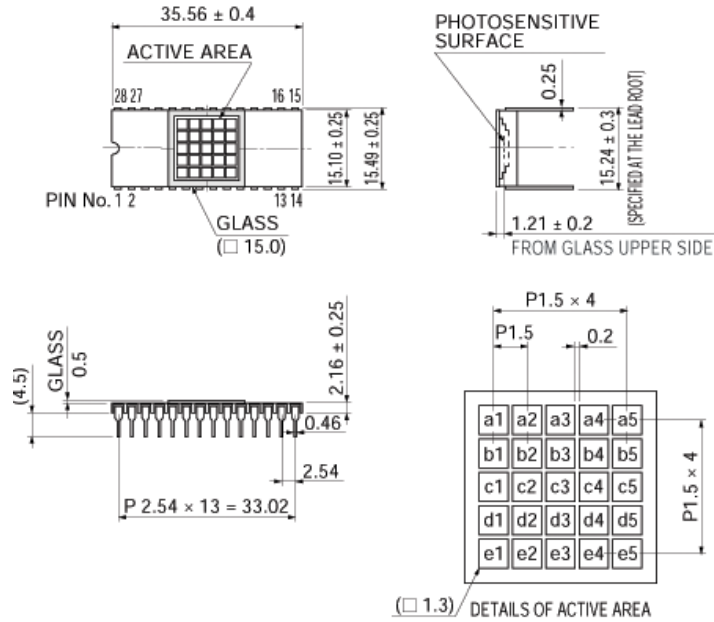


Figure 4.12: dimensional outline of the photodiodes array (unit: mm)

Concerning electrical and optical characteristics, the spectral response ranges from $\lambda=320 \text{ nm}$ to $\lambda=1000 \text{ nm}$ with peak sensitivity wavelength $\lambda_p=800 \text{ nm}$ where the photosensitivity curve of the photodiode reaches 0.5 A/W . The sensor bandwidth is 170 MHz and therefore it can be considered flat over the range of interest that does not overcome few kHz .

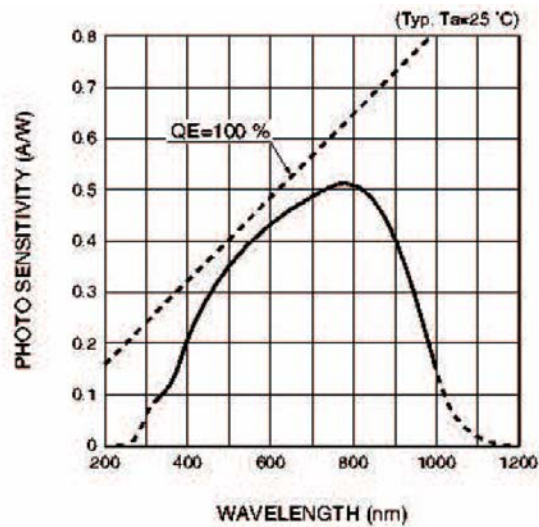


Figure 4.13: spectral response of the photodiodes

The signal conditioning of the photocurrents emerging from the 25 photodiodes is performed by electronics that we have properly designed and engineered for the operation of our system. In particular, we have implemented 25 small electronic boards allocated in groups of 5 into suitable cases which also provide for the supply (see figure 4.14). Each circuit receives one the 25 photocurrents, converts into voltage form and amplifies the signal before it is transformed into digital form by the ADC.

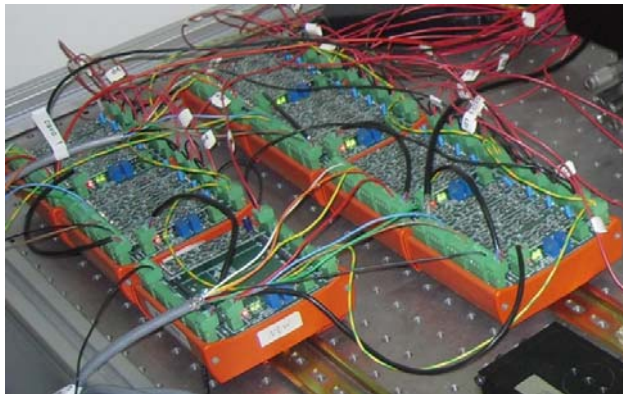


Figure 4.14: picture of the 25 photodiode amplifier allocated into the cases and connected to rest of the system

The block diagram of the amplifier is shown in figure 4.15. It is a DC coupled analogical circuit based on the technology of operational amplifiers with feedback impedance [102], [103].

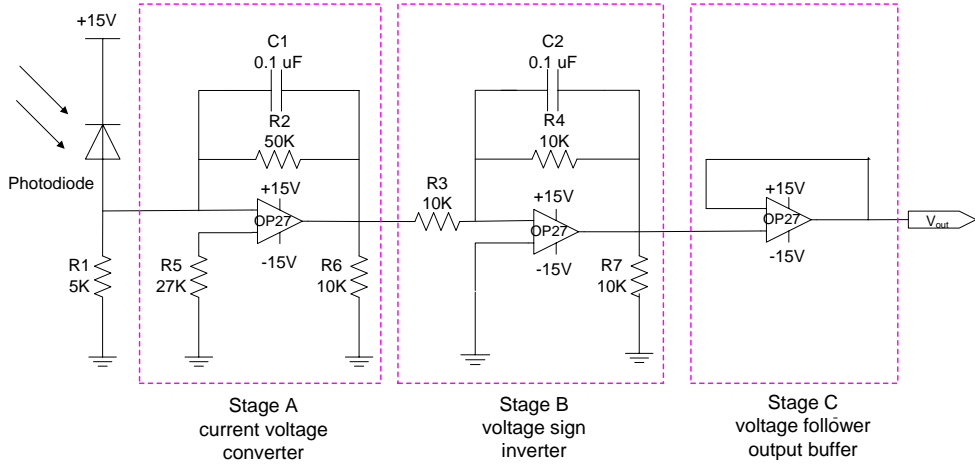


Figure 4.15: block diagram of the photodiode amplifier based on the operational OP27

We have used the operational OP27 manufactured by Analog Devices [104] into three different stages.

The Stage A is the current voltage converter that collects the photocurrent of the inversely biased photodiode and produces the proportional voltage. If we consider the photodiode as ideal generator of current I_{PD} , we can calculate the voltage at the input of the Stage A using the Thévenin equivalent circuit of the photodiode in series with the resistor R_1 as in figure 4.16. In this case we have the voltage generator $V_{th}=I_{PD} \cdot R_1$ in series with the impedance $R_{th}=R_1$.

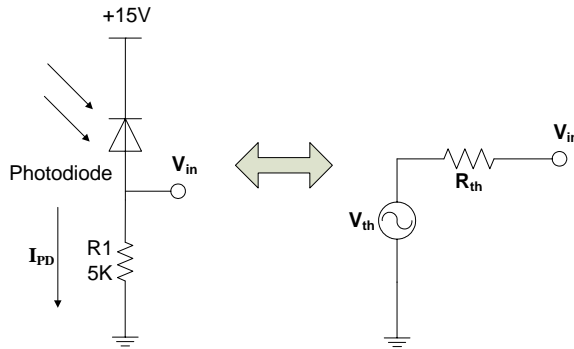


Figure 4.16: Thévenin equivalent circuit of the photodiode circuit. $V_{th}=R_1 I_{PD}$ and $R_{th}=R_1$

Therefore, from the theory of the operational amplifiers with feedback impedance, the voltage at the output of Stage A is given by:

$$V_0^A = -\frac{R_2}{R_1} V_{th} = -\frac{R_2}{R_1} I_{PD} R_1 = -R_2 I_{PD} \quad (4.1)$$

The capacitor C_1 is used to limit the high frequency noise.

The Stage B is an inverter with amplification factor -1 whose task it to change the sign of the signal, according to:

$$V_0^B = -\frac{R_4}{R_3} V_0^A = -1 \cdot V_0^A = +R_2 I_{PD} \quad (4.2)$$

Finally, the Stage C is the output buffer that sets the output impedance of the amplifier at low level. In our case we have chosen the DC voltage follower configuration which provides the circuit an output impedance of about 0,75 Ω [102].

The output signal of the voltage follower, which is also the output of the whole circuit, is not changed, so we have:

$$V_{out} = V_o^C = +R_2 I_{PD} \quad (4.3)$$

Therefore the voltage signal at the output of the photodiode amplifier is proportional to the photocurrent and the amplification factor is exactly the value of the resistor R_2 .

In our circuit we have used the value $R_2=50K$ which corresponds to conversion from input photocurrent to output voltage of $20 \mu A \rightarrow 1 V$. We have illuminated the photodiode and measured with an amperometer in series to the photodiode [105] the value of $18.5 \mu A$ for corresponding output of 1 V. This can be acceptable within the experimental tolerance.

4.5 Optical arrangement for mode matching of the laser beam with the interferometer

The design of the AO system that we have presented in the previous Chapter is based on several assumptions that need to be strictly satisfied in our

experimental prototype if we want to perform a good and reliable characterization.

One of the most important requirements that the setup must fulfil is that the laser beam is correctly matched with the interferometer and in particular with the deformable mirror and with the pixellated photodiode.

In fact, the laser beam diameter at the plane of the adaptive mirror must be small compared with the diameter of the deformable membrane in order to avoid non linearity effects that are more evident in the boundary region where the membrane is bonded. But, in the same time the laser spot needs to be large enough for aberrations like astigmatism which would not be effectively corrected if the beam was strongly focused around the axis.

Furthermore, in our model the analysis of the Gaussian beam perturbation has been carried out on the waist plane which must coincide with the plane of the photodiodes array. Here the waist must also fulfil the condition $1.4 < w_0/L < 1.6$ (L = length of the single pixel) for a good decoupling of the 6 degrees of freedom.

The problem of controlling position and diameter of the beam waist in Gaussian Optics is commonly named *mode matching* and can be solved using a thin lens and the ABCD law for light propagation [95]. The Gaussian beam propagation follows the ABCD law in paraxial approximation as:

$$q_2 = \frac{Aq_1 + B}{Cq_1 + D} \quad (4.4)$$

in analogy with spherical waves, where the curvature radius R is now replaced by the complex parameter q .

Using the ABCD matrix of the thin lens of focal length f , the complex parameter q_1 at the input transforms into the parameter q_2 at output according to:

$$\frac{1}{q_2} = \frac{1}{q_1} - \frac{1}{f} \quad (4.5)$$

If q_1 and q_2 are respectively at distances d_1 and d_2 from the lens, as pictured in figure 4.17, the relationship between them is given by:

$$q_2 = \frac{\left(1 - \frac{d_1}{f}\right)q_1 + \left(d_1 + d_2 - \frac{d_1 d_2}{f}\right)}{-\frac{1}{f}q_1 + \left(1 - \frac{d_1}{f}\right)} \quad (4.6)$$

as can be seen using the ABCD matrix of the system made by the sequence of distance d_1 , thin lens f and distance d_2 .

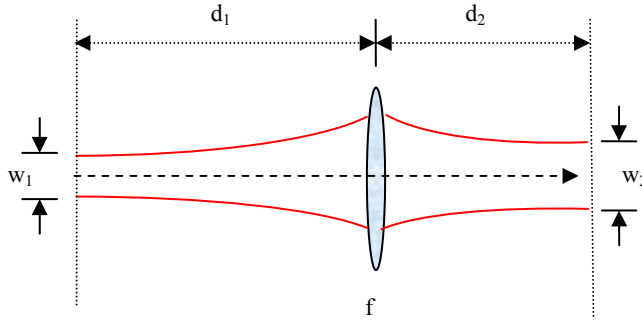


Figure 4.17: schematic of the Gaussian beam propagation through the thin lens

The input beam of initial waist w_1 , after passing through the thin lens at distance d_1 , is focused into the new waist w_2 at distance d_2 . We can note that the behaviour is similar to that observed for a spherical wave in the geometrical paraxial approximation. In fact, in that case the light emerging from a point like source at distance d_1 is focused by the thin lens into an image point at distance d_2 according to the law of conjugate points. In Gaussian optics the ideal point of focalization is replaced by a finite size spot as the transverse dimension of the Gaussian beam cannot ever collapse into a null size geometrical point. So the law of the conjugate points is modified into:

$$\left(1 - \frac{d_2}{f}\right) = \frac{1 - \frac{d_1}{f}}{\left(1 - \frac{d_1}{f}\right)^2 + \left(\frac{\pi w_1^2}{\lambda f}\right)^2} \quad (4.7)$$

which provides that the distance of the image d_2 never diverges to infinite. It is worth noting that eq. (4.7) reduces to the law of conjugate points in

geometrical optics if $w_l \rightarrow 0$. The difference between geometrical optics and Gaussian optics is well represented in figure 4.18, where we picture the law of conjugate points of the thin lens for geometrical optics and for Gaussian optics.

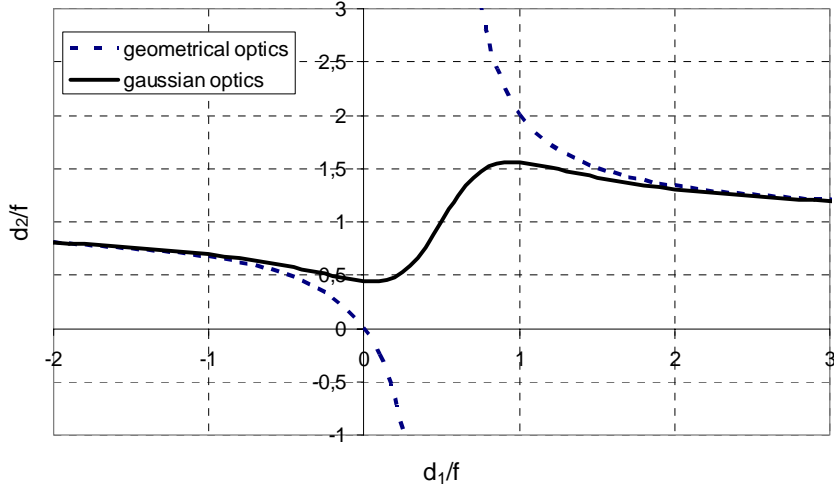


Figure 4.18: law of conjugate points of the thin lens for geometrical optics (dashed blue line) and for Gaussian optics (continue black line).

Hence, if we assume that at distances d_1 and d_2 the beam waists have flat wavefront, it holds:

$$q_1 = j \frac{\pi w_1^2}{\lambda} \quad ; \quad q_2 = j \frac{\pi w_2^2}{\lambda} \quad (4.8)$$

that, substituted into eq. (4.6), gives the following two equations from the real and the imaginary part respectively:

$$(d_1 - f)(d_2 - f) = f^2 - f_0^2 \quad (4.9)$$

and

$$\frac{d_1 - f}{d_2 - f} = \frac{w_1^2}{w_2^2} \quad (4.10)$$

being f_0 the coherence length:

$$f_0 = \frac{\pi w_1 w_2}{\lambda} \quad (4.11)$$

By combining eq. (4.9) and eq. (4.10), we can derive:

$$\begin{cases} d_1 = f \pm \frac{w_1}{w_2} \sqrt{f^2 - f_0^2} \\ d_2 = f \pm \frac{w_2}{w_1} \sqrt{f^2 - f_0^2} \end{cases} \quad (4.12)$$

where plus or minus signs can be alternatively used.

This means that, if we fix the desired ratio w_2/w_1 and choose the suitable lens with $f > f_0$, we can calculate the distances d_1 and d_2 where the beam waists are formed.

We have used these two final equations for the arrangement of the experimental setup, in order to match the beam waist of the input laser to the plane of the deformable mirror and successively to the plane of the pixellated photodiodes. In particular, as we had to match twice the beam, we have considered the more complicated optical structure shown in the figure below.

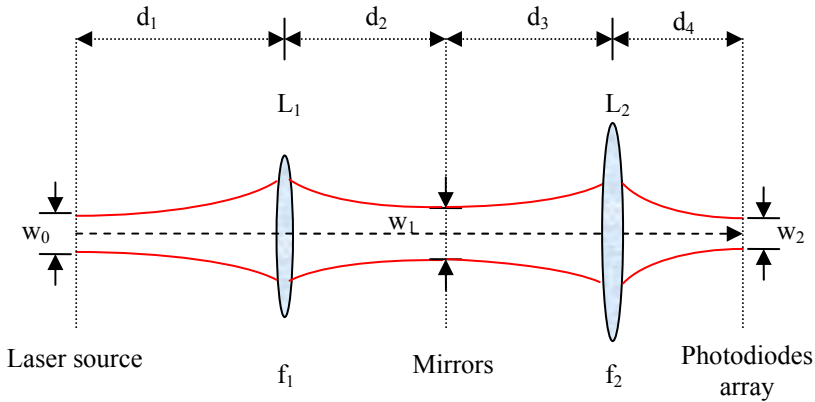


Figure 4.19: schematic of the optical system based on two thin lenses used in our experimental prototype. The lens L_1 matches the input beam waist w_0 with the beam waist w_1 on the adaptive mirror plane, while the lens L_2 matches the beam waist w_1 to the waist w_2 on the plane of the photodiodes array.

With reference to the experimental setup schematized in figure 4.1, the first distance d_1 corresponds to the path from the initial waist position to the lens L_1 ; the distance d_2 corresponds to the path between L_1 and the mirrors (the optical path is the same for the adaptive and the piezo mirror). The waist w_1 at the deformable mirror is chosen equal to 3 mm so the laser spot of diameter $2w_1=6\text{ mm}$ covers completely the central electrode and half of the first ring of lateral actuators and in the same time it is small enough with respect to the membrane diameter of 30 mm .

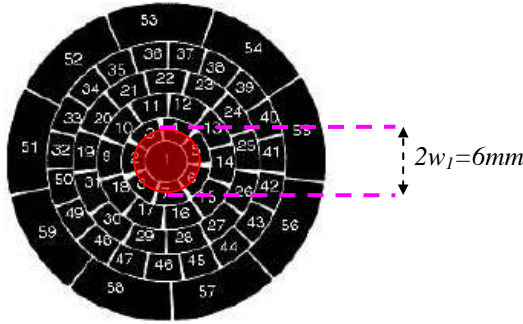


Figure 4.20: mode matching of the laser beam with the deformable mirror. The spot covers the central electrode and half of the first ring of lateral electrodes.

The distance d_3 of figure 4.19 corresponds to the path that each of the two half beams runs from the mirror to the lens L_2 separated by distance d_4 from the pixellated photodiode. Here the two beams interfere and form the waist w_2 which must comply with the requirement $1.4 < w_2/L < 1.6$, being $L=1.3\text{ mm}$ the length of one pixel. We have chosen $w_2=2\text{ mm}$, so $w_2/L=1.54$ and the spot $2w_2=4\text{ mm}$ covers the central pixel and part of the first pixels around.

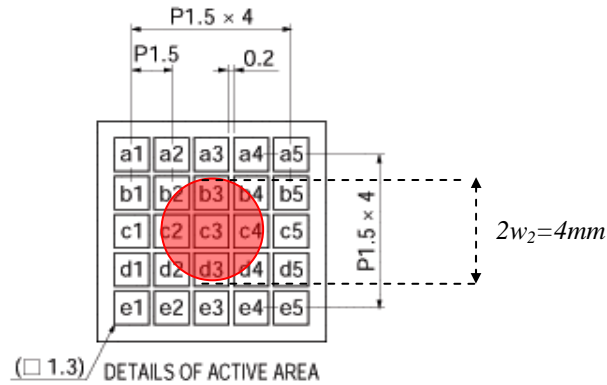


Figure 4.21: mode matching of the laser beam with the pixellated array of photodiodes

4.6 Data processor

The digital signal processing of the data collected by the ADC is made of several operations foreseen by the design of the control system (figures 3.9 and 3.10) and necessary to generate correction signals for the actuators. In figure 4.22 we show the scheme of the operations that we need to carry out using the data processor for the lock in control and for the adaptive wavefront correction.

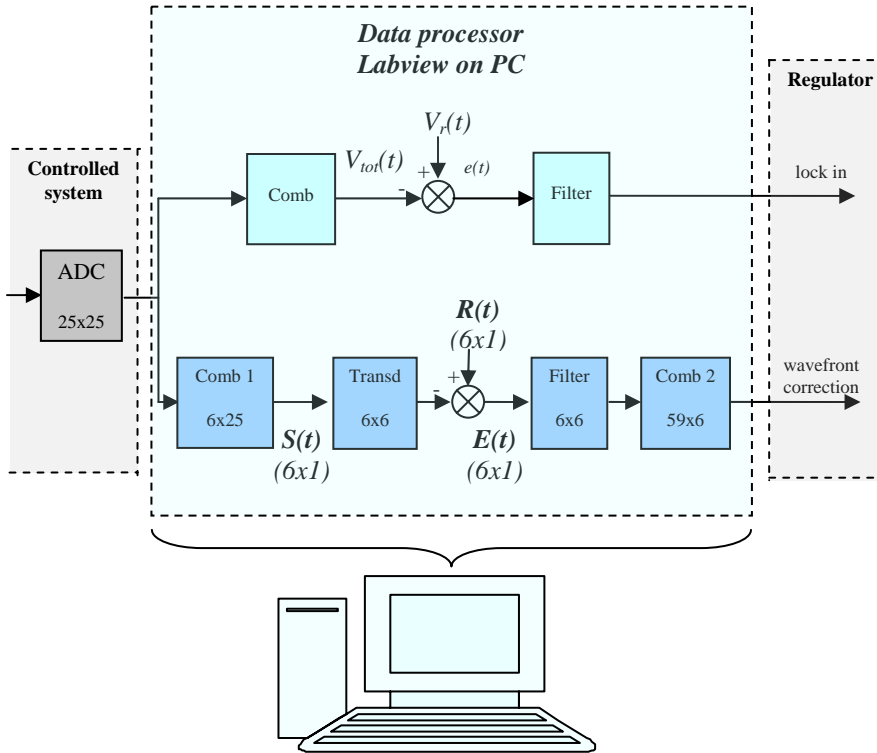


Figure 4.22: block diagram of the data processor implemented on Labview programmed PC

We have performed the data processing unit using the Labview Virtual Instrument properly designed on a standard PC [106], [107].

In fact, Labview is a graphical programming language that permits to create block diagrams of Virtual Instruments and execute lots of operations on digital signals. A front panel can be created as user/machine interface where we can manipulate the parameters of the Virtual Instruments as if we were

using real physical instruments. We can operate the Virtual Instrument through knobs, pushbuttons, dials and other input devices, and we can see indicators such as graphs, leds and other displays.

In our Prototype we have simulated the blocks corresponding to the combinatorics using the transfer matrices designed in Chapter 3, while low pass filters at 0.1 Hz have been chosen as correcting networks for the stability of the controls.

In the following two figures we show two examples respectively of the block diagram and of the front panel that we have used in our work.

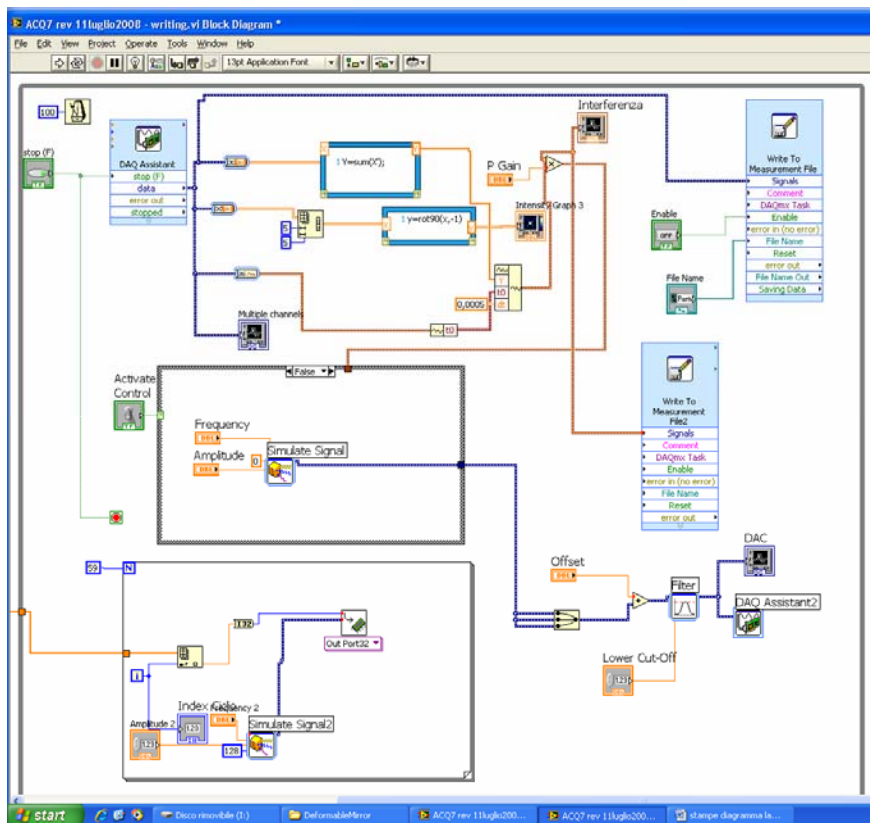


Figure 4.23: block diagram of the Virtual Instrument simulated on Labview to perform the required operations of the data processor. The blocks and the data flow are properly designed in compliance with the scheme of fig. 4.22

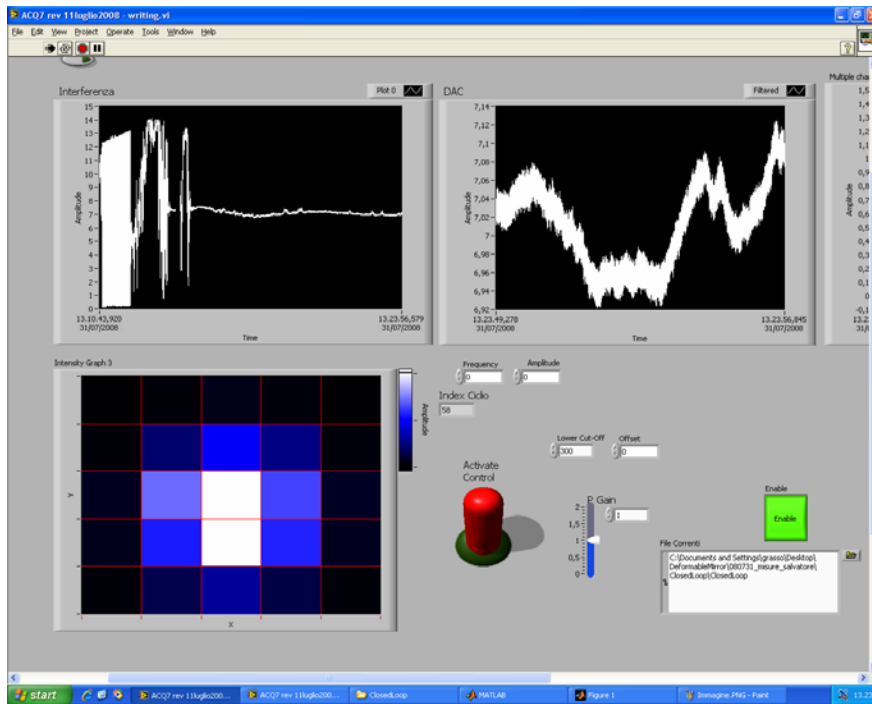


Figure 4.24: front panel of the Virtual Instrument. In the dials on the top we can see the transient of the interference signal that is reaching the regime stationary condition (left side) thanks to the lock in carried out by the driver signal (right side). In the bottom, on the left the 5x5 coloured matrix that simulates the array of photodiodes (the colour changes from black to white for increasing intensity on the photodiode). On the right side we can see some indicators and the red lever that we use to activate the control.

Chapter 5

Test of the prototype, results and discussion

So far we have presented the Project of the AO system for the correction of laser beam jitters in interferometric GW detectors. In particular, starting from the presentation of the Virgo Experiment and after investigating the state of the art of the available AO technology, we have developed the design of a new AO system where the phase front reconstruction is performed using an interferometric technique more sensitive and faster than the usual Shack Hartmann sensor. Successively, we have described the arrangement of the experimental Prototype implemented in our laboratory to perform the simultaneous control of six aberration modes of the laser wavefront in compliance with the design statements.

In this final Chapter we report the tests we have carried out for the characterization of the Prototype and the results obtained for the validation of the Project. Our goal is to check effectiveness and stability of the control in the band up to 1 *kHz* and to demonstrate that our AO system fulfils the requirements for laser noise reduction in the Virgo antenna.

We have performed several measurements and all the data that we here present are statistically processed and reported in form of graphs, curves, surfaces, tables and histograms in such a way to provide the reader a good understanding of the behaviour and the performances of the system in comparison with the theoretical prediction.

The measurements are divided into three groups and for each one we provide a short remind about the theoretical aspects and the methodology followed for their execution.

First of all we have characterized the two control systems implemented respectively for the lock in of the interferometer and for the adaptive correction of the perturbed wavefront. To do that, we have measured the frequency response functions and here report the Bode diagrams of modulus and phase which give us information about bandwidth and stability.

Secondly, we have measured the coefficients of the aberration modes under the condition of open loop and of closed loop control. The curves of such coefficients in the time domain give evidence of the strong reduction of the RMS values when the loop is closed. The same data converted in spectral curves demonstrate that the residual noise is significantly reduced in the

region of low frequency below 200 Hz, in good accordance with the Virgo requirements.

The third set of measurements is the laser beam quality control that we have performed to check whether our AO system is really able to clean up the jitters due to first and second order Hermite Gauss terms perturbing the fundamental Gaussian mode. In particular, we show that when we close the loop of the AO control the total intensity profile of the two beams interfering at the photodiodes array matches with good precision the ideal Gaussian curve that is expected on the interference plane of two unperturbed laser beams. This result gives us direct evidence of the jitters suppression operated by our AO system.

5.1 Measurement of the frequency response function of the control system

We briefly remind the basic theoretical principles for the characterization of control systems and explain the experimental methodology that we used to test our Prototype.

Then, we present the measurements and discuss the results achieved for the lock in of the interferometer and for the AO control that has been implemented to simultaneously correct six aberration modes of the laser beam.

5.1.1 Some theoretical principles

The study of control systems is based on the use of dynamical mathematical models that usually are considered linear within a certain range of variation of the variables [96].

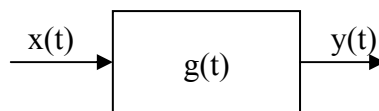


Figure 5.1: block diagram of a system with input variable $x(t)$, output variable $y(t)$ and pulse response $g(t)$

In figure 5.1 we see that a linear stationary system is generally an operator that transforms the input signal $x(t)$ into the output signal $y(t)$ according to a specific law obtained by solving the differential equation of type:

$$a_n \frac{d^n y}{dt^n} + a_{n-1} \frac{d^{n-1} y}{dt^{n-1}} + \dots + a_0 y = b_m \frac{d^m x}{dt^m} + b_{m-1} \frac{d^{m-1} x}{dt^{m-1}} + \dots + b_0 x \quad (5.1)$$

where the coefficients a_n and b_m are constants and $n \geq m$.

In order to characterize the system in the time domain, we need to analytically solve that differential equation and thus obtain the dependence of $y(t)$ on $x(t)$. In particular, if we know the response $g(t)$ of the system to the Dirac pulse function $\delta(t)$, we have all the necessary information as each input signal transforms into output through the following integral of convolution:

$$y(t) = \int_0^{\infty} g(t') x(t - t') dt' \quad (5.2)$$

On the other hand, as the analytical solution of the differential equation (5.1) is quite difficult to calculate except for simple cases, it is common to study dynamical systems using the method of the Laplace transform. This is an operator associating any function $f(t)$ defined in the time domain of variable t to the corresponding complex function $F(s)$ defined in the domain of variable $s = \sigma + j\omega$, according to:

$$\left\{ \begin{array}{l} F(s) = \int_0^{\infty} f(t) e^{-st} dt \\ f(t) = \frac{1}{2\pi j} \int_{\sigma_0 - j\infty}^{\sigma_0 + j\infty} F(s) e^{st} ds \end{array} \right. \quad (5.3)$$

The method of Laplace is very useful because it allows to transform the differential equation (5.1) into the simple algebraic equation:

$$Y(s) = G(s)X(s) \quad (5.4)$$

where $X(s)$ and $Y(s)$ are Laplace transforms of $x(t)$ and $y(t)$ respectively, and :

$$G(s) = \frac{Y(s)}{X(s)} = \frac{\sum_{i=0}^m b_i s^i}{\sum_{i=0}^n a_i s^i} \quad (5.5)$$

is the *transfer function* of the system, expressed in form of ratio between two polynomials of variable s given by the application of the Laplace operator to the two terms of eq. (5.1). This last result, which holds when the system is initially quiet, allows to calculate the Laplace transform $Y(s)$ by the product of $X(s)$ times $G(s)$ and then to obtain the signal $y(t)$ by the inverse transform operator indicated in the second row of eq. (5.3).

The transfer function $G(s)$ is the Laplace transform of the pulse response $g(t)$ and permits to calculate the system response $Y(s)$ to any input $X(s)$. Hence, the system dynamics is completely characterized from $g(t)$ in the time domain or alternatively from $G(s)$ in the Laplace domain.

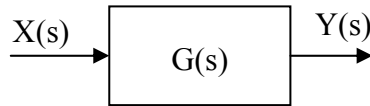


Figure 5.2: block diagram of a system represented in the complex domain of Laplace. $X(s)$ is the input signal, $Y(s)$ the output signal and $G(s)$ is the transfer function.

The dynamical behaviour of any system depends on the number and the kind of poles of $G(s)$, or the zeros of the equation:

$$\sum_{i=0}^n a_i s^i = 0 \quad (5.6)$$

In particular, if eq. (5.6) has only real solutions then the system is of the first order and it responds to an instantaneous variation of the input signal with the typical delay time τ before reaching the stationary regime. In the case of complex conjugate solutions with negative real part, the system is of the second order and its response to an instantaneous variation of the input signal is characterized by the rise time τ and several damped oscillations before reaching the stationary state. This kind of second order system is stable and has proper frequency ω_n and damping coefficient δ . On the contrary, if the real part of the complex conjugate poles is positive, the oscillations increase

and the output signal diverges. In this case the system is unstable and do not ever reach the stationary regime.

Figure 5.3 shows typical step responses of first and second order systems.

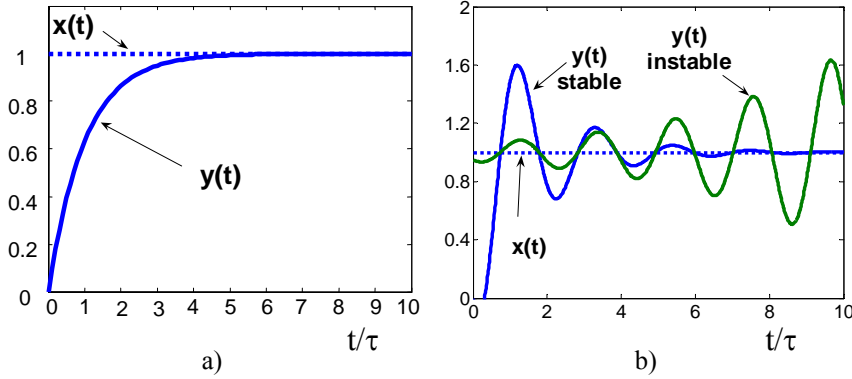


Figure 5.3: typical step response $y(t)$ of a system of the first order a) and of the second order b) in case of stability and of instability. The x axis is the time t normalized to the characteristic rise time τ .

Stationary linear systems can be also described using the Fourier representation based on the study of the *frequency response function* $G(j\omega)$ given by the transfer function $G(s)$ when $s=j\omega$ and related to the pulse response $g(t)$ through the Fourier transform operator:

$$G(j\omega) = \int_0^{\infty} g(t)e^{-j\omega t} dt \quad (5.7)$$

$$g(t) = \frac{1}{2\pi} \int_{-\infty}^{\infty} G(j\omega)e^{j\omega t} d\omega$$

In fact, we can represent any system using the frequency response function that converts the Fourier transform of the input signal $X(\omega)$ into the Fourier transform of the output signal $Y(\omega)$ according to:

$$Y(\omega) = |G(j\omega)|e^{j\varphi(\omega)}X(\omega) \quad (5.8)$$

In this last equation we have remarked that $G(j\omega)$ is a complex function that introduces the phase difference $\varphi(\omega)$ between input and output.

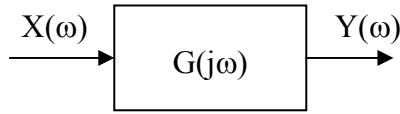


Figure 5.4: block diagram of a system represented in the Fourier domain. $X(\omega)$ is the input signal, $Y(\omega)$ the output signal and $G(j\omega)$ is frequency response function.

The Fourier representation is often preferred because it can be experimentally tested by direct measurements of the frequency response function.

The most popular method to represent $G(j\omega)$ is the *Bode diagram* composed of two graphs named respectively *amplitude diagram* α and *phase diagram* β . The first one is the logarithm of $G(j\omega)$ modulus plotted against the logarithm of ω and the second one is the phase $\varphi(\omega)$ against the logarithm of ω . In the following figure we show typical Bode diagrams for a system of the first order and for a stable system of the second order. The scale is logarithmic for the α diagram and half logarithmic for β .

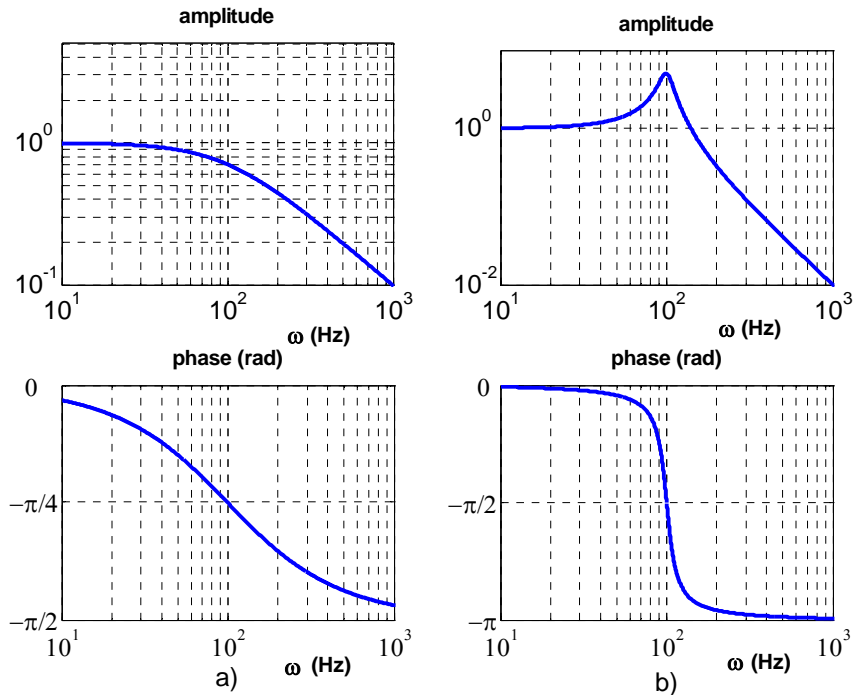


Figure 5.5: Bode diagram of a system a) of the first order (cut off frequency 100 Hz) and b) of the second order (proper frequency 100 Hz, damping coefficient 0.1)

The amplitude can also be plotted in half logarithmic scale in terms of decibel (dB) given by $20 \log_{10} |G(j\omega)|$ as scale unit on the y axis.

The most relevant parameter of the first order system is the bandwidth measured from zero up to the higher cut off frequency $\omega_H = 1/\tau$ where the α diagram drops down to $1/\sqrt{2}$ of its static value corresponding to $-3dB$.

In second order systems we notice the resonance frequency ω_n where the amplitude exhibits a peak whose shape depends on the damping term δ .

The models so far discussed can be applied to describe all the linear systems including the closed loop controls that are of particular interest in our work. Therefore, using the same formalism, we schematize the feedback control of figure 5.6 where we assume that the transducer is 1.

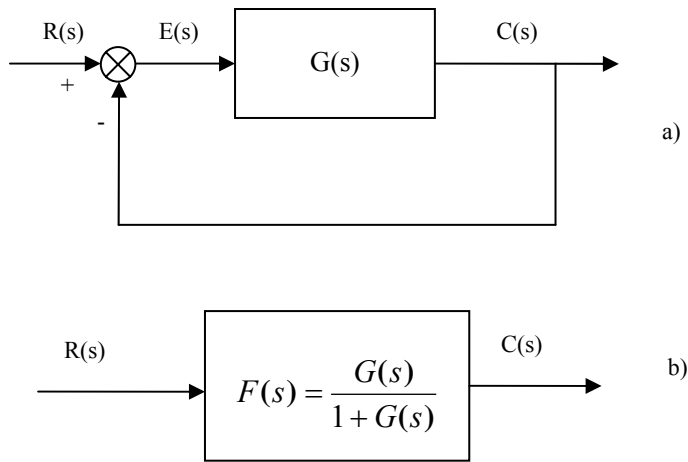


Figure 5.6: block diagram of the feedback control system a) and synthetic representation b). The transducer is assumed to be unitary.

In this case we have to deal with two different transfer functions that are $G(s)$ for open loop and $F(s) = G(s)/[1 + G(s)]$ for closed loop system.

The characterization of that control is based on information about the following three aspects:

1. Robustness and effectiveness
2. Response time and bandwidth
3. Stability

The system robustness against disturbances, non linearity effects and parameters variation is proportional to the amplitude of the open loop gain G

in the bandwidth of interest. This means that if the condition $|G(j\omega)| \gg 1$ is fulfilled, the feedback system is robust and effective in maintaining the controlled system on the working point set by the reference signal.

Response time and bandwidth at closed loop concern the system capability to follow fast reference signal variations. As the closed loop system is DC coupled, the bandwidth of $F(j\omega)$ is defined from zero to -3dB cut off frequency.

Stability indicates the system aptitude to reach the regime state after the excitation induced by the input signal. In feedback control systems the stability is estimated using the Nyquist criterion that involves the analysis of the frequency response of the open loop gain $G(j\omega)$. In particular, two parameters are defined, named *stability margins*, which measure the quality of the dynamical behaviour of the closed loop control system. The *amplitude margin* M_A is the inverse of the modulus $|G(j\omega)|$ calculated in the frequency ω where the phase is $\varphi(\omega) = -\pi$. The *phase margin* M_{PH} is the angle that it is necessary to subtract to $\varphi(\omega)$ calculated in the frequency ω where the modulus is 1, to reach the value $-\pi$. Typical values for the stability of the closed loop system are M_A from 4 to 6 (from 12 dB to 16 dB) and M_{PH} from 45° to 60° (from 0.78 rad to 1.05 rad).

In conclusion, a closed loop control system is completely characterized if all the parameters here discussed are known. Therefore, in order to test our experimental Prototype, we have carried out measurements of the frequency response function at open loop and at closed loop. From the open loop gain we get information about robustness, effectiveness and stability, while from the closed loop response we measure the bandwidth of feedback control.

5.1.2 Methodology of measurement

The measurement of frequency response functions has been operated using the Virtual Spectrum Analyzer implemented on Labview. This instrument generates the oscillating sinusoidal signal at variable frequency that is introduced into the system under test and in the same time it measures and processes the system output. So it is possible to reconstruct the amplitude and phase diagram of the system frequency response over the whole spectral range from 0 to ∞ .

The process of measurement implemented on the Virtual Analyzer is shown in the block diagram of figure 5.7.

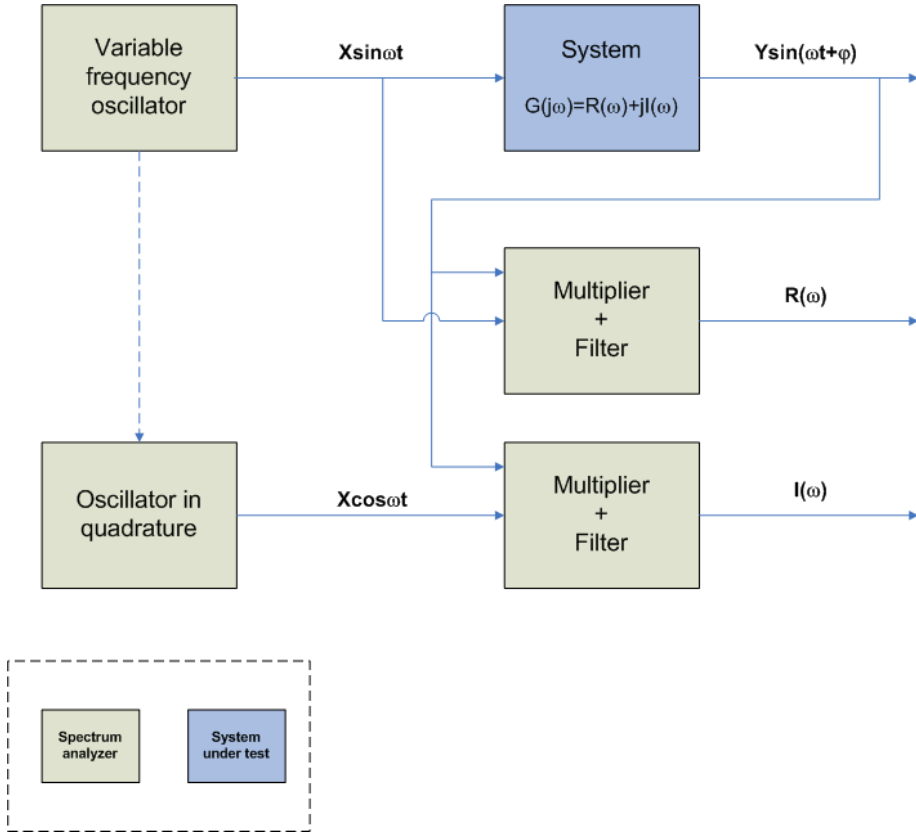


Figure 5.7: block diagram of the process implemented on the Virtual Spectrum Analyzer for the measurement of frequency response functions

The variable frequency oscillator generates the signal $X\sin\omega t$ that is introduced into the system under test. The output of the system is the sinusoidal signal of amplitude Y and phase difference φ given by:

$$Y \sin(\omega t + \varphi) = Y(\sin \omega t \cos \varphi + \cos \omega t \sin \varphi) \quad (5.9)$$

That output is reintroduced into two multipliers where it is respectively multiplied times the input signal and its derivative, giving:

$$\begin{cases} z_1(t) = XY(\sin^2 \omega t \cos \varphi + \sin \omega t \cos \omega t \sin \varphi) \\ z_2(t) = XY(\cos^2 \omega t \sin \varphi + \sin \omega t \cos \omega t \sin \varphi) \end{cases} \quad (5.10)$$

Successively, these two signals $z_1(t)$ and $z_2(t)$ are integrated over m times the period $T=2\pi/\omega$:

$$\left\{ \begin{array}{l} \frac{1}{mT} \int_{-\frac{T}{2}}^{+\frac{T}{2}} z_1(t) dt = \frac{XY}{2} \cos \varphi = \frac{X^2}{2} R(\omega) \\ \frac{1}{mT} \int_{-\frac{T}{2}}^{+\frac{T}{2}} z_2(t) dt = \frac{XY}{2} \sin \varphi = \frac{X^2}{2} I(\omega) \end{array} \right. \quad (5.11)$$

and finally by the product with the term $2/X^2$ we achieve real part $R(\omega)$ and imaginary part $I(\omega)$ of $G(j\omega)$.

These are used to calculate amplitude and phase of the Bode diagrams.

5.1.3 Results and discussion

5.1.3.1 Frequency response function of the lock in control system

We have initially measured the frequency response at open loop and at closed loop of the feedback control implemented with the piezo electric mirror to lock the interferometer on the middle fringe working point.

The following figures report the amplitude and phase Bode diagrams of the measured $G(j\omega)$ and $F(j\omega)$.

Piezo Open loop

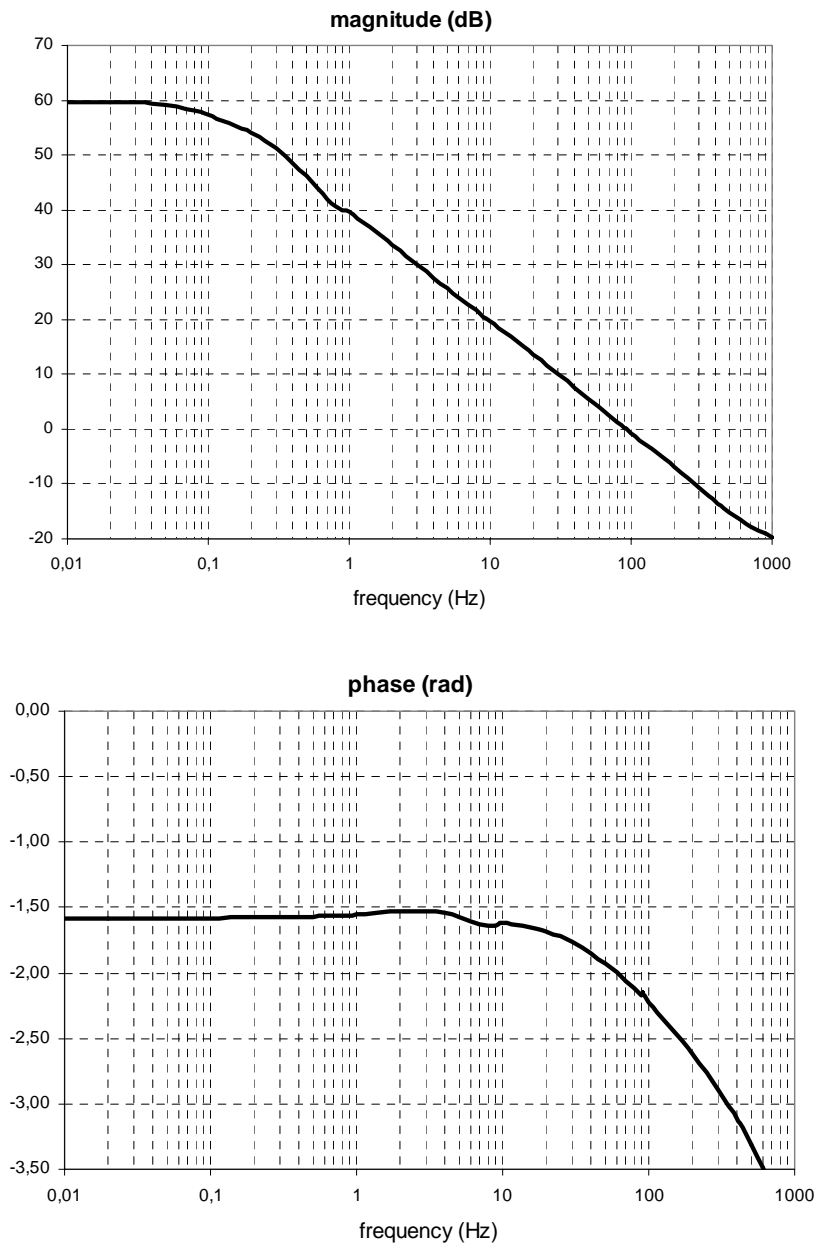


Figure 5.8: Bode diagram of the frequency response function $G(j\omega)$ of the piezo control at open loop

Piezo Closed loop

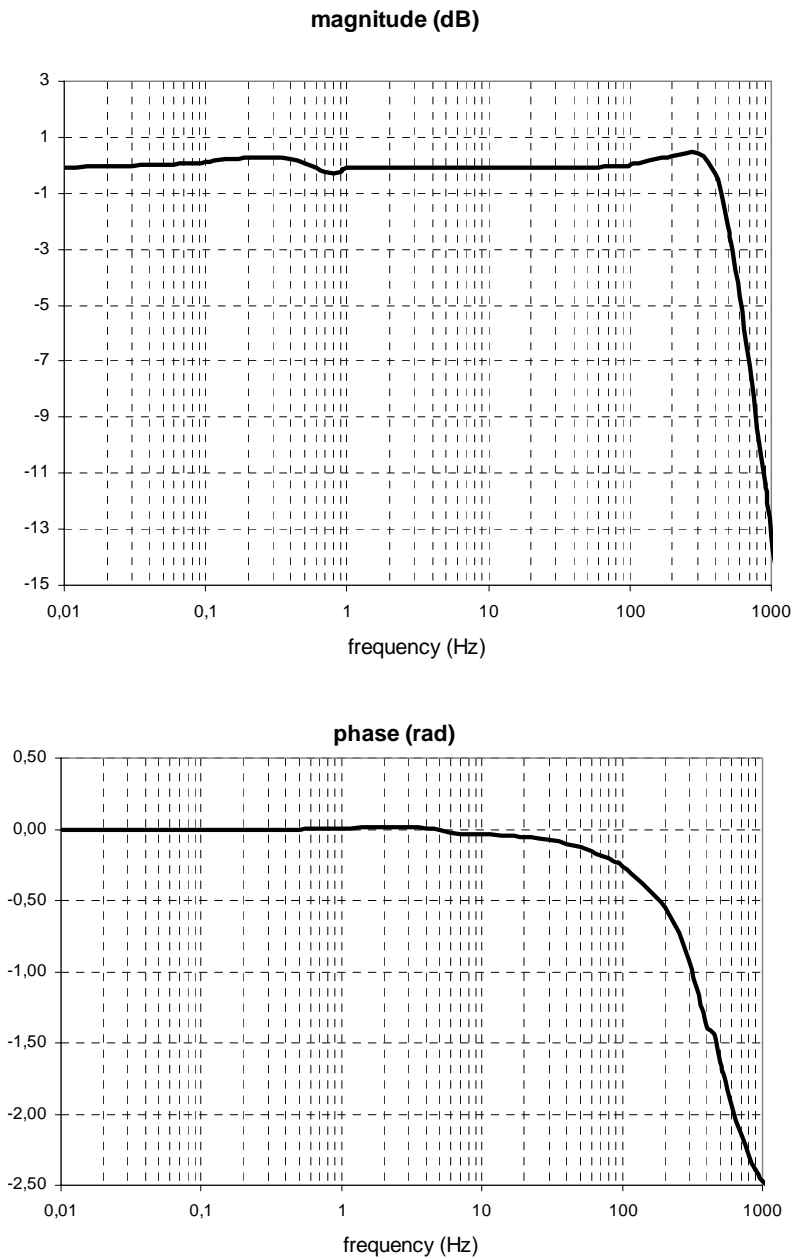


Figure 5.9: Bode diagram of the frequency response function $F(j\omega)$ of the piezo control at closed loop

From figure 5.8, which reports the frequency response function $G(j\omega)$ of the piezo control system at open loop, we see that the static gain measured at 0.01 Hz is 60 dB (corresponding to 10^3) and that it decreases to 0 dB (or 1) at 91 Hz. This last is the so called *unitary gain frequency* or the upper limit for robustness and effectiveness of the control.

The Bode diagram relative to the open loop frequency response gives also information about the stability. In fact, the amplitude margin is 13.8 dB and the phase margin is 0.99 rad and therefore from the Nyquist theorem we can affirm that the system is stable.

From figure 5.9, we see that the closed loop control exhibits the dynamical behaviour similar to second order systems with resonance frequency at 450 Hz and bandwidth of 535 Hz.

5.1.3.2 Frequency response functions of the AO control system

The piezo control has been used only in the first step of our experiment to lock the interferometer and operate the procedure of diagonalization of the deformable mirror transfer matrix.

After that, the piezo actuator has been switched off and simply used as static flat mirror in one of the two arms of the Michelson.

On the contrary, the adaptive control has been put into operation to perform wavefront correction using the deformable mirror placed in the second arm of the interferometer.

Thanks to the diagonalization which allows to consider the six degrees of freedom decoupled one with another, we have independently measured the frequency responses g_{ii} , $i=1,...,6$ (see eq. (3.75)) of the single controls acting at open loop respectively on longitudinal mode, TiltX, TiltY, Astigm45, Astigm90 and Defocus and the frequency responses f_{ii} , $i=1,...,6$ (see eq. (3.76)) of the same controls at closed loop.

The set of 12 Bode diagrams that we present in the following gives the complete characterization of our AO control.

Longitudinal Open loop

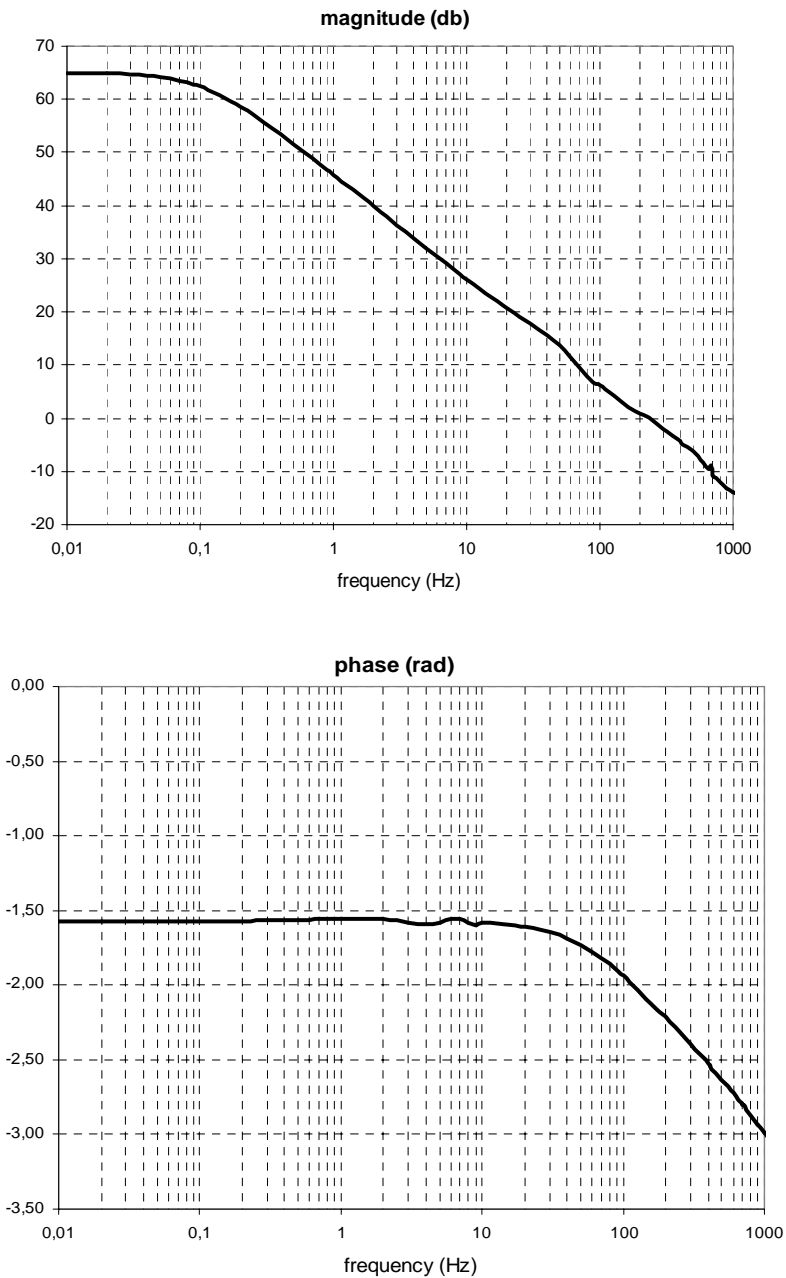


Figure 5.10: Bode diagram of the frequency response function $g_{11}(j\omega)$ of the longitudinal control at open loop

Longitudinal Closed loop

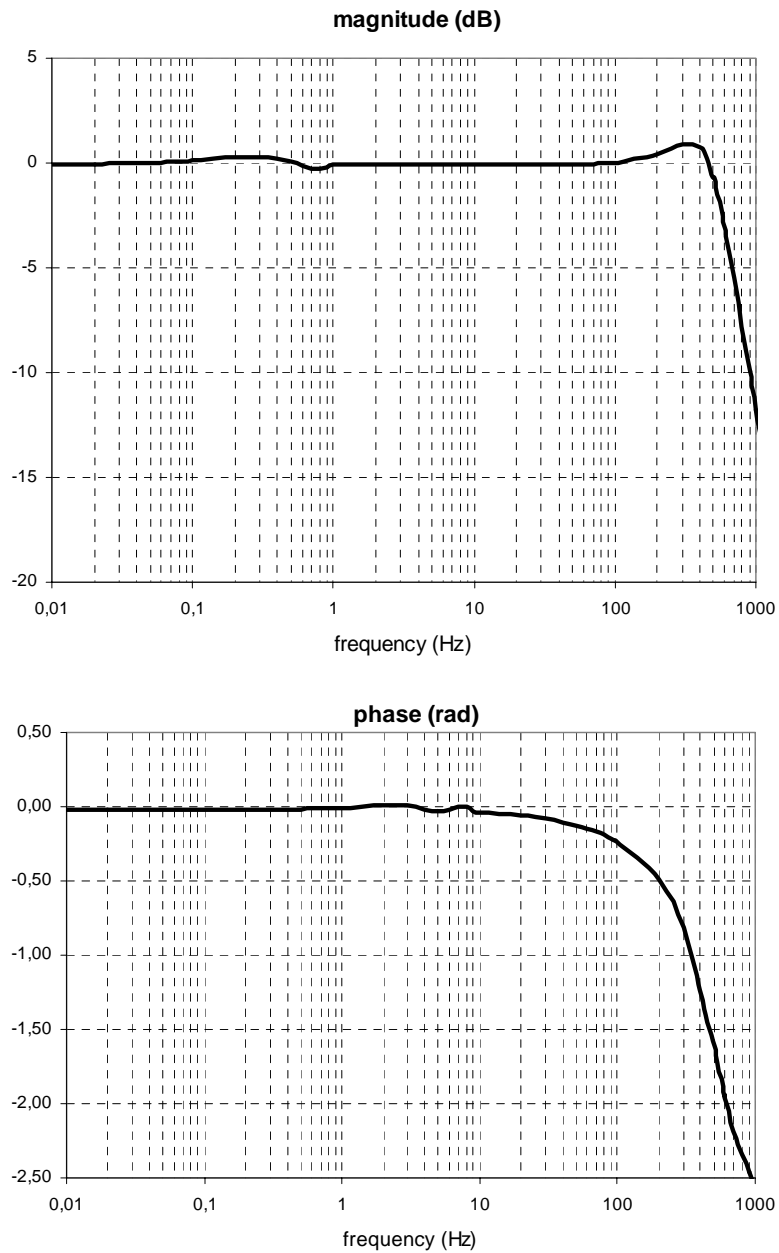


Figure 5.11: Bode diagram of the frequency response function $f_{11}(j\omega)$ of the longitudinal control at closed loop

TiltX Open loop

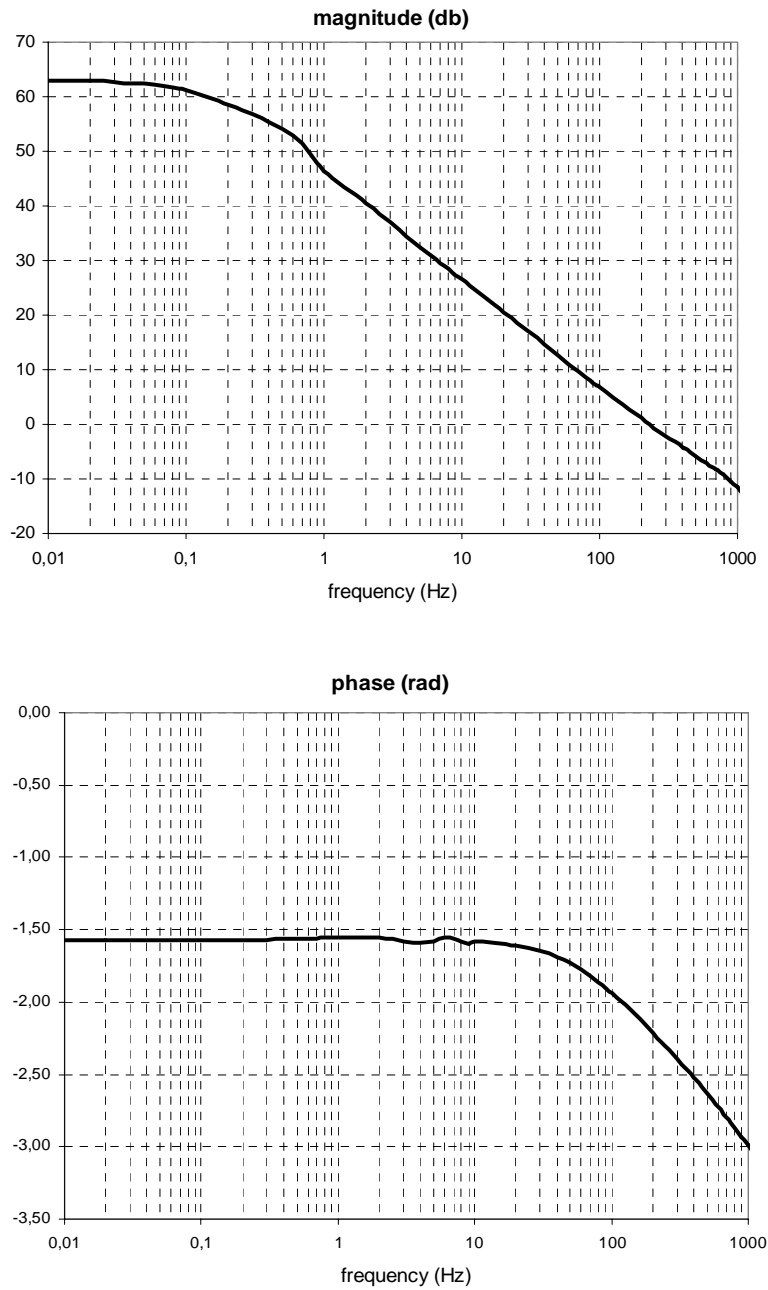


Figure 5.12: Bode diagram of the frequency response function $g_{22}(j\omega)$ of the TiltX control at open loop

TiltX Closed loop

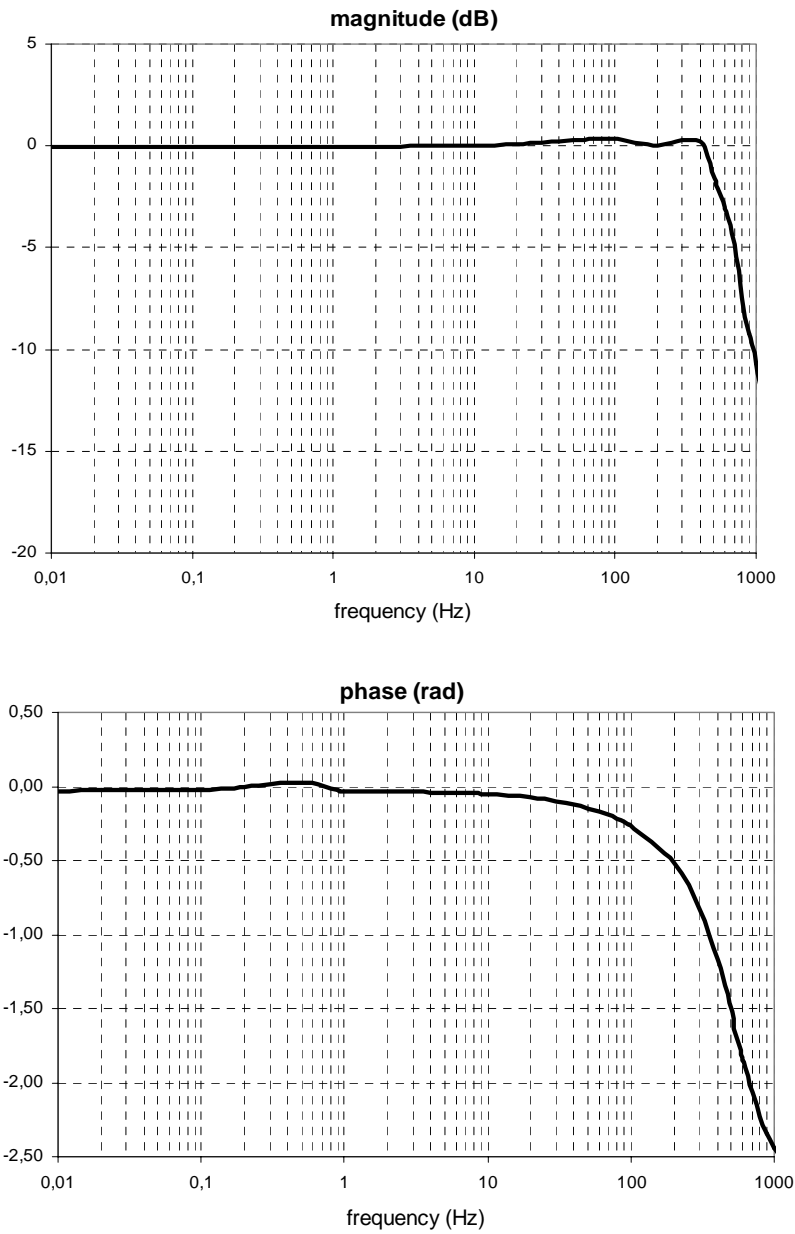


Figure 5.13: Bode diagram of the frequency response function $f_{22}(j\omega)$ of the TiltX control at closed loop

TiltY Open loop

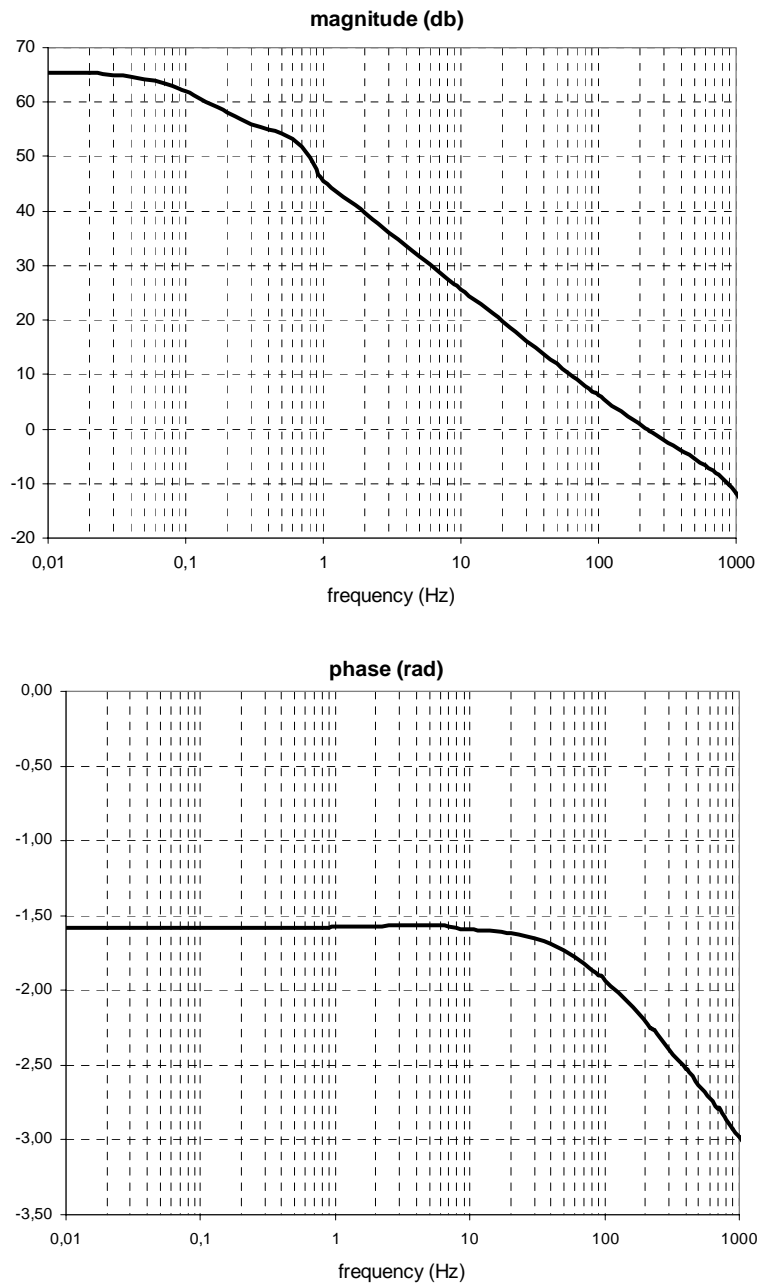


Figure 5.14: Bode diagram of the frequency response function $g_{33}(j\omega)$ of the TiltY control at open loop

TiltY Closed loop

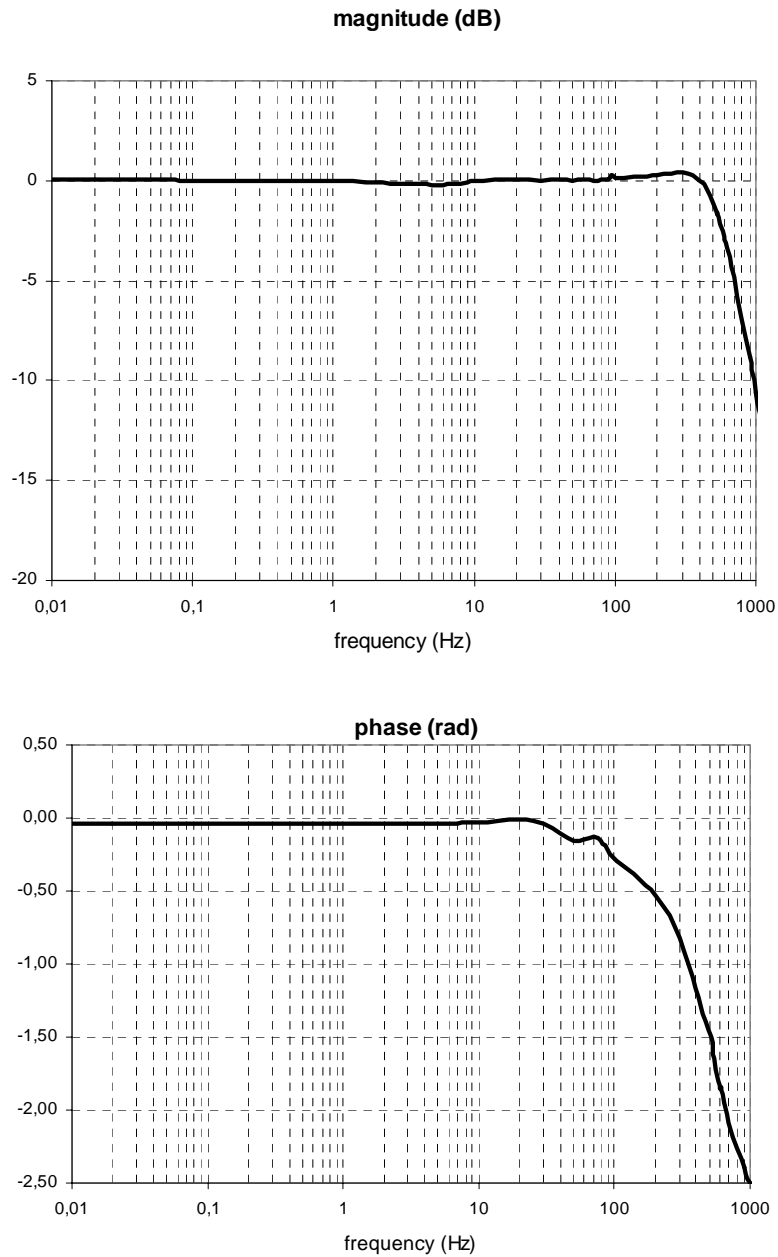


Figure 5.15: Bode diagram of the frequency response function $f_{33}(j\omega)$ of the TiltY control at closed loop

Astig45 Open loop

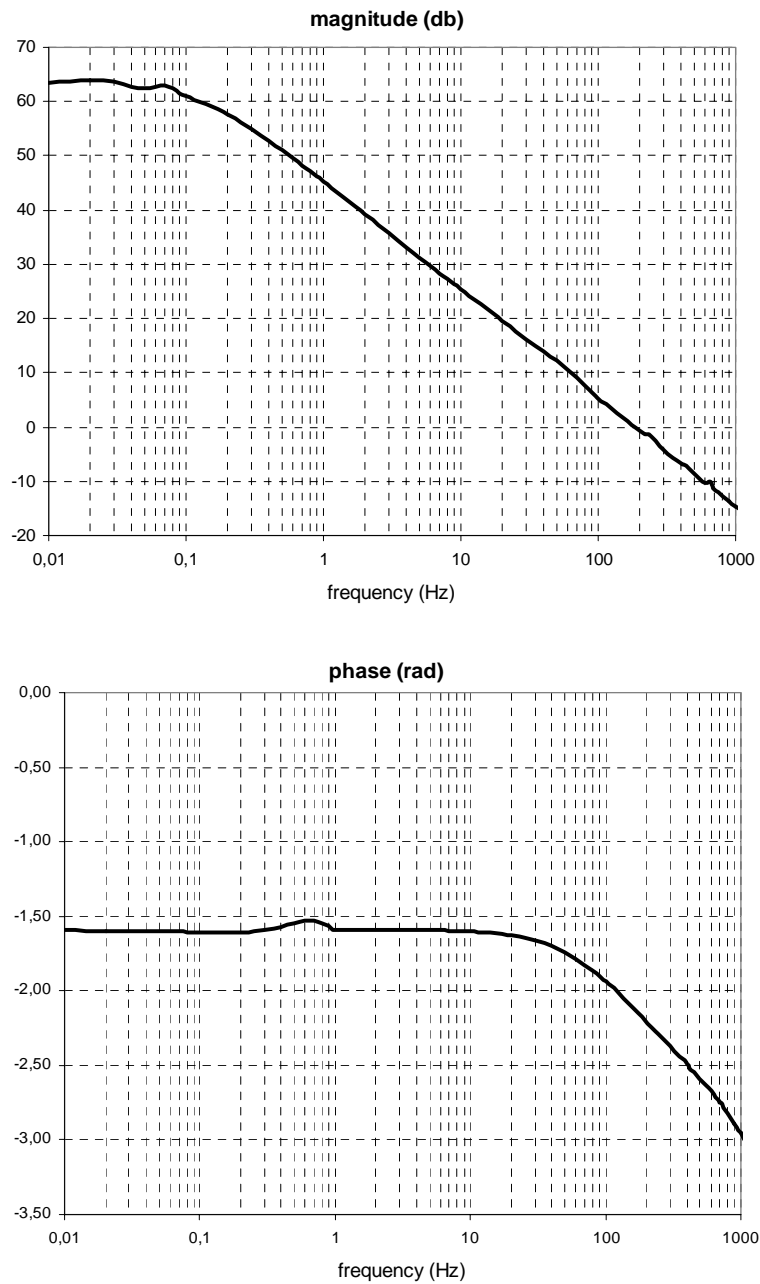


Figure 5.16: Bode diagram of the frequency response function $g_{44}(j\omega)$ of the Astig45 control at open loop

Astig45 Closed loop

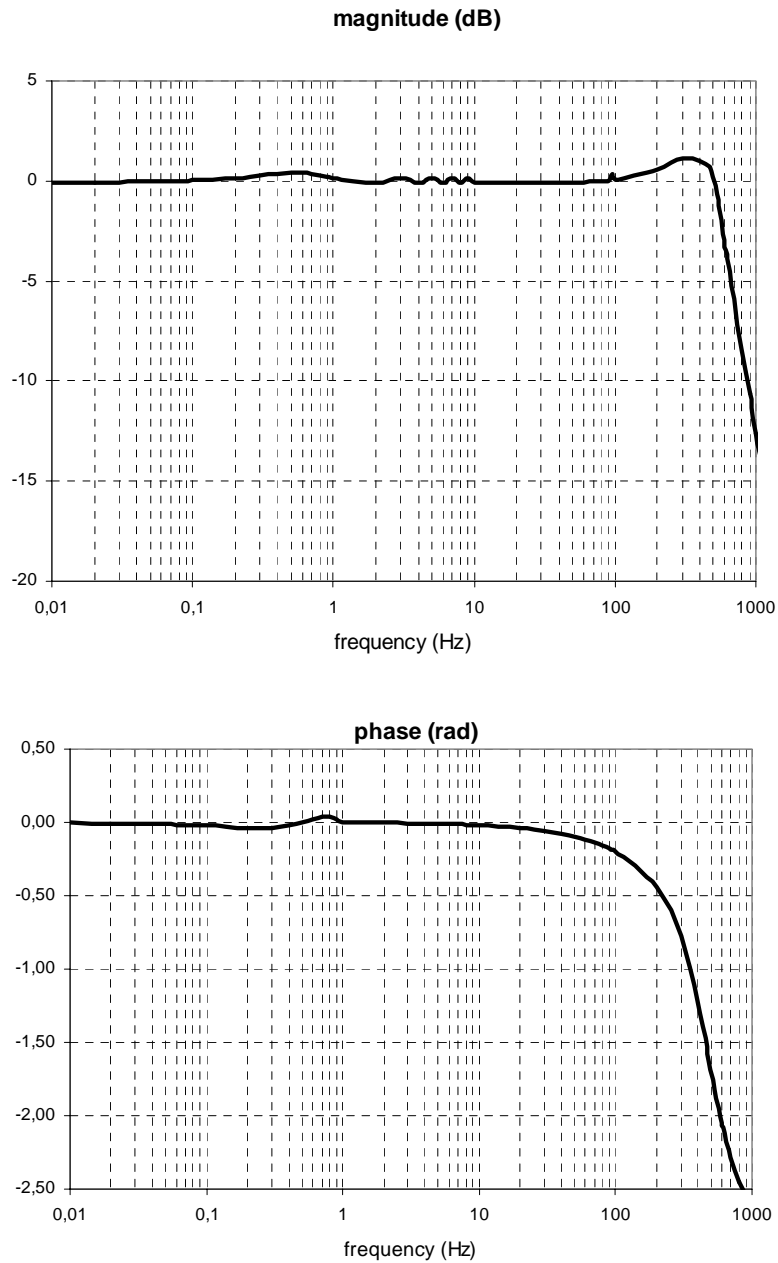


Figure 5.17: Bode diagram of the frequency response function $f_{44}(j\omega)$ of the Astig45 control at closed loop

Astig90 Open loop

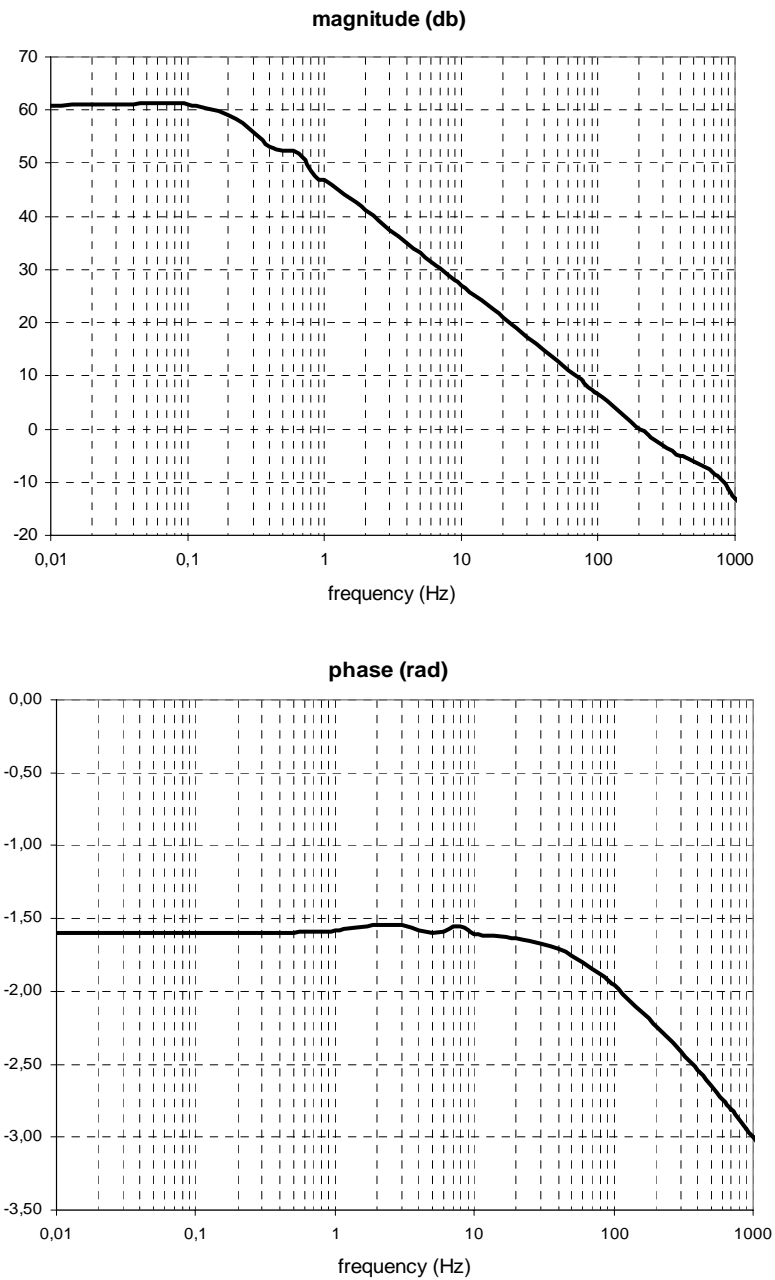


Figure 5.18: Bode diagram of the frequency response function $g_{55}(j\omega)$ of the Astig90 control at open loop

Astig90 Closed loop

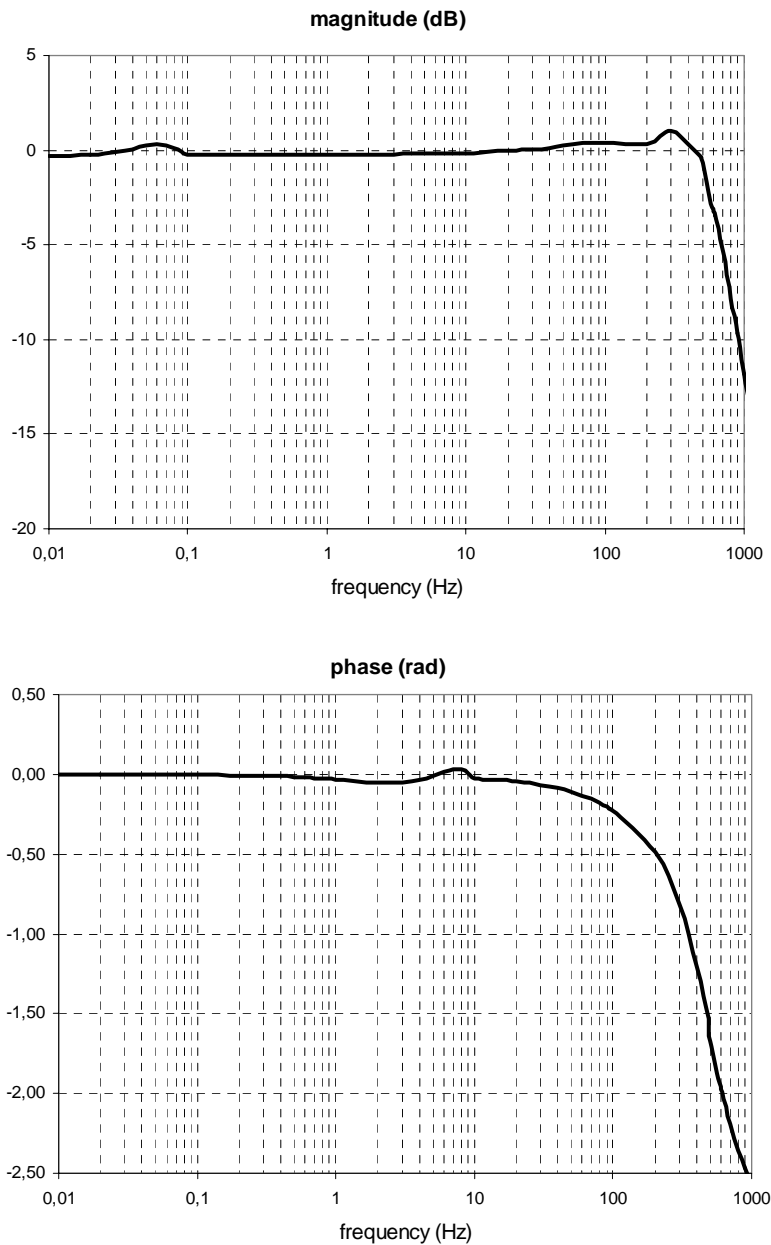


Figure 5.19: Bode diagram of the frequency response function $f_{55}(j\omega)$ of the Astig90 control at closed loop

Defocus Open loop

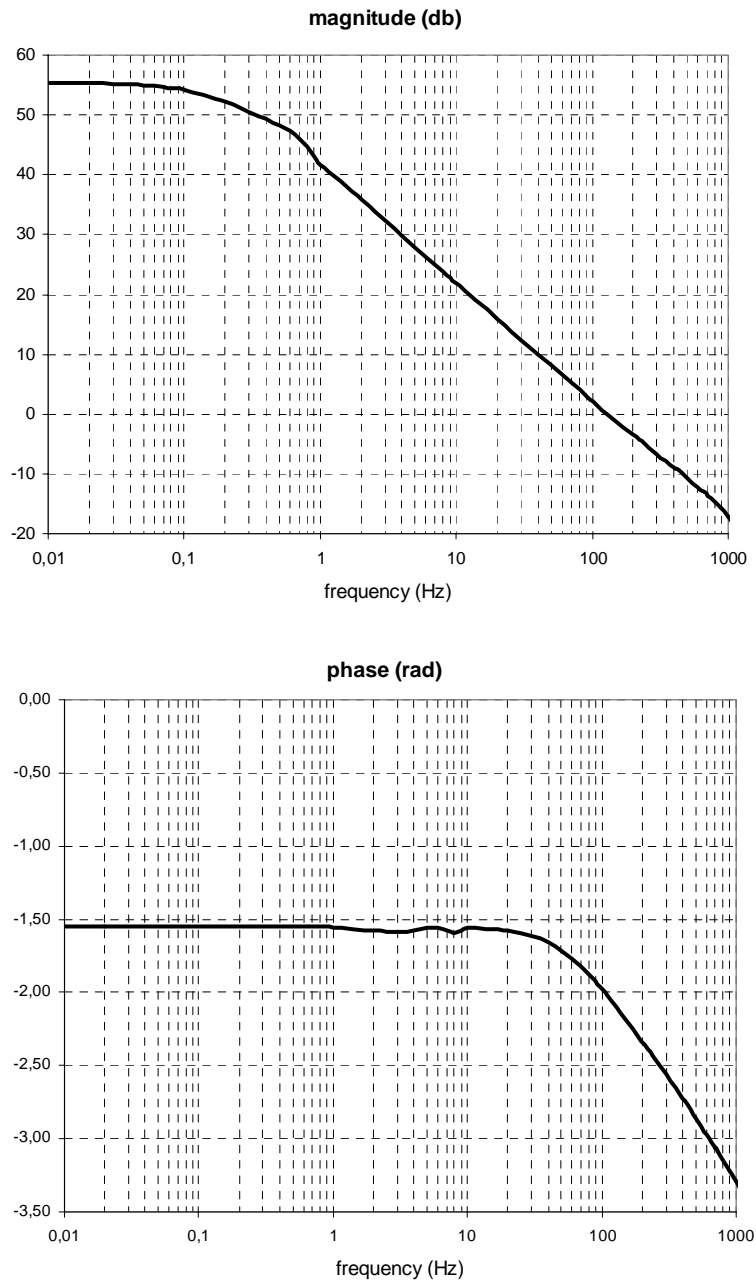


Figure 5.20: Bode diagram of the frequency response function $g_{66}(j\omega)$ of the Defocus control at open loop

Defocus Closed loop

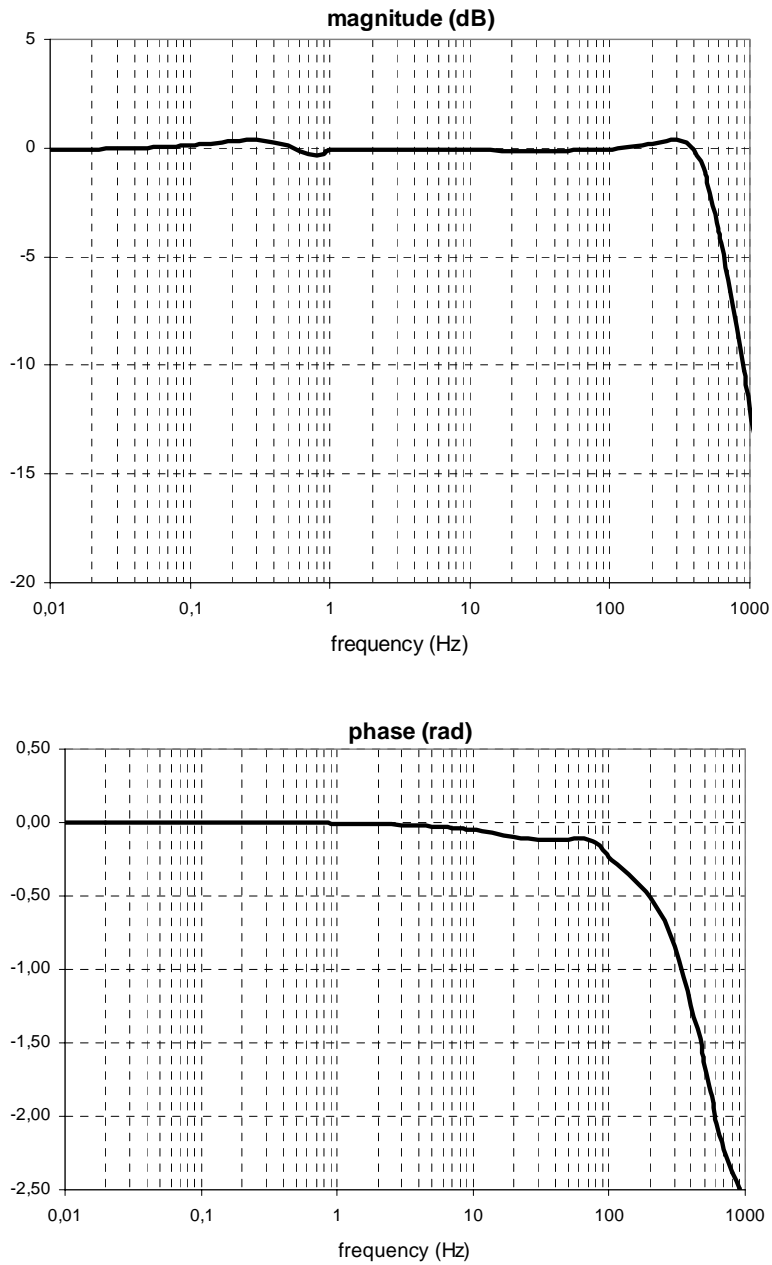


Figure 5.21: Bode diagram of the frequency response function $f_{66}(j\omega)$ of the Defocus control at closed loop

These measures permit to identify the parameters characterizing the adaptive control system. In particular, from the diagrams of the frequency responses at open loop we see that each control exhibits static gain of the order of $60 \div 70$ dB which decreases with slope of -20 dB/decade beyond the cut off frequency of 0.1 Hz set by the low pass filter used as correcting network for the stability. This implies that these six curves reach the unitary gain at about 200 Hz. Therefore the wavefront correction on the six modes is expected to be robust and effective in the band of few hundreds of Hz which is particularly interesting for Virgo application. Furthermore, amplitude and phase margins lay all within the range 12 dB \div 16 dB and 0.78 rad \div 1.05 rad respectively and therefore the Nyquist stability is fulfilled. Finally, the frequency response diagrams of the closed loop controls show the typical behaviour of second order systems with resonance frequencies ranging from 400 Hz to 500 Hz and bandwidth of about 600 Hz.

The values of the referred parameters are all listed in the following table 5.1.

Mode	Open loop				Closed loop	
	Static Gain at 0.01Hz	Unitary Gain	Amplitude Margin	Phase margin	Resonance frequency	Bandwidth
	dB	Hz	dB	rad	Hz	Hz
Longitudinal	66	235	15,2	0,86	480	601
TiltX	64	230	14,9	0,87	520	595
TiltY	67	220	15,9	0,88	530	610
Astig45	63	188	15,9	0,96	470	600
Astig90	61	205	15,8	0,9	490	590
Defocus	56	130	14,7	1,04	480	570

Table 5.1: operative parameters of the six feedback controls measured for the characterization of the Adaptive Optics Prototype implemented in laboratory

With reference to figures 5.22 and 5.23, where we have respectively plotted static gain and unitary gain of the six modes, we see that TiltY control has the maximum static gain equal to 67 dB while longitudinal control exhibits the largest unitary gain frequency of 235 Hz.

More generally, the correction of the first three modes (longitudinal, TiltX and TiltY) is more robust and wideband than the correction of the second

three modes (Astigm45, Astig90 and Defocus) and this appears reasonable to the author because these last modes correspond to second order Zernike polynomials and then require patterns of deformation for the adaptive mirror that are more difficult to achieve in real actuators.

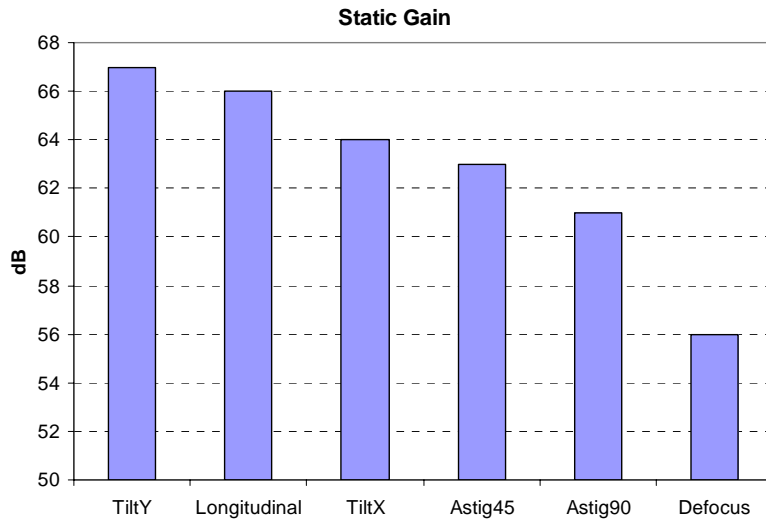


Figure 5.22: measured static gain of the six controls of the AO system

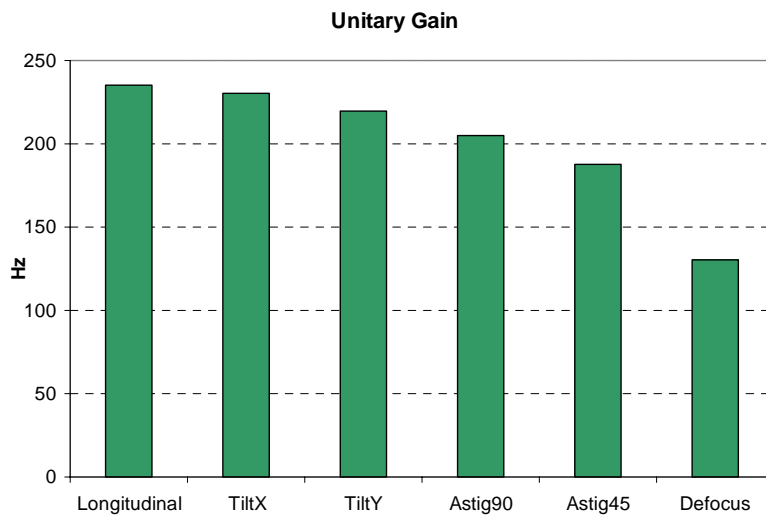


Figure 5.23: measured unitary gain of the six controls of the AO system

5.2 Measurement of residual noise in the controlled laser beam

We have directly tested the laser beam jitters suppression performed by our Adaptive Optics Prototype. The results demonstrate the compliance with Virgo requirements as stated in Chapter 1, which provide for 40 dB noise reduction at low frequency below 1 Hz and 20 dB below few tens of Hz.

To execute the test we have put into operation the Prototype and measured the six aberration coefficients of the controlled laser beam with the adaptive control firstly at open loop and secondly at closed loop. By comparing the values of the coefficients in the two cases, we have checked the actual noise reduction and measured the gap between free laser original noise and residual noise of the controlled beam. The reduction that we have simultaneously measured on the six aberration coefficients when the AO control loop is closed demonstrates the good performance of our system.

In the following, we shortly discuss the statistical processing techniques that we have used to analyze the measured noise. After that, we talk about the methodology of measurement based on the collection of digital data with sampling frequency chosen upon the Nyquist Shannon theorem. Finally, we present the measures of the six aberration coefficients and discuss the difference between free noise at open loop and residual noise at closed loop. In particular, we report the time variation of the six coefficients and calculate their RMS residual values. The same data are also processed in terms of Power Spectral Density curves and the noise reduction is reported in the different spectral ranges for comparison with Virgo requirements.

5.2.1 Some theoretical principles

Let us consider the time evolution of the physical parameter x that in each instant t has the probability of assuming a certain value. This is called *stochastic process* $x(t)$ and is characterized by the function of probability distribution of the first order $f(x,t)$ [108], [109].

The *mean value* of $x(t)$ is the time dependent function given by:

$$\eta(t) = E[x(t)] = \int_{-\infty}^{+\infty} xf(x,t)dx \quad (5.12)$$

which represents the expected value of the variable.

It is also defined the statistical parameter named *autocorrelation function*:

$$R(t_1, t_2) = E[x(t_1)x(t_2)] = \int_{-\infty}^{+\infty} x_1 x_2 f(x_1, x_2, t_1, t_2) dx_1 dx_2 \quad (5.13)$$

where x_1 and x_2 are the variable values at instants t_1 and t_2 , and $f(x_1, x_2, t_1, t_2)$ is the function of probability distribution of the second order.

The stochastic process is stationary if, for each real value $\varepsilon \in \mathcal{R}$, the two variables $x(t)$ and $x(t+\varepsilon)$ have the same statistics. This implies that the function of probability distribution of the first order is constant, or:

$$f(x, t) = f(x) \quad (5.14)$$

and that the function of probability distribution of the second order depends on the time difference $\tau = t_1 - t_2$, or:

$$f(x_1, x_2, t_1, t_2) = f(x_1, x_2, \tau) \quad (5.15)$$

The mean value is then time independent:

$$\eta = E[x(t)] = \int_{-\infty}^{+\infty} x f(x) dx = \text{const} \quad (5.16)$$

and the autocorrelation function is only dependent on τ .

$$R(\tau) = E[x(t+\tau)x(t)] = \int_{-\infty}^{+\infty} x_1 x_2 f(x_1, x_2, \tau) dx_1 dx_2 \quad (5.17)$$

The process $x(t)$ is *ergodic* when the mean of ensemble of eq. (5.16) and the autocorrelation function of eq. (5.17) can be replaced by time averages, as:

$$\eta \equiv \lim_{T \rightarrow \infty} \frac{1}{2T} \int_{-T}^{+T} x(t) dt \cong \frac{1}{2T} \int_{-T}^{+T} x(t) dt \quad (5.18)$$

and

$$R(\tau) \equiv \lim_{T \rightarrow \infty} \frac{1}{2T} \int_{-T}^{+T} x(t+\tau)x(t)dt \cong \frac{1}{2T} \int_{-T}^{+T} x(t+\tau)x(t)dt \quad (5.19)$$

The *Power Spectrum* $S(\omega)$ or *Power Spectral Density (PSD)* of the process $x(t)$ is defined as the Fourier transform of the autocorrelation function, that is:

$$S(\omega) = \int_{-\infty}^{+\infty} R(\tau) e^{-j\omega\tau} d\tau \quad (5.20)$$

with the inverse:

$$R(\tau) = \frac{1}{2\pi} \int_{-\infty}^{+\infty} S(\omega) e^{j\omega\tau} d\omega \quad (5.21)$$

If we calculate $R(\tau)$ in $\tau=0$ and use eq. (5.19), we have:

$$R(0) = \frac{1}{2\pi} \int_{-\infty}^{+\infty} S(\omega) d\omega = \frac{1}{2T} \int_{-T}^{+T} |x(t)|^2 dt = E[|x(t)|^2] \quad (5.22)$$

The PSD is of particular interest in experiments where signal processing is required because the area of the function $S(\omega)/2\pi$ over the whole spectral range is the mean power of the process $x(t)$. It is usually preferred to use the square root of the PSD $\sqrt{S(\omega)}/2\pi$, whose integral over the spectral range represents the RMS of the process $x(t)$. The unit of measure of the square root of the PSD is equal to $A/\sqrt{\text{Hz}}$, being A the unit of measure of the process $x(t)$. In the following we will speak only of PSD, even if meaning its square root, for the sake of simplicity.

A linear system of frequency response $G(j\omega)$ transforms the PSD $\sqrt{S_x(\omega)}$ of the input $x(t)$ into the PSD $\sqrt{S_y(\omega)}$ of the output $y(t)$ according to:

$$\sqrt{S_y(\omega)} = G(j\omega) \sqrt{S_x(\omega)} \quad (5.23)$$

So, if we want to suppress stochastic noise of a given signal in a selected frequency range, we can use a filtering system of suitable frequency response that suppresses the input noise exactly in that spectral interval.

In our experiment we have designed an AO system based on the scheme of closed loop automatic control in order to perform active filtering of laser beam stochastic jitters. For each of the six degrees of freedom x_i ($i=1,...,6$) corresponding to first and second order jitters, we expect PSD reduction as:

$$\sqrt{S_{y_i}(\omega)} = \frac{1}{1 + g_{ii}(j\omega)} \sqrt{S_{x_i}(\omega)} \quad (5.24)$$

in accordance with the theory of automatic controls, being g_{ii} the open loop gain of the control acting of the i^{th} mode, $S_{x_i}(\omega)$ the initial spectral power and $S_{y_i}(\omega)$ the jitters spectral density after correction. The measures presented in the following demonstrate the success of that prediction.

5.2.2 Methodology of measurement

The target of our measurement is to demonstrate the control effectiveness. To do that, we have measured the aberration signals $S_i(t)$ at open loop and at closed loop and compared the two results to test the actual noise reduction.

We have directly measured the 25 voltages emerging from the photodiode amplifiers and converted into digital form by the ADC board. Each voltage is sampled and saved in the form of a string of data on the hard disk of the PC. This procedure allows us to process off line the data of the 25 channels and then to extract the aberration coefficients $S_i(t)$ using the combinations of table 3.1. The strings of data corresponding to the time variation of $S_i(t)$ have been statistically processed with the commercial software Matlab [110] to calculate RMS and Power Spectral Density.

The sampling frequency f_s and the period T for string data collection have been chosen in accordance with the theory of digital data processing [111].

In particular, as we are interested to signal spectral analysis in the bandwidth of 1 kHz, we have set the sampling frequency on 2 kHz in compliance with the Nyquist-Shannon theorem.

The period T of data collection has been calculated from the equation:

$$T = \frac{10}{\delta f} \quad (5.25)$$

that is 10 times the inverse of the minimum resolution δf required for the spectral analysis.

We have used the value $\delta f = 0.1 \text{ Hz}$ and then the minimum period T for data collection is 1 minute and 40 seconds. We have programmed the Labview Instrument for data collection on a period T of 2 minutes.

We have carried out five sets of measurements to collect 25 voltage signals of the photodiodes respectively under the following operative conditions:

No.	Operative condition on the photodiodes surface	Adaptive Control
1	Dark. No laser beam.	Open loop
2	Laser beam from the arm of the piezo. Beam from the arm of the adaptive mirror screened.	Open loop
3	Laser beam from the arm of the adaptive mirror. Beam from the arm of the piezo screened.	Open loop
4	Interference of the two beams	Open loop
5	Interference of the two beams	Closed loop

Table 5.2: operative conditions for the five sets of measurements carried out to test the AO control

The first set is necessary to measure the dark noise of the system.

Measurements 2 and 3 allow to calibrate the Gaussian profile on the photodiodes plane and to check the mode matching providing for $w_2 = 2 \text{ mm}$.

From measurement no. 4 we extract error signals at open loop compared with error signals at closed loop achieved from measurement no. 5.

5.2.3 Results and discussion

We report 12 graphs representing time variation and Power Spectral Density of the six aberration coefficients.

The signals in the time domain are reported in Volts as measured at the output of the photodiode amplifiers and plotted from 0 to 120 seconds; on the contrary, in the frequency range from 0,1 Hz to 1 kHz we make the spectral analysis of the adimensional coefficients normalized to the maximum value measured at open loop as we are interested to the relative correction.

Each graph includes three curves corresponding respectively to dark noise, free noise at open loop and residual noise at closed loop of the specific degree of freedom. The comparison of these curves is widely discussed below.

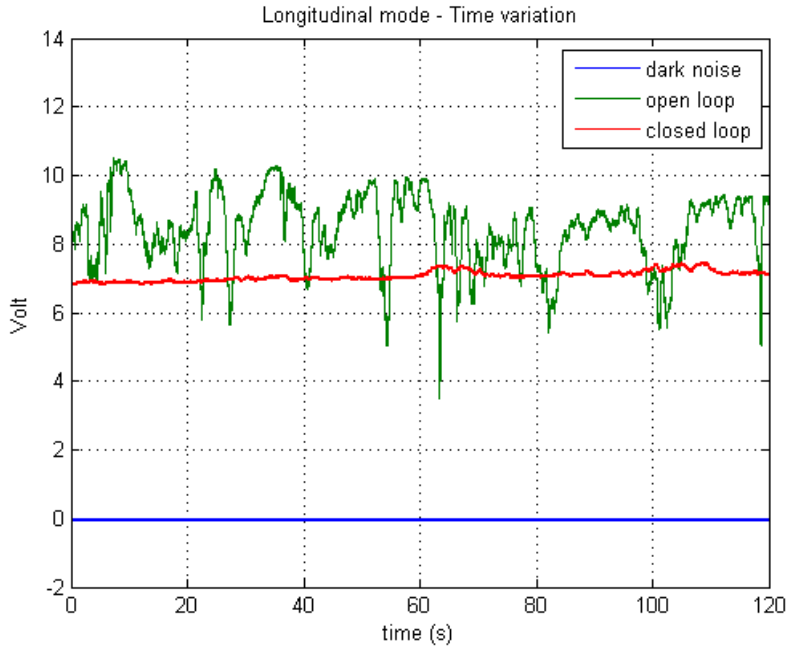


Figure 5.24: time variation of the coefficient relative to longitudinal mode

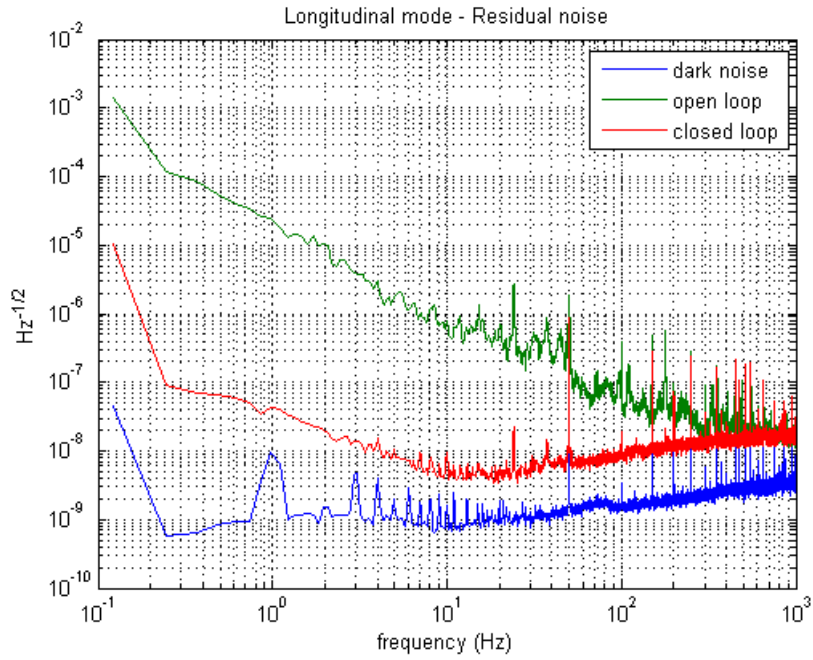


Figure 5.25: Power Spectral Density of the coefficient relative to longitudinal mode

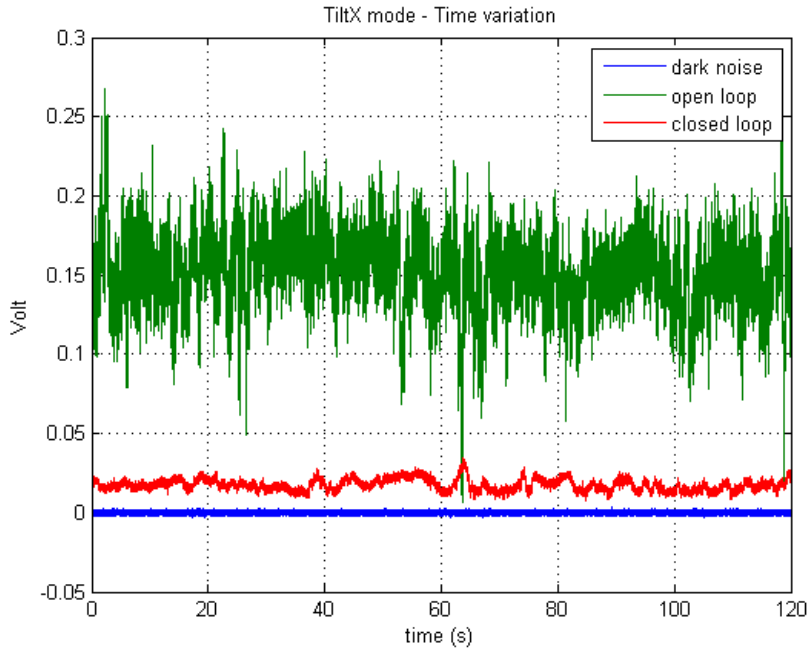


Figure 5.26: time variation of the coefficient relative to TiltX mode

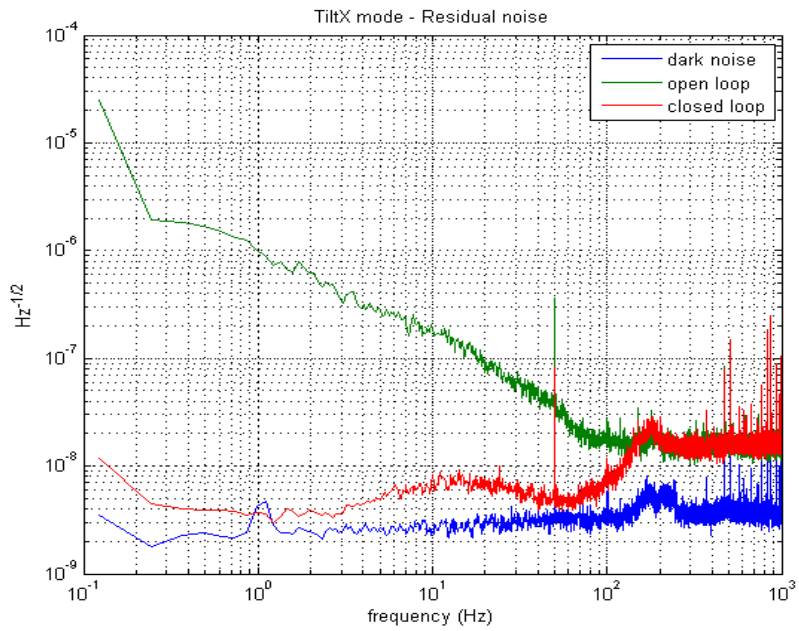


Figure 5.27: Power Spectral Density of the coefficient relative to TiltX mode

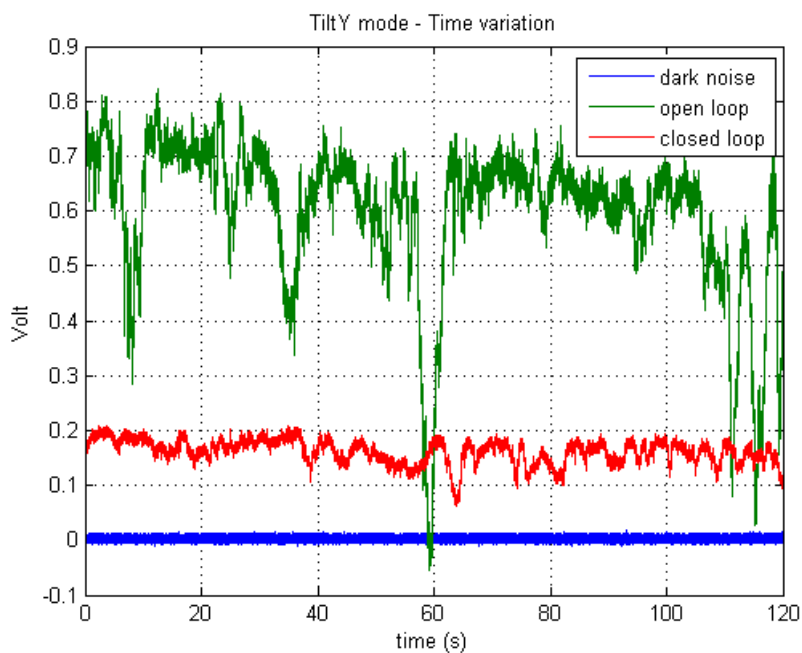


Figure 5.28: time variation of the coefficient relative to TiltY mode

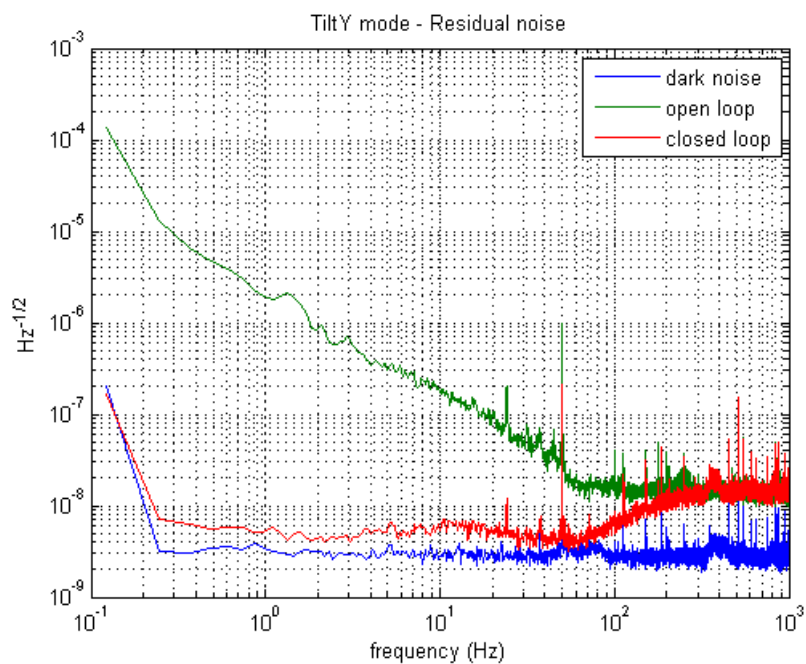


Figure 5.29: Power Spectral Density of the coefficient relative to TiltY mode

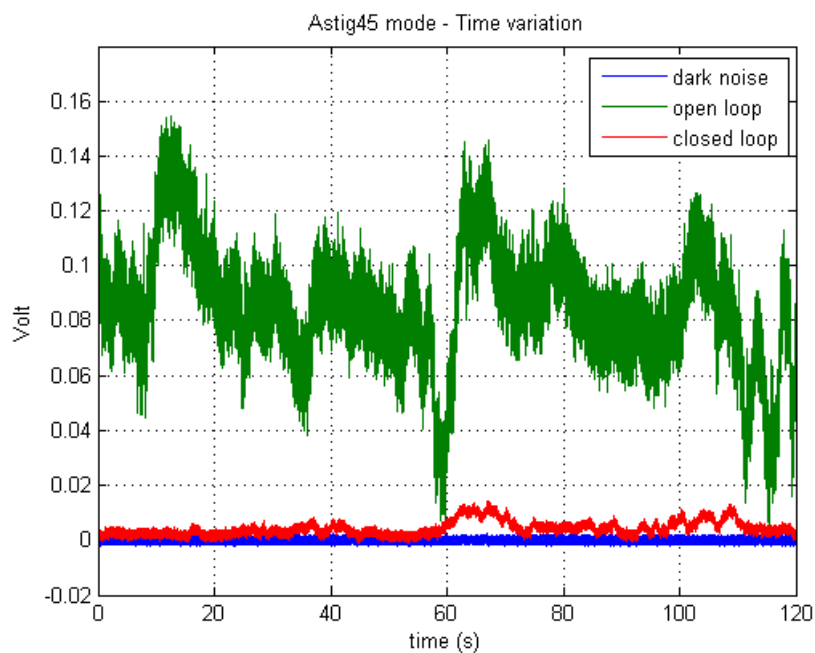


Figure 5.30: time variation of the coefficient relative to Astig45 mode

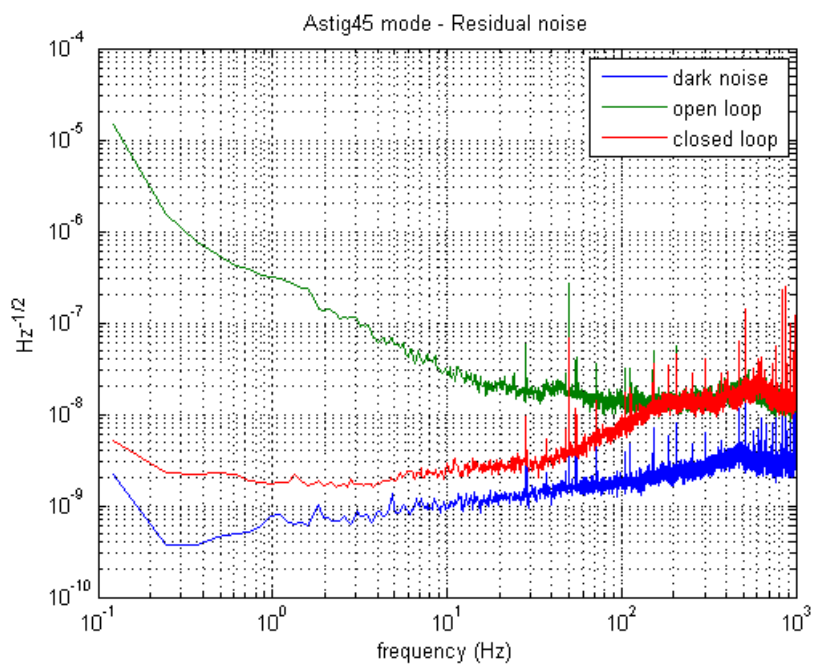


Figure 5.31: Power Spectral Density of the coefficient relative to Astig45 mode

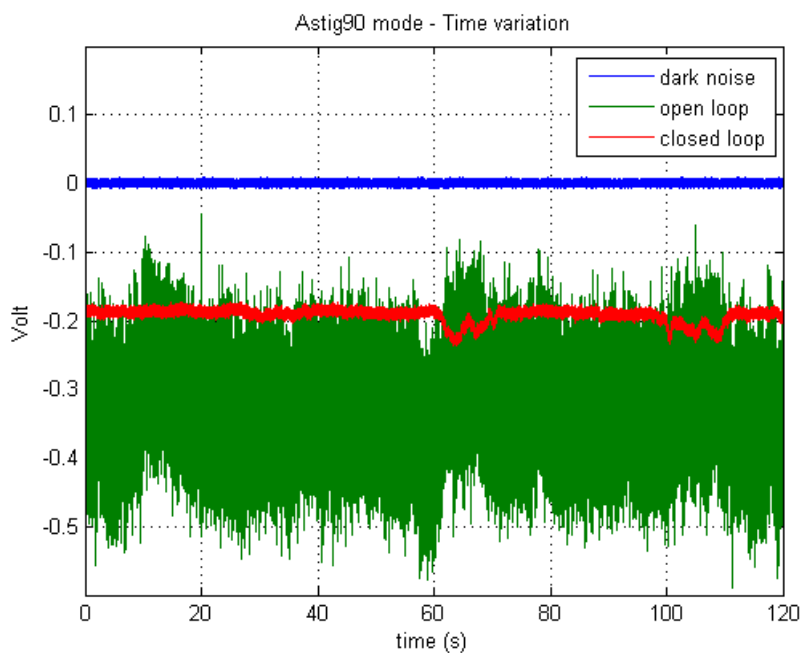


Figure 5.32: time variation of the coefficient relative to Astig90 mode

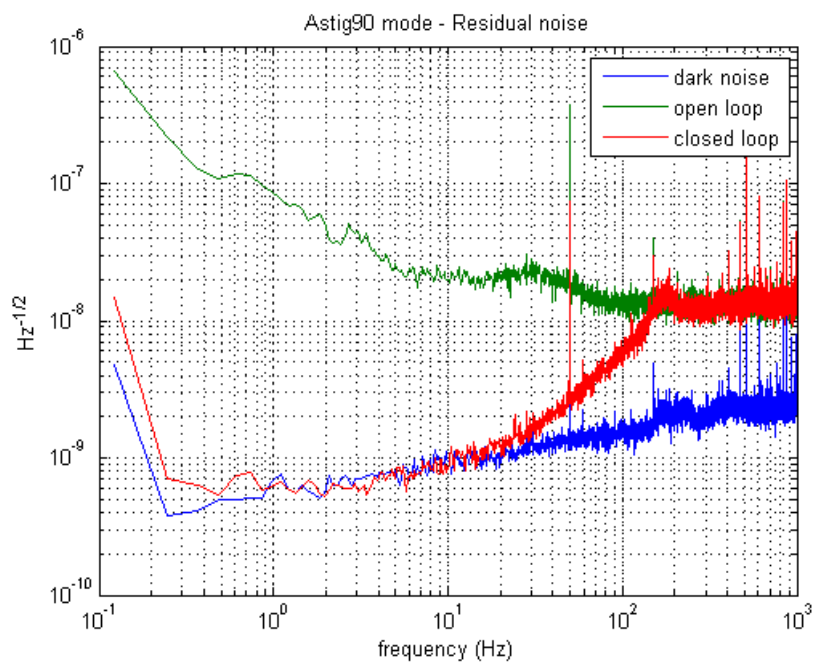


Figure 5.33: Power Spectral Density of the coefficient relative to Astig90 mode

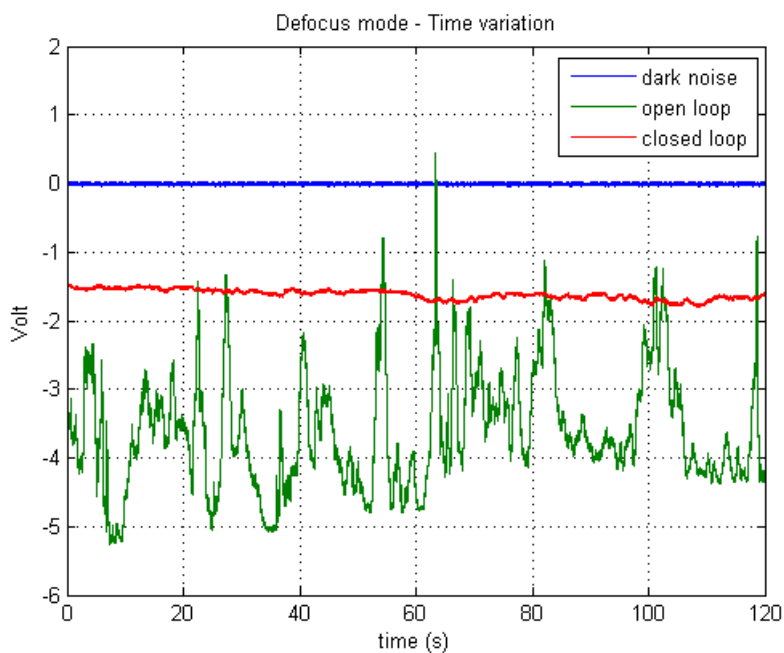


Figure 5.34: time variation of the coefficient relative to Defocus mode

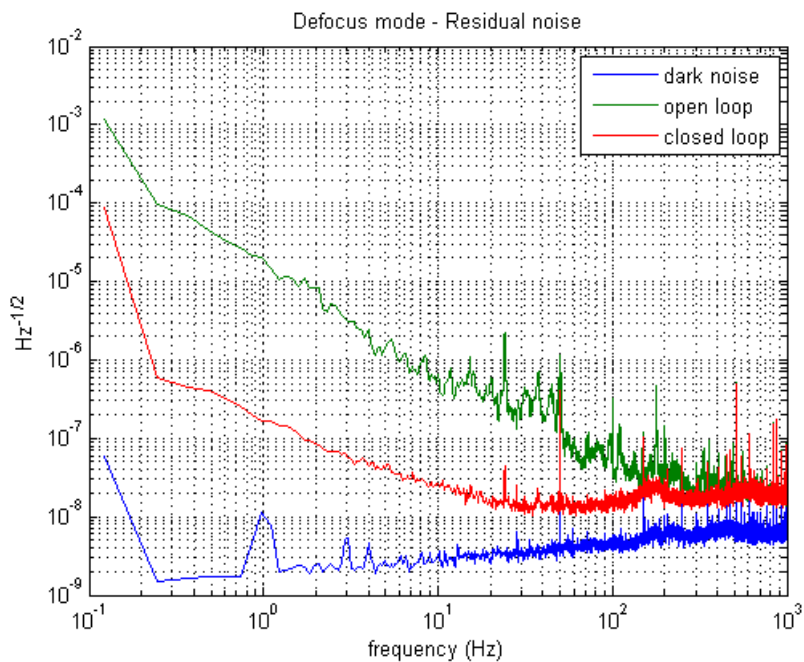


Figure 5.35: Power Spectral Density of the coefficient relative to Defocus mode

From the curves of time variation we see that the laser beam undergoes important reduction of its geometrical fluctuations when the adaptive control loop is closed. In fact such curves exhibit large RMS reduction on the y scale. In table 5.3 all the RMS values are listed for the complete comparison of the coefficients at open loop and closed loop.

Mode	RMS (Volts)	
	open loop	closed loop
Longitudinal	8,5	7,07
TiltX	0,15	0,02
TiltY	0,62	0,16
Astig45	0,09	0,005
Astig90	0,33	0,19
Defocus	3,72	1,62

Table 5.3: RMS values of the aberration coefficients at open loop and at closet loop

The Longitudinal mode is stabilized on the value of 7 *Volts* corresponding to the half fringe lock in of the interferometer (the contrast of the Michelson previously investigated with the piezo mirror ranges from 0 to 14 *Volts*). The Defocus term presents non null RMS value of 1.6 *Volts* due to residual coupling effects with the Longitudinal mode originated by deformable mirror and sensing system. The other coefficients have evident RMS reduction which demonstrates the effectiveness of the control.

The Fourier analysis of the noise reduction can be carried out from the Power Spectral Density curves where we distinguish three different spectral ranges. In the low frequency band up to 10 *Hz*, the control is much robust and effective as expected for the high value of open loop gain exhibited in the corresponding Bode diagrams. In this region the noise reduction changes progressively from three to two orders of magnitude (from 60 *dB* to 40 *dB*) in good compliance with the Virgo requirements stated before.

In the central band 10 *Hz* ÷ 100 *Hz* the control still performs, but the loop gain decreases and the noise reduction drops down to 20 *dB*. Nevertheless this value fits again the Virgo requirements for frequencies of few tens of *Hz*.

Finally, in the upper band beyond 100 *Hz* the control does not work as the it reaches its unitary gain frequency that for all the degrees of freedom stands around 200 *Hz*. Over this limit free noise at open loop and residual noise at closed loop coincide.

We note that the residual noise is often close to the dark noise and therefore for further improvements more performing components are necessary. In the table below we list the aberration reduction at three typical frequencies corresponding to 1 Hz, 10 Hz and 100 Hz.

Mode	Noise reduction		
	1 Hz	10 Hz	100 Hz
<i>Longitudinal</i>	$1.7 \cdot 10^{-3}$	$7 \cdot 10^{-3}$	$1.5 \cdot 10^{-1}$
<i>TiltX</i>	$3.8 \cdot 10^{-3}$	$3.6 \cdot 10^{-2}$	$4 \cdot 10^{-1}$
<i>TiltY</i>	$2.7 \cdot 10^{-3}$	$3 \cdot 10^{-2}$	$4.4 \cdot 10^{-1}$
<i>Astig45</i>	$6 \cdot 10^{-3}$	$8.7 \cdot 10^{-2}$	$4.5 \cdot 10^{-1}$
<i>Astig90</i>	$7 \cdot 10^{-3}$	$4.5 \cdot 10^{-2}$	$4.1 \cdot 10^{-1}$
<i>Defocus</i>	$9 \cdot 10^{-3}$	$5.2 \cdot 10^{-2}$	$4 \cdot 10^{-1}$

Table 5.4: measured data of noise reduction of the six aberration coefficients

It is also useful to see figure 5.36 where we have an immediate outlook of noise reduction expressed in dB for the six degrees of freedom in the three main frequencies of interest.

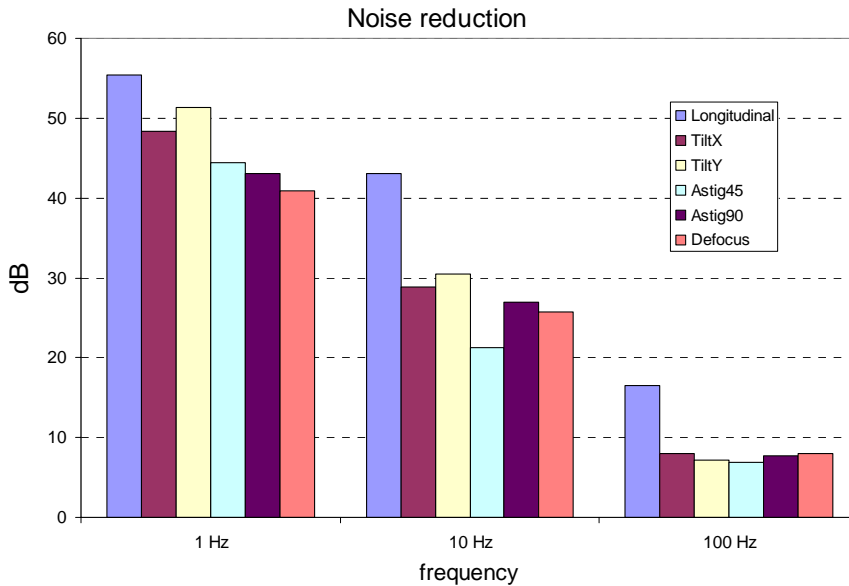


Figure 5.36: noise reduction of the six aberration modes expressed in dB

The fulfilment of Virgo requirements is demonstrated: in fact the six coefficients corresponding to first and second order Hermite Gauss modes exhibit simultaneous suppression of more than 40 *dB* at 1 *Hz* and of more than 20 *dB* at 10 *Hz* when the AO control loop is closed.

5.3 Quality control of the Gaussian beam

We have completed our experimental work by carrying out the quality control of the Gaussian beam after wavefront correction.

According to the quality procedures based on international standards such as *ISO 9001*, we have defined a numerical indicator which is representative of the quality of the Gaussian beam; therefore we have measured that parameter for the laser beam before and after the AO correction in order to check the expected improvements performed at closed loop.

In this section, after the description of theoretical principles and of the methodology of measurement, we present and discuss the obtained results.

5.3.1 Some theoretical principles

We have assumed that in our Michelson interferometer one arm is passed through by the reference Gaussian beam while the other arm contains the laser beam perturbed by higher order Hermite Gauss modes. In the previous Section we have demonstrated that our AO system performs the suppression of the Hermite Gauss perturbations up to the second order and this allows to consider the corrected laser beam with good approximation similar to the fundamental Gaussian beam of the reference arm.

In order to check the quality of the laser beam cleaned up from the initial jitters, we have directly measured the transverse intensity profile originated at the photodiodes array by the interference of the reference beam with the beam under test. The experimental data collected on the photodiodes are then compared with the ideal Gaussian profile expected if the two beams were perfectly matching on the fundamental mode. The discrepancy of the actual data from the ideal curve is key indicator of the laser beam quality.

In fact, provided that the Michelson is locked on the middle fringe working point, two ideal interfering beams would have phase fronts perfectly parallel

and shifted by the phase factor $\delta = \pi/2$. Therefore the intensity at the output of the Michelson should correspond point by point to the ideal Gaussian profile:

$$I_{out}^{ideal}(r) = \frac{I_0}{2} e^{-\left(\frac{r}{w_2}\right)^2} \quad (5.26)$$

being I_0 the input laser beam intensity, r the radial distance from the optical axis and w_2 the beam waist matched on the photodiodes array (figure 5.37).

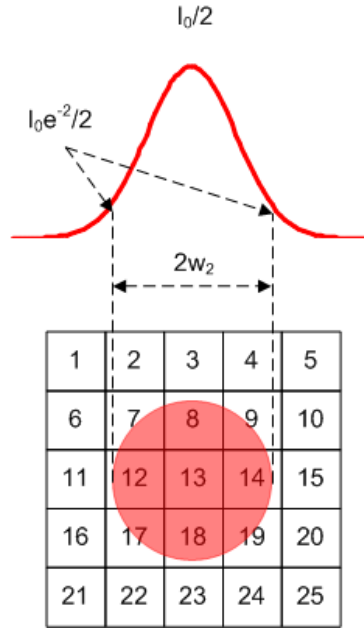


Figure 5.37: laser spot of diameter $2w_2$ covering the photodiodes array and projection of the corresponding 2D intensity profile. In the ideal case this profile is perfectly Gaussian and centred on the central pixel n. 13

On the contrary, in the real case one of the two beams is perturbed and therefore the two wavefronts do not overlap due to instantaneous variations induced by jitters. This means that the phase difference δ of the two beams is not perfectly fixed on $\pi/2$ but has small time and position fluctuations, or $\delta = \delta(r, t)$.

Thus the intensity at the output of the Michelson, given by:

$$I_{out}^{real}(r) = \frac{I_0}{2} (1 + \cos \delta(r, t)) \cdot e^{-\left(\frac{r}{w_2}\right)^2} \quad (5.27)$$

exhibits a variance from the ideal case of eq. (5.26) as shown in figure below

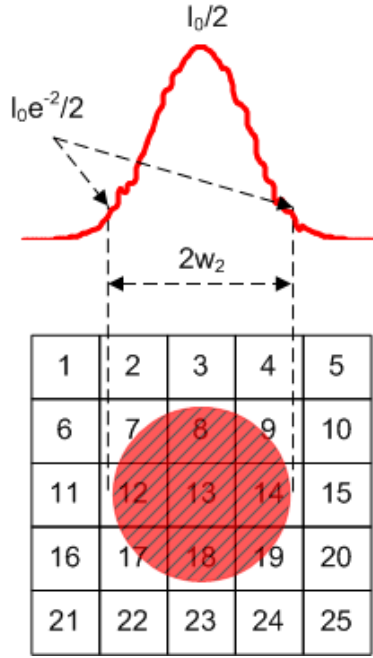


Figure 5.38: laser spot of diameter $2w_2$ covering the photodiodes array and projection of the corresponding 2D intensity profile. In the real case this profile has a variance from the perfect Gaussian curve

The variance of the real curve of eq. (5.27) from the ideal curve of eq. (5.26) represents the degree of perturbation of the laser beam under test: in fact it is null if the beam is perfectly Gaussian and increases with the laser jitters.

Our AO control system is expected to reduce the laser beam perturbation and increase its quality towards the limit of perfect Gaussian profile corresponding to null variance of the curve (5.27) from the ideal limit (5.26).

The method that we have used to measure the quality of the beam is then to calculate that variance. This is made by fitting the intensity data collected at the photodiodes with the ideal curve of eq. (5.26) using the χ^2 test [112] as numerical indicator of the degree of compliance.

Usually, if we want to fit N measured variables y_k of standard deviation σ_{y_k} to the theoretical curve $y=f(x)$, the χ^2 parameter is defined as:

$$\chi^2 = \sum_{k=1}^N \frac{(y_k - f(x_k))^2}{\sigma_{y_k}^2} \quad (5.28)$$

In this form, the parameter χ^2 is null if each measure y_k corresponds exactly to the theoretical value $f(x_k)$ and diverges if the experimental data do not fit the ideal curve.

In our case we measure the five intensities I_k corresponding to the central points x_k of the photodiodes $k=11, 12, 13, 14, 15$ of figure 5.38. In order to have a parameter proportional to the compliance of the measures with the ideal Gaussian profile $I=G(x)$, we have used the following indicator:

$$\chi^2(\%) = \left[1 - \frac{\sum_{k=11}^{15} \frac{1}{\Delta I_k^2} \left(\frac{\overline{I_k} - G(x_k)}{G(x_k)} \right)^2}{\sum_{k=11}^{15} \frac{1}{\Delta I_k^2}} \right] \times 100 \quad (5.29)$$

which ranges from 100% (total compliance) to 0% (no compliance) and is therefore the numerical parameter that we need to represent the quality of the laser beam under test.

5.3.2 Methodology of measurement

We have first measured the intensity curve produced on the photodiodes array by a single laser beam of the Michelson when the other is screened. This permits to calibrate the reference Gaussian curve with the measure of the central peak on the photodiode *no. 13* and to check the beam waist $w_2=2mm$ arranged with the mode matching.

After that, we have measured the intensity profile of the interference figure at open loop and at closed loop, and compared the two sets of data with the ideal Gaussian profile of beam waist $w_2=2mm$. The $\chi^2(\%)$ calculated in the two cases confirms the improvement of the laser beam quality when the adaptive control loop is closed.

The intensity data are sampled on the ADC board with frequency of 2 KHz and sent to the Labview Virtual Instrument programmed for the collection of strings of period $T=120$ seconds. This means that each string contains $N=240.000$ samples, which can be considered a sufficient number of measures for a good statistical processing [113].

In particular, we have calculated the mean value $\overline{I}_k = \frac{1}{N} \sum_{i=1}^N I_{ik}$ and the

standard deviation $\Delta I_k = \sqrt{\frac{1}{N-1} \sum_{i=1}^N (I_{ik} - \overline{I}_k)^2}$ ($k=11, 12, \dots, 15$) and therefore

plotted these five intensities with the error bar $(\overline{I}_k \pm \Delta I_k)$ against the corresponding x_k coordinate.

Using the $\chi^2(\%)$ as defined in eq. (5.29), we have fitted the experimental data with the theoretical curve of eq. (5.26) and the results that we have obtained are shown in the following Subsection.

5.3.3 Results and discussion

All the intensity measures are here reported in terms of W/m^2 and this has been possible because we have completely characterized the experimental set up. In particular, starting from the voltage signals read at the output of the photodiode amplifier, we have used the conversion factor $1V/20\mu A$ which transforms the photocurrents emerging from the photodiodes as discussed in Section 4.4. The photocurrents are converted into optical power by the factor $0.45 A/W$ extracted by the sensitivity curve of the photodiodes provided by the manufacturer Hamamatsu. And finally, the optical intensity can be calculated from the optical power on the area of $1.3 \times 1.3 \text{ mm}^2$ of the single photodiode.

The first graph in figure 5.39 shows the measured intensity produced by the single beam coming from one arm of the interferometer. The five experimental data permit to calibrate the ideal Gaussian profile which exhibits the central peak of $59 W/m^2$ and the $1/e^2$ beam waist of 2 mm as expected.

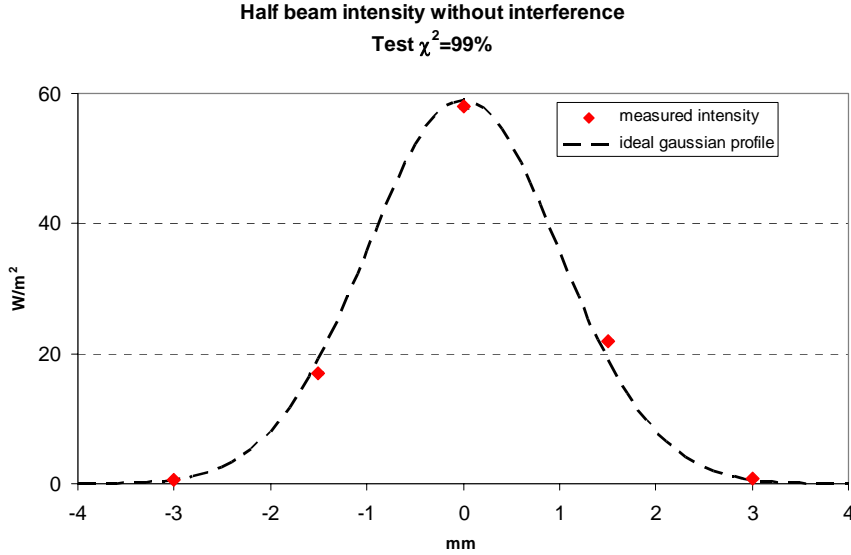


Figure 5.39: measured intensity of half beam from one arm of the interferometer and calibration of the ideal Gaussian profile. The central maximum is 59 W/m^2 and decreases to $1/e^2$ at 2mm from the center as predicted by the mode matching arrangement

This Gaussian profile which matches at $\chi^2(\%) = 99\%$ with the intensity data of the single beam is the reference curve that we use for the following two graphs.

We report the experimental data of the intensity produced by the interference of the two beams of the Michelson, respectively when the AO control is at open loop and at closed loop. The two sets of data are compared with the same calibrated Gaussian profile.

We can see that when the interferometer is not controlled by the AO system (figure 5.40), the five experimental data of the output intensity fit the ideal curve with factor $\chi^2(\%) = 84\%$.

On the contrary, when the adaptive control loop is closed (figure 5.41), we observe good compliance of the data, as the factor $\chi^2(\%)$ raises to 96% .

This observation is an evident improvement of the laser beam quality that can be with no doubt ascribed to the operation of our AO system.

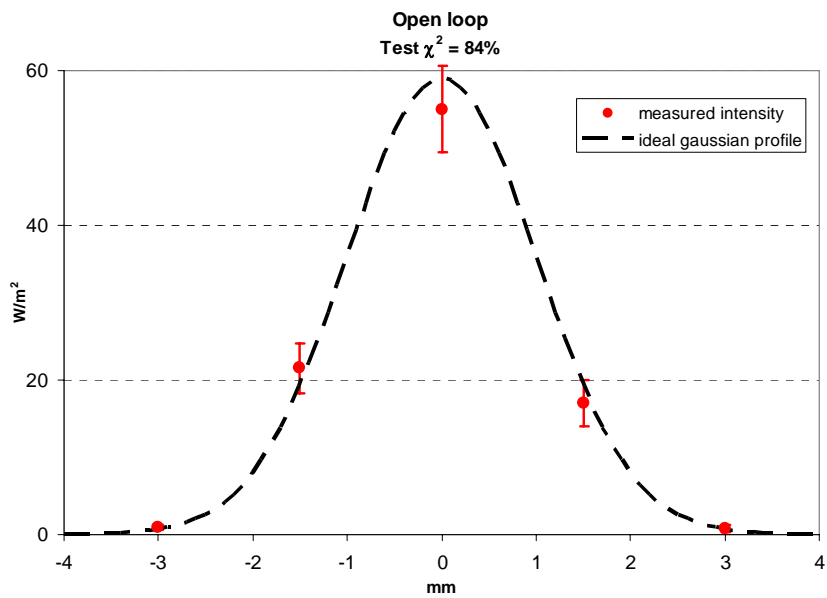


Figure 5.40: comparison between ideal Gaussian profile and measured intensity at open loop

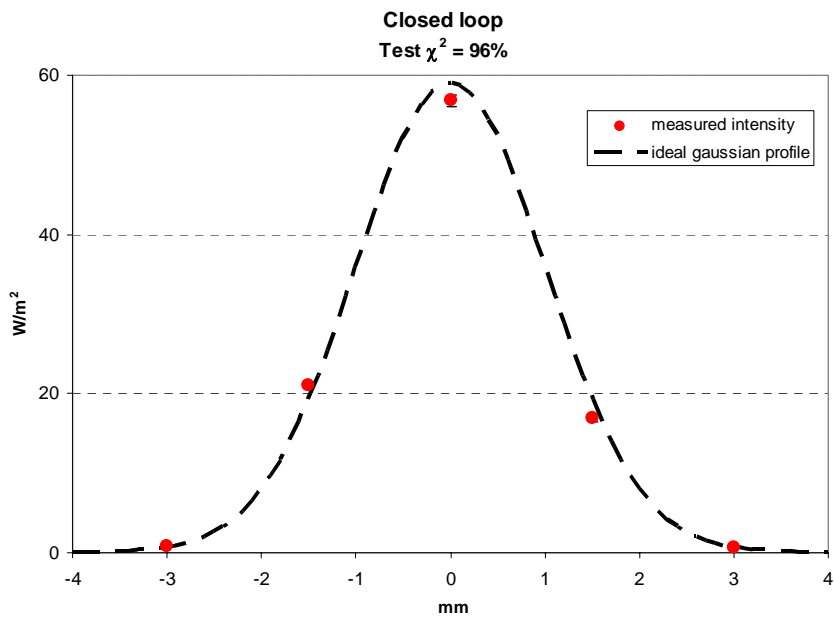


Figure 5.41: comparison between ideal Gaussian profile and measured intensity at closed loop

Conclusions

The Doctoral Work that we have carried out during these last three years has been finalized to develop and test an Adaptive Optics system that performs the effective suppression of the jitters affecting laser beams in air. Our target is to demonstrate the possible application of such system to interferometric gravitational antennas for the reduction of the intrinsic noise and the improvement of the sensitivity curve. The main researches and the results that we have achieved are reported in the present Thesis arranged in five Chapters.

In the first part of this paper we have discussed the principal aspects of the gravitational wave detection remarking the big difficulty due to the weakness of the signals expected from astronomical bodies. We have said that large scale ground based interferometers are the most promising GW antennas as they perform high sensitivity and wideband detection based on the movement of suspended masses in the typical Michelson configuration. Among the most important experiments that are currently being carried out all over the world, we have presented the Virgo Project and the characteristics of the GW antenna now operating on Cascina site. The Virgo antenna is a ground based Michelson interferometer of 3 *km* long arms designed for wideband GW detection (10Hz÷10kHz) with sensitivity of $\tilde{h} \approx 10^{-23} 1/\sqrt{\text{Hz}}$ at central frequency of 100 *Hz*. This value, which represents the lower limit of detectivity at the best of the present technology, has been gained thanks to sophisticated solutions implemented to reduce the different sources of noise that could affect the detector. Actually, the Virgo sensitivity is limited at low frequency by the seismic noise, at central band by the thermal noise and at high frequency by the shot noise.

The request for further improvements of the sensitivity curve for the Project of Virgo Upgrade and especially for Advanced Virgo, where the noise reduction of one order of magnitude is expected over the whole detection bandwidth, has given new impulse to research for the analysis and the reduction of noise. In particular, much attention is currently paid to the noise originated by the coupling between interferometer misalignments and input laser beam jitters. In fact, the passive filtering of the laser beam aberrations actually performed in the Virgo antenna by the mode cleaner put at the enter of the beam splitter is a partial solution that does not solve completely the problem, as the residual laser fluctuations still impose strict limitations to the alignment of the suspended optics. Therefore the definitive suppression of

free laser beam jitters is still an open issue that could be solved using a pre filtering system before the mode cleaner. This idea has driven the start up of our Ph.D. Work, based on the Virgo requirements which correspond to jitters reduction of at least 40 *dB* at low frequency $f < 1\text{Hz}$ and of 20 *dB* in the region of tens of *Hz*.

The second part of the Thesis has been devoted to investigate the modern techniques of Adaptive Optics which offer the possibility of elegant solutions for the active filtering of optical aberrations. After a short description of the aberrated wavefront and its expansion in series of Zernike polynomials, we have presented the general principles of standard AO systems and their mode of operation based on the automatic correction of the perturbed wavefront. Specific notice has been devoted to the description of the Shack Hartmann sensor for the measurement of the Wave Aberration Function and also to the most common kinds of wavefront actuators that are the deformable mirrors at continuous or segmented surface. Our overview of the AO technology has been completed with an accurate examination of the principal operative parameters and the main applications in the fields of astronomy, industry and medicine. From that analysis we have concluded that standard AO techniques, although very advanced for the different applications, are not compliant with the requirements of jitters reduction necessary in interferometric antennas. In fact, we have seen that the Shack Hartmann wavefront sensor, commonly adopted in AO systems, exhibits a residual noise of $10^{-8} \text{ rad}/\sqrt{\text{Hz}}$ which is comparable with the jitters measured in a free laser under quiet laboratory conditions.

The third part of the present Thesis enters the core of our R&D work and presents the design of the AO system that we have developed in order to overcome the serious limitations exhibited by adaptive controls based on the Shack Hartmann sensor. In the system that we propose the wavefront detection is performed by a fast and low noise interferometric technique discovered from the analysis of the perturbed laser beam, in which we have demonstrated that jitters can be alternatively represented in terms of Hermite Gauss modes perturbing the Gaussian fundamental mode or in terms of Zernike polynomials expanding the aberrated wavefront. This correspondence has allowed us to design an AO system where laser fluctuations are interferometrically detected in terms of Hermite Gauss coefficients while wavefront correction is performed through driver commands sent to the deformable mirror in terms of Zernike modes.

We have reported the optical design of the AO system arranged in the configuration of the Michelson interferometer with the piezo mirror put at the end of reference arm and the adaptive mirror put at the end of the second arm

containing the perturbed beam that we need to correct. Using the piezo mirror, the interferometer is locked on the middle fringe working point where the sensitivity is maximum and the output intensity is directly proportional to the small phase variations of the two beams. A 5x5 pixellated photodiode collects the interference fringes at the output of the Michelson and generates 25 photocurrents that we suitably combine to extract 6 signals corresponding to the first and second order Hermite Gauss coefficients of the perturbed beam. These are used as error signals and converted into Zernike commands when we close the adaptive control and perform the simultaneous correction of the 6 aberration modes. We have also presented the design of the closed loop automatic controls used for the lock in and the adaptive correction. In both the block diagrams that represent the control schemes we assume the interferometer as controlled system disturbed by the aberrations while the piezo mirror and the deformable mirror are respectively the regulators for the lock in and the adaptive correction. The matrix formalism has been adopted to represent the transfer functions of the six modes that are simultaneously controlled. They are treated like six independent degrees of freedom thanks to the procedure of matrix diagonalization that is widely discussed.

In order to validate the design of our AO system we have implemented the Prototype on the seismically isolated bench of the Laboratory of Applied Physics led by Professor Fabrizio Barone at the University of Salerno. The experimental apparatus is described in the forth part of our Thesis where we have detailed the geometry of the Michelson configuration and the characteristics of the main components that have been supplied by specific manufacturers that are leader of the market, such as Melles Griot for the He Ne laser, OKO Technologies for the Deformable Mirror and Hamamatsu for the 5x5 pixellated photodiode. We have also described the block diagram of operators that perform the processing unit and that we have implemented using the Labview Virtual Instrument programmed on a standard PC. Finally, we have shown the mode matching arranged for the positioning of the beam waist on the surface of the adaptive mirror and of the photodiodes array.

The last part of this work contains the measures and the results that we have achieved from the test of the Prototype. We have presented three sets of measurements that give the complete characterization of the Prototype and demonstrate its effectiveness in the suppression of laser beam jitters in air in compliance with the Virgo requirements. We have first reported the Bode diagrams of the frequency response functions measured on each of the six automatic controls implemented for the adaptive correction of the laser beam. The diagrams measured at open loop have demonstrated robustness and stability of the controls in the band of interest. In fact the open loop gain at

low frequency is over 60 *dB* and decreases to unity at about 200 *Hz* with slope of -20 *dB/decade*. The cut off frequency is set at 0.1 *Hz* using a low pass filter as correcting network for the stability. On the contrary, the Bode diagrams of the frequency response functions measured at closed loop show the typical behaviour of a second order system with resonance frequency at 450 *Hz* and cut off at about 500 *Hz*. This is the limit to the band of the control and is set by the deformable mirror as actually manufactured by OKO. The second group of measurements that we have reported concern the direct test that we have performed on the Prototype in order to check its capability of reducing the laser jitters. In fact, we have put the system into operation and measured the error signals that indicate the perturbation of the beam. The curves of the aberration coefficients represented in the time domain and in the Fourier domain clearly show that the residual noise measured when the adaptive control loop is closed is strongly suppressed in comparison with the free noise detected when the loop is open. In particular the spectral analysis has allowed to check that reduction of more than 60 *dB* is reached below 1 *Hz* and of 20 *dB* for frequencies up to 100 *Hz*. This means that our AO system fulfils the strict requirements for the laser beam jitters reduction in the Virgo antenna. We have ended the experimental work with a third group of measurements for the quality control of the laser after the adaptive correction. To do that, we have defined a numerical parameter derived from the χ^2 test and have used it as indicator for the quality of the beam. In fact, using the optical theory of interference applied to our Michelson geometry, we have demonstrated that this indicator is equal to 100% if the laser beam under test is perfectly Gaussian and tends to 0% if it is very perturbed with respect to the reference beam. The measures show that when the control loop is open the quality indicator of the free laser is 84% while if adaptive correction is switched on then the same indicator raises to 96%. This is a clear evidence of the improved optical quality of the laser beam performed by the AO system. The results achieved in our Doctoral work allow to say that the AO system we have designed and implemented can be considered a good solution for the reduction of the laser beam jitters in air and therefore can be seriously proposed for application to Virgo upgrade and to Advanced Virgo.

Bibliography

- [1] Ray D’Inverno, *Introducing Einstein’s Relativity*, Clarendon Press, Oxford
- [2] S. Weinberg, *Gravitation and cosmology: principles and applications of the general theory of Relativity*, John Wiley-Sons, New York (1972).
- [3] C.W. Misner, K.S. Thorne, J. Wheeler, *Gravitation*, W. H. Freeman, San Francisco (1973).
- [4] C. Moller, *The theory of relativity*, Oxford University Press, New Delhi (1972).
- [5] R.M. Wald, *General relativity*, The University of Chicago Press, Chicago, (1984).
- [6] S. Bonazzola, J.A. Marck, *Astrophysical sources of gravitational radiation*, Annu. Rev. Nucl. Part. Sci., 45, 655-717 (1994).
- [7] K.S. Thorne, *Probing black holes and relativistic stars with gravitational waves*, grqc/9706079 (1997).
- [8] K.S. Thorne, *Gravitational waves from compact bodies*, in Proc. of IAU Symposium 165, Compact stars in binaries, also gr-qc/9506084 (1995).
- [9] E.E. Flanagan, *Astrophysical sources of gravitational radiation and prospects for their detection*, gr-qc/9804024 (1998).
- [10] R.H. Dicke, *The theoretical significance of experimental relativity*. Gordon and Breach, (1968)
- [11] D.G. Blair, *The detection of gravitational waves*, Cambridge U. Press, Cambridge (1991).
- [12] M. Maggiore, *High-energy physics with gravitational wave experiments*, e-Print Archive: gr-qc/9803028, (1998).

- [13] P.R. Saulson, *Fundamentals of Interferometric Gravitational Wave Detectors*, World Scientific (1994)
- [14] A. Brillet, A. Giazotto et al., *The VIRGO Project, Final Conceptual Design of the French-Italian Interferometric Antenna for Gravitational Wave Detection*, unpublished (1992).
- [15] S. Braccini for the VIRGO Collaboration, *The status of VIRGO*, Proceedings of the 6th Amaldi conference, Class. Quantum Grav. 23 No 8 (2006) S63-S69.
- [16] A. Abramovic et al., *LIGO: The Laser Interferometer Gravitational-Wave Observatory* Science 256, 325 (1992).
- [17] D. Sigg (for the LIGO Science Collaboration), *Status of the LIGO detectors*, Proceedings of the 6th Amaldi conference, Class. Quantum Grav. 23 No 8 (21 April 2006) S51-S56
- [18] For a Review: LIGO Scientific Collaboration, *Recent results on the search for continuous sources with LIGO and GEO*, Proc of TAUP - Zaragoza (2005).
- [19] TAMA Collaboration, *Upper limits from the LIGO and TAMA detectors on the rate of gravitational-wave bursts*, Phys.Rev. D 72: 122004, (2005).
- [20] G. Ballardin et al., *Measurement of the transfer function of the steering filter of the VIRGO super attenuator suspension*, Rev. Sci. Instrum., 72, 3635 (2001).
- [21] M. Bernardini et al., *Suspension last stage for the mirrors of the VIRGO interferometric gravitational wave antenna*, Rev. Sci. Instrum., 70, 3463 (1999).

- [22] G. Losurdo et al., *Inertial control of the mirror suspensions of the VIRGO interferometer for gravitational wave detection*, Rev. Sci. Instrum., 72, 3654-3661 (2001).
- [23] L. Barsotti for the VIRGO Collaboration, *The variable finesse locking technique*, Proceedings of the 6th Amaldi conference, Class. Quantum Grav. 23 No 8 (2006) S85-S89.
- [24] F. Cavalier, *Le controle global de Virgo*, These d'Habilitation a diriger des Recherches, Université de Paris Sud, LAL 01-69 (2001).
- [25] D.Z. Anderson, *Alignment of resonant optical cavities*, Appl. Opt., 23, 2944-2949 (1984).
- [26] M. Mantovani for the VIRGO Collaboration, *The VIRGO automatic alignment system*, Proceedings of the 6th Amaldi conference, Class. Quantum Grav. 23 No 8 (2006) S91-S101.
- [27] F. Acernese, et al., *First locking of the Virgo central area interferometer with suspension hierarchical control*, Astrop. Phys., 20 (6), 629-640 (2004).
- [28] A. Vicere for the VIRGO Collaboration, *The status of coalescing binaries search code in Virgo, and the analysis of C5 data*, Proceedings of the 6th Amaldi conference, Class. Quantum Grav. 23 No 8 (2006) S187-S196.
- [29] A.C. Clapson for the VIRGO Collaboration, *Testing Virgo burst detection tools on commissioning run data*, Proceedings of the 6th Amaldi conference, Class. Quantum Grav. 23 No 8 (2006) S197-S205
- [30] G. Ballardini et al., *Measurement of the VIRGO superattenuator performance for seismic noise suppression*, Rev. Sci. Instrum. 72 3643-3652 (2001).

- [31] R. Loudon, *The Quantum Theory of Light*, 2nd Edition, Clarendon Press, Oxford, 1983
- [32] F. Bondu, J.Y. Vinet, *Mirror thermal noise in interferometric gravitational-wave detectors*, Phys. Lett. A 198: 74-78, (1995).
- [33] F. Bondu, P. Hello, J.Y. Vinet, *Thermal noise in mirrors of interferometric gravitational wave antennas*, Phys. Lett. A 246: 227-236, (1998).
- [34] V.B. Braginsky, M.L. Gorodetsky, *Thermodynamical fluctuations and photo-thermal shot noise in gravitational wave antennae*, S.P. Vyatchanin, Phys. Lett. A 264: 1-10, 1999.
- [35] W. Winkler, K. Danzmann, A. Rudiger, R. Schilling, *Heating by optical absorption and the performance of interferometric gravitational-wave detectors*, Phys. Rev. A 44:7022-7036,(1991).
- [36] P. Hello, *Compensation for thermal effects in mirrors of gravitational wave interferometers*, Eur. Phys. J. D 15:373-383, (2001).
- [37] E. D'Ambrosio, R. O'Shaughnessy, S. String, K.S. Thorne, S. Vyatchanin, *Reducing thermoelastic noise in gravitational-wave interferometers by flattening the light beams*, e-Print Archive: gr-qc/0409075 (Submitted to Phys.Rev. D)
- [38] Y.T. Liu, K.S. Thorne, *Thermoelastic noise and homogeneous thermal noise in finite sized gravitational-wave test masses*, Phys. Rev. D 62: 122002, (2000).
- [39] J.Y. Vinet, *Mirror thermal noise in flat-beam cavities for advanced gravitational wave interferometers*, Class. Quant. Grav. 22: 1395-1404, (2005).

- [40] E. D'Ambrosio, *Nonspherical mirrors to reduce thermoelastic noise in advanced gravitational wave interferometers*, Phys. Rev. D 67: 102004, (2003).
- [41] R.C. Lawrence, *Active wavefront correction in laser interferometric gravitational wave detectors*, PhD thesis (2003).
- [42] E. Calloni, A. Brillet, C.N. Man, F. Barone, F. Fusco, R. De Rosa, L. Di Fiore, A. Grado, L. Milano, G. Russo, *Digital Alignment System for a Laser Beam*, Phys. Lett. A 193, 15-20 (1994).
- [43] S. Grasso, *Rumore ambientale e controlli elettrostatici delle ottiche nell'antenna Virgo*, Tesi di Laurea, biblioteca del Dipartimento di Fisica dell'Università "Federico II" di Napoli
- [44] S. Grasso, C. Altucci, F. Barone, V. Ragozzino, S. Solimeno, Pham-Tu, J.-Y. Vinet, R. Abbate. *Electrostatic systems for fine control of mirror orientation in interferometric GW antennas*, Physics Letters A, 244 (1998), pp. 360-370.
- [45] E. Calloni, F. Barone, L. Di Fiore, A. Grado, P. La Penna, L. Milano, *Effects of misalignment and beam jitter in Fabry-Perot laser stabilization*, Opt. Comm. 142, 50-54, (1997)
- [46] F. Barone, E. Calloni, L. Di Fiore, A. Grado, P. Hello, L. Milano, G. Russo, *Effects of Misalignments and Beam Jitters in Interferometric Gravitational Wave Detectors*, Phys. Lett. A 217, 90-96, (1996).
- [47] R.W.P. Drever et al., *Laser phase and frequency stabilization using an optical resonator*, Appl. Phys. B: Photophys. Laser Chem. 31 (1983) 97-105
- [48] A. Rüdiger, R. Schilling, L. Schnupp, W. Winkler, H. Billing and K. Maischberger, *A mode selector to suppress fluctuations in laser beam geometry*, Opt. Acta 28, 641, (1981).

- [49] Y. Hefetz, M. Mavalvala, D. Sigg, *Principles of calculating alignment signals in complex optical interferometers*, J. Opt. Am. B, 14, 1597-1605, (1997).
- [50] E. Morrison, B. J. Meers, D. I. Robertson, H. Ward, *Automatic alignment of optical interferometers*, Appl. Opt. 33, 5037 (1994).
- [51] J.D. Mansell, J. Hennawi, E.K. Gustafson, M.M. Fejer, R.L. Byer, D. Clubey, S. Yoshida, D.H. Reitze, *Evaluating the Effect of Transmissive Optic Thermal Lensing on Laser Beam Quality With a Shack - Hartmann Wave-Front Sensor*, Appl. Opt. 40, 366-374, (2001).
- [52] G Mueller, R.S. Amin, D. Guagliardo, D. McFeron, R. Lundock, D.H. Reitze and T.B. Tanner, *Method for compensation of thermally induced modal distortions in the input optical components of gravitational wave interferometers*, Class. Quant. Grav. 19, 1793-1801, (2002).
- [53] F. Bondu, *Study of thermal noise and frequency stabilization of the laser of interferometric detector of Virgo gravitational waves*, (Orsay, LAL), Jan 1996. 180pp, Ph.D. Thesis.
- [54] H. Luck, K.O. Muller, P. Aufmuth, K. Danzmann, *Correction of wavefront distortions by means of thermally adaptive optics*, Opt. Comm. 175, 275-287, (2000).
- [55] J.T. Baker, F. Barone, E. Calloni, R. De Rosa, L. Di Fiore, A. Eleuteri, L. Milano, S. Restaino, K. Quipiani, *An adaptive optics approach to the reduction of misalignments and beam jitters in gravitational wave interferometers*, Class. Quantum Grav. 19, 1813-1818, (2002).
- [56] B. Rossi, *Ottica*, Masson, 1991
- [57] A. E. Conrady, *Applied Optics and Optical Design*, Dover Publications, N.Y., 1929
- [58] R. Bruzzese, *Ottica, Laser e Applicazioni*, Ed. Liguori, Napoli, 1994

- [59] M. Born and E. Wolf, *Principles of Optics*, 7th (expanded) Ed., Cambridge University Press, 1999
- [60] R. E. Fischer, *Optical System Design*, McGraw Hill, N.Y., 2000
- [61] Max, CE, Bauman B, and Chanan G., *Zernike polynomials and their relation to Seidel polynomials*, Lecture for The Center for Adaptive Optics Lecture, University of California at Santa Cruz, April 18,2002
- [62] W. Brouwer, *Matrix Methods in Optical Instrument Design*, Benjamin, N.Y., 1964
- [63] Zemax, *Optical Design Program – User’s Guide*, Zemax Development Corporation, 2006
- [64] R.K.Tyson, B.W.Frazier, *Field Guide to Adaptive Optics*, SPIE Field Guides, Volume FG03, J.E.Greivenkamp, Series Editor
- [65] A. Tokovinin, *Tutorial on adaptive optics at CTIO*, <http://www.ctio.noao.edu/>
- [66] Tyson, K. Robert, *Introduction to adaptive optics*, Bellingham, WA: SPIE, The International Society for Optical Engineering (2000).
- [67] Tyson, K. Robert, *Principles of adaptive optics*, Boston, MA: Academic Press (1998).
- [68] Daniel R. Neal *Shack-Hartmann sensor engineered for commercial measurement applications*, WaveFront Sciences, Inc., 14810 Central S.E., Albuquerque, NM 87123, SPIE 5162-19
- [69] E. Dalimier, C. Dainty, *Comparative analysis of deformable mirrors for ocular adaptive optics*, Optics Express 13, 4275-4285 (2005).
- [70] Bifano, T. G., Perreault, J., Mali, R. K., and Horenstein, M. N., *Microelectromechanical Deformable Mirrors*, *Journal of Selected Topics in Quantum Electronics*, [5], pp. 83-90, 1999

- [71] Perreault, J. A., Bifano, T. G., Levine, B.M., and Horentein, M. N., *Adaptive optic correction using microelectromechanical deformable mirrors*, Optical Eng'g [41] 5, pp. 561-566, 2002
- [72] H. Babcock, *The possibility of compensating astronomical seeing*, Publ. Astron. Soc. Pac. 65,229-236,(1953)
- [73] *Adaptive Optics in Astronomy*, edited by F. Roddier (Cambridge University Press, Cambridge, UK), (1999).
- [74] J.W. Hardy, *Adaptive optics for astronomical telescopes*, New York, NY: Oxford University Press (1998).
- [75] Gardner, C.S., B.M. Welsh, and L.A. Thompson, *Design and performance analysis of adaptive optical telescopes using laser guide stars*, Proc. IEEE 78, 1721-1743 (1990).
- [76] *Adaptive Optics for Industry and Medicine*, edited by S. R. Restaino and S. W. Teare, Albuquerque, (2002).
- [77] *Adaptive Optics for Vision Science*, Edited by J. Porter, H. Queener, J. Lin, K. Thorn and A. Awwal, J. Wiley & Sons
- [78] Doble, Williams, (Center for Visual Science, Univ. Of Rochester, NY, USA.), *The application of MEMS technology for adaptive optics in vision science*, Selected Topics in Quantum Electronics, IEEE Journal of, May-June 2004 Volume 10 Issue 3, Pages 629-635)
- [79] A. Roorda and D. R. Williams, *The arrangement of the three cone classes in the living human eye*, Nature, vol. 397, pp. 520–522, 1999.
- [80] J. Liang, D. R. Williams, and D. T. Miller, *Supernormal vision and high-resolution retinal imaging through adaptive optics*, J. Opt. Soc. Amer. A, Opt. Image Sci., vol. 14, pp. 2884–2892, 1997.
- [81] H. Hofer, L. Chen, G. Y. Yoon, B. Singer, Y. Yamauchi, and D. R. Williams, *Improvement in retinal image quality with dynamic*

- correction of the eye's aberrations*, Opt. Express, vol. 8, pp. 631–643, 2001.
- [82] A. W. Dreher, J. F. Bille, and R. N. Weinreb, *Active optical depth resolution improvement of the laser tomographic scanner*, Appl. Opt., vol. 28, pp. 804–808, 1989.
- [83] J. Liang, B. Grimm, S. Goelz, and J. F. Bille, *Objective measurement of the wavefront aberration of the human eye with the use of a Hartmann–Shack wavefront sensor*, J. Opt. Soc. Amer. A, Opt. Image Sci., vol. 11, no. 7, pp. 1949–1957, 1994.
- [84] J. Liang and D. R. Williams, *Aberrations and retinal image quality of the normal human eye*, J. Opt. Soc. Amer. A, Opt. Image Sci., vol. 14, pp. 2873–2883, 1997.
- [85] T. Weyrauch, M. A. Vorontsov, J. W. Gowens II, T. G. Bifano, *Fiber coupling with adaptive optics for free-space optical communication*, Free-Space Laser Communication and Laser Imaging, David G. Voelz, Jennifer C. Ricklin, Editors, Proceedings of SPIE Vol. 4489 (2002)
- [86] P. Kurczynski, A. J. Tyson, B. Sadoulet, D. J. Bishop, and D. R. Williams, *Membrane mirrors for vision science adaptive optics*, in Proc. SPIE, vol. 4561, 2001, pp. 147–162.
- [87] E. J. Fernandez and P. Artal, *Membrane deformable mirror for adaptive optics: Performance limits in visual optics*, Opt. Express, vol. 11, pp. 1056–1069, 2003.
- [88] S. Middelhoek, S.A. Audet, *Silicon sensors*, Academic Press, London, 1989
- [89] L.S. Fan, Y.C. Tai and R.S. Muller, *Integrated movable micromechanical structures for sensors and actuators*, IEEE Trans. Electron Devices 35, 724-730, 1998

- [90] L. N. Thibos and A. Bradley, *Use of liquid-crystal adaptive-optics to alter the refractive state of the eye*, Optom. Vis. Sci., vol. 74, no. 7, pp. 581–587, 1997.
- [91] S. Grasso, F. Acernese, R. Romano and F. Barone, *Adaptive optics system prototype for the automatic control of geometrical fluctuations in a laser beam in air*, Proc. SPIE 6747, 67470V (2007), Florence (IT), 17-21 September 2007
- [92] S. Grasso, F. Acernese, R. Romano and F. Barone, *Automatic control of laser beams aberrations in air using an adaptive optics system prototype based on interferometric techniques*, Proc. SPIE 6932, 69323T (2008), S. Diego (California), 9-13 March 2008
- [93] S. Grasso, F. Acernese, R. Romano, F. Barone, *Adaptive Optics System Prototype for the automatic control of geometrical fluctuations in a laser beam in air*, Proc. SPIE 7108, 71080Q (2008), Cardiff (UK), 15-18 September 2008
- [94] O. Svelto, *Principles of lasers*, 3rd Ed., Plenum press, N.Y., (1995)
- [95] H. Kogelnick and T. Li, *Laser beams and resonators*, Appl. Opt., 5, 1550, (1966)
- [96] G. Marro, *Controlli Automatici*, Zanichelli, Bologna, 1992
- [97] *Helium Neon Lasers*, Melles Griot, www.mellesgriot.com
- [98] *Single frequency laser Operating Manual*, Melles Griot Laser Group, Carlsbad, California, USA, (1999)
- [99] G. Vdovin, *39/59 – channel micromachined adaptive mirror: technical data and operating manual*, Flexible Optical & Inventive Data, Delft, The Netherlands, www.okotech.com, (2002)

- [100] G. Gaydadjiev, G. Vdovin, *24-ch 8 bit PCI DAC card – Installation and Programmers Guide*, Flexible Optical & Inventive Data, Delft, The Netherlands, www.okotech.com, (2002)
- [101] 5x5 element Si PIN photodiode array S7585, Hamamatsu Photonics K.K., Solid State Division, Hamamatsu City, Japan, www.hamamatsu.com
- [102] J. Millmann, *Circuiti e sistemi microelettronici*, Bollati Boringhieri (1990)
- [103] J. Millmann and C.C. Halkias, *Integrated Electronics: Analog and Digital Circuits and Systems*, Mc Graw Hill, N.Y. (1972)
- [104] *Low noise, Precision Operational Amplifier OP27*, Technical Paper, Analog Devices, Norwood U.S.A., www.analog.com, (2006)
- [105] E. Burattini, C. Sciacca, *Misure elettriche e fondamenti di elettronica*, Ed. Liguori, Napoli (1980)
- [106] S. Fenney, *The Labview Programming Environment and Basic Operations*, Arizona State University
- [107] *Labview User's Manual, Part Number 320999D-01*, National Instruments, www.ni.com, (2001)
- [108] A. Papoulis, *Probabilità, variabili aleatorie e processi stocastici*, Boringhieri, Torino, 1981
- [109] P. R. Oliva e F. Terrasi, *Elaborazione statistica dei risultati sperimentali*, Ed. Liguori, Napoli, 9th Edition (1988)
- [110] *Matlab User Guides*, The MathWorks, Inc., www.mathworks.com, (2005)
- [111] A. Oppenheim, R. Schafer, *Elaborazione Numerica dei Segnali*, F. Angeli Editore

- [112] M. Severi, *Introduzione alla sperimentazione fisica*, Zanichelli, Bologna, 1985
- [113] J. R. Taylor, *Introduzione all'analisi degli errori*, Zanichelli, Bologna, 1986

Acknowledgments

The realization of this PhD work has been possible thanks to the contribution of many people who have given me not only scientific suggests but also the human support which I consider even more important.

First of all, my gratitude to Professor Fabrizio Barone who has always believed in me and given the chance to join his group of research at the University of Salerno.

I am also very grateful to Professor Giuseppe Schirripa and to Professor Gennaro Conte for allowing me to enter the XXI Doctoral Course at the University of Roma Tre and for the supervision of my PhD work.

Many thanks to Dr. Fausto Acernese and to Dr. Gerardo Giordano for the essential help and collaboration in laboratory and for the friendship we have formed and that I hope will last in the future.

Finally, I want to remember all the people of my private life who have sustained me in several moments of difficulty that I have faced in this last three years.